Resolving the Structure, Morphology, and Trace Metal Association of Nanominerals: The Case for Schwertmannite

Rebecca A. French

Dissertation submitted to the faculty of the Virginia Polytechnic Institute and State University in partial fulfillment of the requirements for the degree of

Doctor of Philosophy
In
Geosciences

Michael F. Hochella Jr., Chair
Mitsuhiro Murayama
J. Donald Rimstidt
Matthew J. Eick

August 12th, 2011
Blacksburg, VA

Keywords: schwertmannite, iron oxide, transmission electron microscopy, nanomineral, acid mine drainage

Resolving the Structure, Morphology, and Trace Metal Association of Nanominerals: The Case for Schwertmannite

Rebecca A. French

ABSTRACT

Schwertmannite, a ferric oxyhydroxysulfate mineral typically found under acidic, high sulfate and iron aqueous conditions, such as acid mine drainage environments, was studied using analytical high resolution transmission electron microscopy (HRTEM). HRTEM offers advantages over bulk techniques such as powder x-ray diffraction and pair distribution function (PDF) analysis of synchrotron data, in its ability to discern multiple phases within poorly crystalline nanominerals. Based on extensive HRTEM observations of both natural and synthetic schwertmannite samples, the authors suggest that schwertmannite should not be described as a single phase mineral with a repeating unit cell, but as a polyphasic nanomineral with crystalline areas spanning less than a few nanometers within an amorphous matrix. The few visible lattice fringes observable in both natural and synthetic schwertmannite agree well with d-spacings of goethite (and jarosite in natural samples) implying that the transformation from schwertmannite to these phases occurs as a gradual structural reordering at the nanoscale. In the synthetic study, the complete transformation from schwertmannite to goethite nanorods and nanoparticles within 24 hours at 75°C was observed, indicating a low energetic barrier to schwertmannite's phase transformation. We also found that amorphous silica can be intimately entrained within natural schwertmannite, and that high concentrations of arsenic can be held in close association of nanocrystalline regions of the mineral.

Acknowledgments

I would like to thank my advisor Mike for all of his support throughout my Ph.D. He is an exceptional advisor in his open mind towards what graduate education can be and what a student may do with it for a career. He encouraged me to apply for the position of Graduate Student Representative to the BOV, knowing that it would take a significant time commitment that few other advisors would approve of for a Ph.D. student, but it paid off. Thanks Mike. I would like to thank my committee members for their many cumulative hours of classes, discussions, and writing contributions to the manuscripts in this dissertation. I would particularly like to thank Mitsu and Niven for helping me navigate the field of TEM. Thank you to Manuel and his family for showing me the 'field' for the first time and giving me a Spanish family. I would like to thank the members of my VT family: the Hochella group, for many good times and advice; the ENT Lab for their friendship and teamwork in building a successful interdisciplinary and multi-department lab at VT; and finally the Department of Geosciences. Its students, faculty, and staff have been a great pleasure to work with for the past four years and they made this academic journey a smooth ride. I would like to thank my colleagues in student government at VT who taught me more than can ever be observed under a microscope. I would like to thank Beth and Carol, for being my most steadfast friends while at VT and Mark, who has held my hand throughout the last few months of my Ph.D. with unwavering kindness and understanding. Finally, I would like to thank my family for their love and support. It was my family's strong belief in the value of education that made me believe that I could go all the way. I look forward to becoming the second Dr. French in my family with many more to follow.

Attributions

Several colleagues and coworkers aided in the writing and research for many sections of this dissertation. A brief description of their background and contributions are below.

Professor Michael F. Hochella Jr. (Department of Geosciences, Virginia Tech) is the primary research advisor and Committee Chair. He provided general scientific guidance and support with writing all of the Chapters. He has also provided the majority of financial support for this research.

Professor Mitsuhiro Murayama (Department of Materials Science and Engineering, Virginia Tech) is a committee member and provided general scientific guidance and assisted in the collection of all images from the FEI Titan transmission electron microscopes which were used for Chapters 2 and 3. He helped with experimental design on these microscopes, assisted with the interpretation of results, and contributed to the writing of Chapters 2 and 3.

Professor Emeritus J. Donald Rimstidt (Department of Geosciences, Virginia Tech) is a committee member and provided general scientific guidance, especially on understanding the geochemistry of acid mine drainage systems and crystal growth mechanisms. He assisted in the interpretation of results and writing in Chapter 3.

Dr. Manuel A. Caraballo (Geology Department, University of Huelva, Spain) obtained the natural schwertmannite samples, collected field measurements, and calculated the saturation indices for Chapter 3 and helped with the interpretation of results and environmental context for the field site in the Iberian Pyrite Belt of Spain. He also aided in the writing of Chapter 3.

Dr. Niven Monsegue (Department of Materials Science and Engineering, Virginia Tech) assisted with the collection of images and selected area electron diffraction patterns on the Philips EM 420 transmission electron microscope and the interpretation of results from those images for Chapter 2.

Dr. Bojeong Kim (Department of Geosciences, Virginia Tech) prepared ultramicrotomed samples of natural schwertmannite, aided in the experimental design for the environmental scanning electron microscope/energy dispersive spectroscopy pre-scan analysis for arsenic, and in the writing for Chapter 3.

Table of contents

List of Figures

Chapter 2

Chapter 3

Appendix A

List of Tables

Chapter 3

1) Introduction

"Always formed as sub-micron crystallites, [schwertmannite] is an important agent for sorption of metal contaminants, as well as a carrier of significant sulfate, in acid mine drainage situations" (Waychunas et al., 2005).

This was my introduction to schwertmannite. I had read the review article entitled, *Nanoparticulate iron oxide minerals in soils and sediments: unique properties and contaminant scavenging mechanisms*, from which this quote was taken, while pursuing my M.S. degree at Cornell University. At that time I was studying the aggregation behavior of titanium dioxide nanoparticles in water (French et al., 2009) and was not concerned with iron oxides in particular, but upon embarking on my Ph.D. at Virginia Tech I revisited this paper hoping for inspiration. I found it in schwertmannite. What caught my attention was that in that one sentence were the key ingredients for an exciting story in nanogeoscience.

First, schwertmannite is a major mineral in acid mine drainage environments. In a 1989 study it was estimated that 9,300 km of streams and rivers, and ca. 72,000 ha of lakes and reservoirs worldwide have been significantly harmed by mine effluents (Johnson and Hallberg, 2005). Acid mine drainage is the major cause of this damage because many valuable metals occur as sulfide ores (e.g. CuS, ZnS, etc.) and these ores are often found with pyrite (FeS_2). Acid mine drainage results from the oxidation of pyrite; a process which releases protons generating acidity and the release of toxic levels of trace metals. Second of all, schwertmannite sorbs metals, particularly arsenic under low pH conditions (Acero et al., 2006; Asta et al., 2010). Arsenic is a highly regulated metal with a World Health Organization drinking water standard of 10 ppb and may

cause skin, lung, bladder, and kidney cancer with long-term low level exposure (Mohan and Pittman, 2007). Finally, schwertmannite "always forms as sub-micron crystallites" making schwertmannite a nanomineral.

Hochella et al. (2008) defined nanominerals as minerals that in at least one of their dimensions measure 1 nm to 100 nm. Nanominerals, unlike mineral nanoparticles that have a bulk counterpart, will only ever be found in this size range. There are few known minerals that fall into this category –ferrihydrite being the most famous example– due to the difficulty of characterizing minerals at the nanoscale. As a result of their small size nanominerals may exhibit surface structural disorder and in the case of minerals that are only a few nanometers in diameter, the disorder of the surface may affect the entire atomic structure of the mineral. This disorder found in nanominerals presents challenges for defining unique atomic structures for these minerals. For example, pair distribution function (PDF) analysis of high-energy x-ray total scattering experiments performed on a synchrotron allowed researchers to significantly refine the structure of the nanomineral ferrihydrite (Michel et al., 2007; Michel et al., 2010). But since this structure was published researchers have called into question the ability of PDF analysis to provide sufficient information to determine the structure of ferrihydrite and generally the ability of PDF analysis to provide sufficient information to determine unique crystallographic structures for nanominerals (Manceau, 2009, 2010, 2011). Schwertmannite may suffer the same problems as ferrihydrite and in fact researchers that used PDF analysis to refine the structure for schwertmannite acknowledge that their proposed structure is "highly defective" (Fernandez-Martinez et al., 2010).

With this in mind, I set out to better understand the structure and morphology of schwertmannite using high resolution transmission electron microscopy (HRTEM). Unlike bulk analyses such as powder x-ray diffraction and synchrotron PDF analysis, HRTEM may identify differences in phase and crystallinity at the nano- and atomic scale within a single mineral. Using this technique, researchers have discovered non-classical crystal growth mechanisms such as oriented attachment of nanoparticles (Banfield et al., 2000), directly observed surface structural disorder resulting from changes in nanoparticle size (Chernyshova et al., 2007), and recognized crystal face dependent dissolution (Liu et al., 2008).

In the first manuscript in Chapter 2 of the dissertation entitled, *Temperature controlled crystal growth of the Fe(III)-oxyhydroxysulfate nanomineral schwertmannite and subsequent transformation to goethite nanorods*, I investigate schwertmannite produced in the laboratory. Although geochemists are ultimately concerned with real world problems, they often use synthetic minerals for controlled laboratory experiments as it may be difficult to obtain pure mineral samples from the field. But researchers hope to mimic field conditions as closely as possible and therefore require synthetic samples that have equivalent structure and properties to their field counterparts. In the case of nanominerals, where the atomic structure may be poorly understood, differences in synthetic conditions could produce synthetic schwertmannite with variable composition and structure and/or synthetic samples that do not accurately reflect field samples. As the majority of studies on schwertmannite rely on powder XRD as a fingerprint for schwertmannite, I was concerned that there could be differences between synthetic and

natural samples that would not be exposed through XRD. It also follows that findings from these studies may or may not be relevant to field conditions.

In the second manuscript in Chapter 3 of the dissertation entitled, *Identifying the polyphasic structure, morphology, and arsenic association of the metastable ferric oxyhydroxysulfate nanomineral schwertmannite using analytical high resolution transmission electron microscopy,* I investigate natural schwertmannite collected from two abandoned mine sites in the Iberian Pyrite Belt (IPB) of southwest Spain. The IPB is a world class site to study schwertmannite as it is the largest known pyrite deposit in the world and has been mined for thousands of years leaving extensive pollution (Sarmiento et al., 2009). A survey of the IPB determined that schwertmannite is the "most important mineral phase, both in controlling the Fe solubility at pH 2-4, and as a sorbent of the trace elements (As, Cu, Zn)" (Espana et al., 2005). Chapter 3 shows the first HRTEM images of natural schwertmannite at a resolution where we can determine differences in structure and morphology across the two field sites. The results show that schwertmannite should not be defined as a classical mineral with a repeating unit cell, but as a polyphasic mineral with crystalline areas spanning less than a few nanometers within an amorphous matrix. The natural samples also contain between ~2000 ppm and ~5000 ppm arsenic. Using energy dispersive x-ray spectroscopy (EDX) we show the distribution of arsenic across individual schwertmannite needles with nanoscale resolution and the resulting implications for arsenic's fate and transport in the IPB.

Although the review by Waychunas et al. (2005) noted some of the important features of schwertmannite, it did not discuss how this mineral is formed and transformed. Using HRTEM the studies in Chapter 2 and 3 reveal that schwertmannite

does not exhibit features characteristic of the classical crystal growth mechanism of ion by ion attachment to a crystal face, but rather forms via non-classical mechanisms such as aggregation of nanoparticles or nanoclusters and/or attachment of ions and/or oligomers to an amorphous phase, which then crystallizes with aging. Previous studies showed that further aging of schwertmannite produces goethite and jarosite. The studies in this dissertation reveal how and under what conditions that aging occurs.

Through working on synthetic and natural schwertmannite and on a lab and field scale this dissertation addresses questions across those areas and draws links between them. Under those conditions the work in this dissertation required a multi- and interdisciplinary approach to science and therefore addresses problems in the established disciplines of materials science, environmental engineering, geochemistry, mineralogy, and soil science as well as emerging fields that work across those disciplinary boundaries such as nanogeoscience and biomineralization. Furthermore, in order to combine those fields, this dissertation required collaboration across multiple departments, subdisciplines, and continents. In this way not only does this dissertation reflect the challenge of investigating a nanomineral using HRTEM, but the challenge of approaching a scientific problem that has no clear disciplinary home. I hope that it will serve as an example of how one may take on such a challenge.

References

Acero, P., Ayora, C., Torrento, C., and Nieto, J.M. (2006) The behavior of trace elements during schwertmannite precipitation and subsequent transformation into goethite and jarosite. Geochimica Et Cosmochimica Acta, 70(16), 4130-4139.

Asta, M.P., Ayora, C., Roman-Ross, G., Cama, J., Acero, P., Gault, A.G., Charnock, J.M., and Bardelli, F. (2010) Natural attenuation of arsenic in the Tinto Santa Rosa acid stream (Iberian Pyritic Belt, SW Spain): The role of iron precipitates. Chemical Geology, 271(1-2), 1-12.

Banfield, J.F., Welch, S.A., Zhang, H.Z., Ebert, T.T., and Penn, R.L. (2000) Aggregation-based crystal growth and microstructure development in natural iron oxyhydroxide biomineralization products. Science, 289(5480), 751-754.

Chernyshova, I.V., Hochella, M.F., and Madden, A.S. (2007) Size-dependent structural transformations of hematite nanoparticles. 1. Phase transition. Physical Chemistry Chemical Physics, 9(14), 1736-1750.

Espana, J.S., Pamo, E.L., Santofimia, E., Aduvire, O., Reyes, J., and Barettino, D. (2005) Acid mine drainage in the Iberian Pyrite Belt (Odiel river watershed, Huelva, SW Spain): Geochemistry, mineralogy and environmental implications. Applied Geochemistry, 20(7), 1320-1356.

Fernandez-Martinez, A., Timon, V., Roman-Ross, G., Cuello, G.J., Daniels, J.E., and Ayora, C. (2010) The structure of schwertmannite, a nanocrystalline iron oxyhydroxysulfate. American Mineralogist, 95, 1312-1322.

French, R.A., Jacobson, A.R., Kim, B., Isley, S.L., Penn, R.L., and Baveye, P.C. (2009) Influence of Ionic Strength, pH, and Cation Valence on Aggregation Kinetics of Titanium Dioxide Nanoparticles. Environmental Science & Technology, 43(5), 1354-1359.

Hochella, M.F., Lower, S.K., Maurice, P.A., Penn, R.L., Sahai, N., Sparks, D.L., and Twining, B.S. (2008) Nanominerals, mineral nanoparticles, and Earth systems. Science, 319(5870), 1631-1635.

Johnson, D.B., and Hallberg, K.B. (2005) Acid mine drainage remediation options: a review. Science of the Total Environment, 338(1-2), 3-14.

Liu, J., Aruguete, D.A., Jinschek, J.R., Rimstidt, J.D., and Hochella, M.F. (2008) The non-oxidative dissolution of galena nanocrystals: Insights into mineral dissolution rates as a function of grain size, shape, and aggregation state. Geochimica Et Cosmochimica Acta, 72(24), 5984-5996.

Manceau, A. (2009) Evaluation of the structural model for ferrihydrite derived from real-space modelling of high-energy X-ray diffraction data. Clay Minerals, 44(1), 19-34.

Manceau, A. (2010) PDF analysis of ferrihydrite and the violation of Pauling's Principia. Clay Minerals, 45(2), 225-228.

Manceau, A. (2011) Critical evaluation of the revised akdalaite model for ferrihydrite. American Mineralogist, 96(4), 521-533.

Michel, F.M., Ehm, L., Antao, S.M., Lee, P.L., Chupas, P.J., Liu, G., Strongin, D.R., Schoonen, M.A.A., Phillips, B.L., and Parise, J.B. (2007) The structure of ferrihydrite, a nanocrystalline material. Science, 316(5832), 1726-1729.

Michel, F.M., Barron, V., Torrent, J., Morales, M.P., Serna, C.J., Boily, J.F., Liu, Q.S., Ambrosini, A., Cismasu, A.C., and Brown, G.E. (2010) Ordered ferrimagnetic form of ferrihydrite reveals links among structure, composition, and magnetism. Proceedings of the National Academy of Sciences of the United States of America, 107(7), 2787-2792.

Mohan, D., and Pittman, C.U. (2007) Arsenic removal from water/wastewater using adsorbents - A critical review. Journal of Hazardous Materials, 142(1-2), 1-53.

Sarmiento, A.M., Nieto, J.M., Olias, M., and Canovas, C.R. (2009) Hydrochemical characteristics and seasonal influence on the pollution by acid mine drainage in the Odiel river Basin (SW Spain). Applied Geochemistry, 24(4), 697-714.

Waychunas, G.A., Kim, C.S., and Banfield, J.F. (2005) Nanoparticulate iron oxide minerals in soils and sediments: unique properties and contaminant scavenging mechanisms. Journal of Nanoparticle Research, 7(4-5), 409-433.

2) Temperature controlled crystal growth of the Fe(III)-oxyhydroxysulfate nanomineral schwertmannite and subsequent transformation to goethite nanorods

Rebecca A. French[1,2*], Niven Monsegue[3,4], Mitsuhiro Murayama[3,4], Michael F. Hochella Jr.[1,2]

[1]ICTAS Environmental Nanoscience and Technology Laboratory, Virginia Tech, Blacksburg, VA 24061, U.S.A.
[2]Department of Geosciences, Virginia Tech, Blacksburg, VA 24061, U.S.A.
[3]ICTAS Nanoscale Characterization and Fabrication Laboratory, Virginia Tech, Blacksburg, VA 24061, U.S.A.
[4]Department of Materials Science, Virginia Tech, Blacksburg, VA 24061, U.S.A.
*Corresponding author e-mail address: rafrench@vt.edu

To be submitted to Journal of Crystal Growth

Abstract

The structure and phase transformation of schwertmannite, an iron oxyhydroxide sulfate nanomineral, synthesized at room temperature and at 75°C, was studied using high resolution transmission electron microscopy (HRTEM). HRTEM revealed that schwertmannite produced at both temperatures exhibited the characteristic morphology of electron dense spheres with nanoneedles. These needles were rounded with no clear faceting and had few distinct lattice fringes. The lattice fringes are consistent with the x-ray diffraction pattern for the bulk schwertmannite and also match d-spacings for goethite, indicating a close structural relationship between schwertmannite and goethite. The complete transformation from schwertmannite to goethite nanorods and nanoparticles (2-4 nm in diameter) within 24 hours at 75°C was observed. The results of this study suggest that schwertmannite should not be described as a single phase with a repeating unit cell, but as a polycrystalline material displaying amorphous and poorly ordered areas within needles. The transformation of schwertmannite to goethite at 75°C

supports the model that metastable nano-precursor phases are initially favored over the thermodynamically stable phase in the iron oxide system.

2.1 Introduction

Schwertmannite is an Fe(III)-oxyhydroxysulfate nanomineral with the proposed chemical formula of $Fe_8O_8(OH)_{8-x}(SO_4)_x$ ($1<x<1.75$) (Bigham et al., 1994). Schwertmannite occurs naturally in acid mine drainage systems and acid sulfate soils (Acero et al., 2006; Burton et al., 2007; Espana et al., 2005; Regenspurg et al., 2004). It has also been found in the waste streams for zinc ore (Claassen et al., 2002; Zinck and Dutrizac, 1998) and coal processing (Barham, 1997) and was suggested as a possible candidate for a raw material for the pigment industry (Barham, 1997). We designate schwertmannite as a nanomineral because it only ever grows to between 1 and 100 nm in at least one of its dimensions (Hochella et al., 2008). Its characteristic 'pin-cushion' morphology is electron dense spheres of 200-500 nm in diameter with nanoneedles of 2-4 nm in width and 60-90 nm in length protruding from the surface (Bigham et al., 1994; Bigham and Nordstrom, 2000).

Nanominerals are difficult to characterize due to their small size and resulting variable atomic structure that can result in structural disorder, strain, and reconstructed surfaces (relative to the interior structure) (Hochella et al., 2008). Schwertmannite exhibits this structural disorder in its characteristic broad 8-line x-ray diffraction (XRD) pattern (Bigham et al., 1994). As a result, determining the structure of schwertmannite remains a challenge. Bigham et al. (Bigham et al., 1990) proposed a structure based on akaganéite (β-FeO(OH)) with sulfate occupying the tunnels formed by octahedral iron chains rather than chloride as in akaganéite. Sulfate forms a bidentate complex with the

iron in the tunnels and distorts the structure. More recently a pair distribution function (PDF) analysis of synchrotron powder diffraction data on synthetic schwertmannite (Schwertmann and Cornell, 1991) and natural schwertmannite showed that schwertmannite consists of a "highly defective entangled network" of an iron octahedral frame similar to akaganéite (Fernandez-Martinez et al., 2010). In this proposed structure each unit cell contains two inner-sphere and two outer-sphere sulfate complexes. An electron nanodiffraction study on synthetic schwertmannite did not show evidence for an akaganéite-like structure and found similarities between schwertmannite and 2-line ferrihydrite (Loan et al., 2004). High resolution transmission electron microscopy (HRTEM) provided further insight into the complexity of this same synthetic schwertmannite's structure and morphology showing schwertmannite composed of a ferrihydrite ($Fe_{10}O_{14}(OH)_2$ (Michel et al., 2007)) core with needles grown by oriented attachment of goethite (α-FeOOH) nanocrystals nucleating off of the core (Hockridge et al., 2009). The formation of goethite from oriented attachment of ferrihydrite nanoparticles has been observed under synthetic conditions (Burleson and Penn, 2006; Penn et al., 2006) and in acid mine drainage systems (Banfield et al., 2000).

In natural systems and in waste streams schwertmannite is often found mixed with other iron oxide phases (Espana et al., 2005), making it difficult to obtain pure samples from field sites. Furthermore, iron oxidizing bacteria facilitate the precipitation of schwertmannite at low temperature (Bigham et al., 1996a). The difficulty of synthesizing schwertmannite in a bioreactor and collecting it in the field necessitated the development of abiotic syntheses for schwertmannite. Researchers used temperatures ranging from 60°C to 85°C to drive hydrolysis and precipitate schwertmannite (Loan et al., 2004;

Schwertmann and Cornell, 1991). One synthesis included extraneous salts that required a dialysis step for their removal (Schwertmann and Cornell, 1991). A synthesis used by Regenspurg et al. (Regenspurg et al., 2004) used peroxide as the oxidizing agent to convert ferrous sulfate to schwertmannite at room temperature, avoiding raising the temperature and adding extraneous salts.

Though these syntheses were run at temperatures ranging from 25° to 85°C, few studies have examined the effect of temperature on schwertmannite. Knorr et al. (Knorr and Blodau, 2007) found that at 10°C and 20°C schwertmannite transformed to an x-ray amorphous material with somewhat increased crystallinity and lower sulfate content and that the increase in temperature increased the transformation rate by a factor of 3.8. Conversely, another study showed that at 4°C schwertmannite remained stable for at least 5 years (Jonsson et al., 2005). Most lab studies found that schwertmannite transformed to goethite at room temperature, but the time of transformation varied significantly from 79 days to 543 days (Bigham et al., 1996b; Jonsson and Lovgren, 2006; Knorr and Blodau, 2007; Schwertmann and Carlson, 2005). Field studies also observed that fresh precipitates of schwertmannite are found on top of goethite in deeper sediment, indicating that aging of the schwertmannite precipitates forms goethite (Espana et al., 2005). Hockridge et al. (Hockridge et al., 2009) showed that after 24 hours at 85°C, schwertmannite partially transformed to goethite.

In this study we investigate the effect of varying temperature on the morphology, structure, and transformation of schwertmannite using HRTEM. HRTEM reveals that schwertmannite produced at different temperatures and displaying similar XRD patterns, exhibits different morphology and structure. Furthermore we show, for the first time, that

the needles of schwertmannite may not be well-described as a single crystalline phase, but rather envisioned as a mix of amorphous and crystalline material with short-range order. Finally the complete transformation of schwertmannite to goethite nanocrystals and nanorods at 75°C within 24 hours was observed for the first time.

2.2 Materials and Methods

2.21 Synthesis

The room temperature synthesis was based on a method in Regenspurg et al. (Regenspurg et al., 2004). Five grams of $FeSO_4$ was dissolved in 500 mL of water (NANOpure®, <18 MΩ-cm, <1 ppb TOC) and placed in a 1000 mL round-bottom flask with stirring. The reaction clock started when 2.5 mL of 30% hydrogen peroxide (H_2O_2) was added to the solution. One synthesis was run at room temperature for 24 hours. The second synthesis was run at 75 ± 2°C for 24 hours using a heating mantle and thermocouple (Barnant Co. Temperature Controller) to maintain the temperature over the course of the experiment. In the experiment run at 75°C, the hydrogen peroxide was added after the $FeSO_4$ solution had reached 75°C.

2.22 Characterization

We collected precipitate from the reaction flask for the X-ray diffraction (XRD) analysis of the 75°C synthesis at intervals of 1, 3, 6, and 24 hours. We collected precipitate from the room temperature synthesis at 24 hours for XRD analysis. At each time interval we removed 25 mL of solution from the reaction flask and filtered it using a 0.2 μm syringe filter. About 10 mL of NANOpure water was pushed through the filter to remove iron-sulfate salts. XRD samples were prepared by suspending the precipitate in ethanol and pouring it on to either a zero-background quartz or zero-background silicon

plate and left to air dry at room temperature. Samples were run on a PANalytical X'Pert PRO X-ray diffraction system with Cu K-alpha radiation (45kV-40mA) from 5.06° 2θ to 69.916° 2θ with step size 0.067°.

Samples for transmission electron microscopy (TEM) were prepared from the precipitate collected for the XRD analysis. The precipitate was suspended in ethanol and placed in a sonicating bath for 2 minutes. A droplet of the suspension was placed on a gold TEM grid with a lacey carbon support film and the excess liquid was wicked away with a Kimwipe®. The TEM grids were stored in a desiccator under vacuum until analysis. Transmission electron micrographs and selected area diffraction (SAED) patterns were collected on a Philips EM420 operating at 120kV. HRTEM images were collected on a FEI Titan operating at 300 kV. HRTEM images were analyzed using Fourier Transform (FT) in Digital Micrograph^{TM} software program with supplemental software (SADP Tools (Wu et al., submitted)) to measure d-spacings from FT images. Where possible, lattice fringes were directly measured by hand using ImageJ (Abramoff et al., 2004), corroborating d-spacings determined from FT analysis. Samples were found to be stable under the beam of the 300 kV FEI Titan during the time needed to collect an image (less than 1 minute). Extended alignment and focusing were performed elsewhere on the sample from where images were collected for analysis. Comparing images of deliberate damage to the sample (supplemental info. Figure A.S1) with images used for our study make us confident that all TEM images shown in this study represent undamaged schwertmannite needles.

2.3 Results and Discussion

2.23 XRD and morphology characterization of schwertmannite produced at varying temperatures

XRD patterns for schwertmannite produced at room temperature after 24 hours of reaction time and at 75°C for 1 hr of reaction time display broad peaks with low intensity, but the room temperature synthesis shows somewhat more intense peaks (Figure 2.1). The peak at 0.339 nm is much more prominent at room temperature than in the high temperature synthesis. In their study of the structure of schwertmannite, Bigham et al. (Bigham et al., 1990) noted that the 0.339 nm peak decreased in intensity and broadened more than other peaks with the increasing addition of sulfate to a schwertmannite synthesized using $FeCl_3$. This indicated that the 0.339 nm peak was more susceptible to decreasing crystallinity and/or particle size.

TEM images of the bulk aggregates of the schwertmannite spheres (Figure 2.2) show that schwertmannite produced at both temperatures displays the distinctive 'pin cushion' morphology with needles extending from a dense sphere. However, the individual schwertmannite spheres produced at room temperature are on the order of 2-3 times larger than the spheres produced at 75°C and are much more electron dense. The greater electron penetration in the high temperature schwertmannite shows that the needles make up a high proportion of the schwertmannite sphere and there does not appear to be a thick solid core. The morphology of the room temperature schwertmannite suggests that either those needles are nucleating off of an electron dense core or that the schwertmannite solely consists of densely packed needles with a small portion of those needles protruding from the surface. More densely packed needles formed at room

temperature are consistent with a reaction-limited model for crystal growth whereas less densely packed needles formed at 75°C reflect a diffusion-limited model (Waychunas, 2001). At this level of magnification we cannot discern whether schwertmannite needles grow through a nucleation and growth process or through aggregation of nanoparticles (Waychunas, 2001).

2.24 Structure and morphology of schwertmannite as revealed by HRTEM

Selected area electron diffraction (SAED) collected on needles on the surface of the room temperature schwertmannite sphere (supplemental info. Figure A.S2) showed only two highly diffuse rings with the stronger ring corresponding to the most intense 0.255 nm peak in the XRD pattern. The majority of d-spacings measured from lattice fringes observed in our HRTEM images aligned with this most intense peak as well (Figure 2.3 and supplemental info. Figure A.S3). The needles average about 5 nm in diameter and exhibit an atomically rough surface. Lattice fringes, although visible in many areas, do not extend for more than a few nanometers. Areas that do not display lattice fringes can indicate amorphous particles, but they may also be an artifact of overlapping particles or crystals that are not in the correct orientation with respect to the electron beam to give rise to fringes (Janney et al., 2000). Some areas of schwertmannite needles show individual nanoparticles less than 5 nm in diameter with visible lattice fringes (see black circle Figure 2.3B). However, other areas do not contain individual particles and have a poorly ordered structure with lattice fringes in varying orientations. (Figure 2.3A, needle in the upper left or needles in the lower half of the image inset Figure 2.3B).

Although we see evidence of individual nanoparticles forming a single needle, none of the needles viewed on these samples exhibit faceting or direct evidence of oriented attachment. In Hockridge et al.'s study (Hockridge et al., 2009), they observed that the needles were made up of highly faceted goethite nanoparticles with lattice fringes corresponding to the (101) plane of goethite. This peak is absent in the schwertmannite XRD pattern. We did not observe any d-spacings indicative of a (101) plane of goethite. D-spacing measured from lattice fringes visible in our study fell within the most intense peak at 0.255 nm in the schwertmannite XRD pattern. Goethite has intense peaks in this area as well and our d-spacing matches the (111), (400), (011), (210), and (301) planes of goethite (supplemental info. Figure A.S3).

It is well-known from field and laboratory studies that schwertmannite is metastable with respect to goethite (Acero et al., 2006; Burton et al., 2008; Bush et al., 2007; Davidson et al., 2008; Schroth and Parnell, 2005; Schwertmann and Carlson, 2005). The strong correlation between the (301) and (111) reflections for goethite and the 0.255 nm d-spacing measured from the schwertmannite XRD pattern indicates that this may be a plane in the structure of schwertmannite that presents a lower energy pathway for the phase change. In their study on the structure of schwertmannite, Fernandez-Martinez et al. (Fernandez-Martinez et al., 2010) noted that the schwertmannite to goethite transformation requires the release of sulfate and two iron octahedra to form the rectangular channel in goethite from schwertmannite's square channel. The highly defective and strained iron octahedral framework they proposed further eases the transformation from schwertmannite to goethite. Previous studies of minerals at low temperature demonstrated that parent phases formed from the transformation of

metastable precursors have crystal orientations that suggest inherited structural motifs (Hochella and Banfield, 1995), including the biomineralization and transformation of ferrihydrite to goethite under natural conditions (Banfield et al., 2000). Hockridge et al.'s study (Hockridge et al., 2009) showed that ferrihydrite forms part of the schwertmannite structure, however, we did not see evidence of ferrihydrite in this study.

Similar to the schwertmannite produced at room temperature, HRTEM images of schwertmannite produced at 75°C (Figure 2.4) also reveal needles with short-range order, indicated by lattice fringes that extend for 1-2 nm (Figure 2.4A and 2.4B insets). Although individual nanoparticles are not easily discernable, due to the lack of lattice fringes, the surfaces' hill and valley appearance could be the result of the aggregation of rounded nanoparticles. Such features indicated crystal growth by aggregation in previous studies of the formation of iron oxides (Banfield et al., 2000; Burleson and Penn, 2006; Penn et al., 2006). In the few areas where lattice fringes were visible, the measured d-spacings fell within the 0.146, 0.166, 0.195, 0.228, and 0.255 peaks for the schwertmannite XRD pattern, where goethite also has peaks (see supplemental info. Figure A.S4 and A.S5). In both images of Figure 2.4, areas with darker contrast also display some lattice fringes that suggests intermingled areas of crystalline (darker contrast) and amorphous material (lighter contrast), particularly at the base of the needles. This polycrystalline nature was suggested for the nanomineral ferrihydrite as well (Manceau, 2009).

The poorly ordered morphology dominates the needles on the surface of schwertmannite produced at 75°C, but there are also needles that are distinctly more crystalline. We observed a longer and thicker than average needle (150 nm x 20 nm) with

a faceted surface and steps (Figure 2.5A) rather than the rounded hill and valley surface (Figure 2.4). Figure 2.5B shows the end of another needle with about 2 nm particles in diameter aggregated together at the tip, but the individual nanoparticles are not distinguishable away from the tip. Aggregation of these particles may account for the lattice fringes visible within the needle that extend for <1 nm and are not measurable using a FT analysis. SAED of a needle of similar size and morphology showed some individual spots within diffuse rings suggesting a mix of crystalline and amorphous material (supplemental info. Figure A.S6).

These types of needles could be the early stages of the transformation of schwertmannite to goethite. Though fringes were not sufficiently measurable on this needle to allow us to test this hypothesis, Burleson et al. (Burleson and Penn, 2006) observed a crystal growth process that displayed a similar type of morphology as we observed here. They saw a bumpy goethite nanorod, formed by the oriented aggregation goethite nanoparticles, smoothing as the reaction progressed. In this study they observed individual nanoparticles intermingled with their rods, whereas we did not observe individual nanoparticles elsewhere on the surface of the needles. Without measureable lattice fringes it is difficult to conclusively determine whether the needles form from random aggregation or from an oriented attachment mechanism, but the poorly ordered morphology with no visible coherent fringing anywhere in the needle suggests that these do not form via an ion by ion crystal growth mechanism.

2.25 Accelerated transformation from schwertmannite to goethite at 75°C

In our experiments we have shown, for the first time, the complete transformation of schwertmannite to goethite within 24 hours at 75°C as seen in XRD patterns (Figure

2.6). Within 3 hrs characteristic goethite peaks appear (Figure 2.6B), particularly in the (101) reflection that is absent in the schwertmannite XRD pattern (Figure 2.6A). As schwertmannite transforms to goethite, we see the gradual replacement of the thin and elongated schwertmannite needles with shorter, thicker, and more acicular particles on the edges of the schwertmannite spheres (Figure 2.7). The characteristic schwertmannite needles remain visible after 6 hours of reaction time (Figure 2.7B), but after 24 hours they are no longer apparent and goethite nanocrystals dominate (Figure 2.7C). However, the spherical shape of the 'pin cushion' morphology of schwertmannite remains in the aggregates of the goethite nanocrystals (Figure 2.7C).

The goethite observed after 24 hours of reaction time appears to be formed from the aggregation of many individual particles that are 2-4 nm in width and varying length (Figure 2.8). These particles appear as individual particles, but also as rods bundled together to form larger particles. Previous studies showed goethite, synthesized by the oxidation of Fe(II) at room temperature, as "rafts of parallel rods" (Cornell and Schwertmann, 2003), but the rods were at least 10 nm in width. The edges of the goethite aggregates appear similar to the "goethite-like aggregates" observed in TEM images in the Hockridge et al. (Hockridge et al., 2009) study, although individual nanoparticles were not distinguishable in their TEM images of goethite. Hockridge et al. (Hockridge et al., 2009) is the only other study that investigated the evolution of a synthetic schwertmannite over 24 hours at an elevated temperature of 85°C, though they had no synthesis run at a lower temperature for comparison as we did. They did observe incomplete transformation to goethite within the 24 hour period, but only saw a maximum crystallite size of about12 nm in a peak broadening analysis of the (101)

reflection. In our study we observed an intense (101) reflection after 24 hours (Figure 2.6D) that showed about 20 nm crystallite size using a peak broadening analysis. This crystallite size and others calculated from the goethite peaks in our study (Figure 2.6D) agree with the size of the aggregates of the rods and not the primary 2-4 nm particle or rod size that we observe in TEM images (Figure 2.7C and Figure 2.8). According to the Scherrer model, micron-sized particles composed of aggregated nanometer particles should display peak broadening consistent with the nanometer particles (Waychunas, 2001). It therefore seems likely that our peak broadening analysis may have significant error associated with it as we cannot take into account possible structural strain, which affects peak broadening as well. Further investigation using HRTEM would be needed to determine whether these goethite nanorods are made up of crystallographically oriented goethite nanoparticles, but previous studies showed that goethite rods formed in this way (Burleson and Penn, 2006; Penn et al., 2006). Furthermore, goethite nanorods of the size seen in Figure 8 are comparable to the size of the schwertmannite needles (Figure 2.4), indicating that those needles may be a precursor to the formation of the bundled rods.

The fact that the same reaction conditions run at room temperature for 24 hours did not yield a goethite transformation product (Figure 2.1A) shows that increasing temperature to 75°C drives the transformation from schwertmannite to goethite. Interestingly, despite the difference in transformation time and temperature between our study at 75°C and previous work at room temperature (Bigham et al., 1996b; Burton et al., 2006; Schwertmann and Carlson, 2005), the final individual goethite particle size in our study was comparable to those studies and they also observed spherical goethite nanoparticle aggregates.

2.4 Conclusions

Our synthesis demonstrates that increasing temperature and decreasing reaction time produces schwertmannite with the same XRD pattern, but with smaller size and less densely-packed needles than schwertmannite produced at room temperature. Despite the difference in size and morphology at the scale of the entire schwertmannite sphere, the majority of needles from both the room temperature and 75°C synthesis are about 5 nm in width and contain areas of amorphous and poorly ordered material. However, some needles on the 75°C synthetic schwertmannite already appeared to be forming thicker and more crystalline rods relative to the 5 nm nanoneedles, though this difference was not reflected in the XRD patterns. The formation of these thicker needles was possibly the beginning step in the transformation of schwertmannite to goethite, which proceeds rapidly with complete transformation within 24 hours at 75°C.

HRTEM images in this study reveal, for the first time, that atomic scale structure may be different across synthetic schwertmannites, despite similar XRD patterns. The variations in atomic structure between the mix of amorphous and poorly ordered material composing the schwertmannite needles in this study and the needles composed of goethite nanocrystals in the Hockridge et al. (Hockridge et al., 2009) study may result in significant differences in reactivity between the two schwertmannites. Variations in atomic structure of other iron oxides, as a function of particle size, has been shown to affect the catalytic oxidation of manganese by hematite (Madden and Hochella, 2005), the hydroquinone-driven reductive dissolution of goethite (Anschutz and Penn, 2005), and hematite's sorption capacity for copper (Madden et al., 2006). Our study underscores the importance of using HRTEM to characterize nanominerals in addition to XRD in

order to fully understand variations in atomic structure and their resultant changes in reactivity.

The rapid transformation from schwertmannite to goethite with a 50°C increase in temperature demonstrates the highly metastable nature of schwertmannite. However, schwertmannite remains stable at room temperature for months to years (Bigham et al., 1996b; Jonsson and Lovgren, 2006; Knorr and Blodau, 2007; Schwertmann and Carlson, 2005). This shows that though the energetic barriers to transformation may be small, the thermodynamically favored phase is not always what you will find in a natural system. The metastability of precursor nanomaterials with respect to thermodynamically favored products may be a particularly important process in low temperature systems (Navrotsky, 2004). This has been displayed in the case of polymorphs within a given material, for example, calcium carbonates and titania, where the metastable polymorphs have a lower surface enthalpy with increasing surface area. Surface area also increases with a decrease in particle size, making metastable nanoparticles the more energetically favorable phase initially in crystal growth processes. This model is consistent with our results showing that schwertmannite, a nanomineral, is a precursor to goethite. However, this model only deals with materials that have the same chemical makeup, whereas sulfate is a component of schwertmannite, but it is not part of the goethite structure. This model also suggests that a dissolution and reprecipitation process and/or "separate nucleation events" are required to form the next stable phase. The lattice fringes that match goethite in the HRTEM images of the schwertmannite (Figure 2.3 and 2.4) suggest that this transformation may occur within the needles as a structural rearrangement. Similar processes have been observed in the transformation of ferrihydrite nanoparticles to

goethite (Banfield et al., 2000). In that study researchers found that the ferrihydrite nanoparticles that were randomly aggregated eventually align and grow through oriented attachment. Furthermore, the ferrihydrite nanoparticles contained many defects suggesting that they were likely formed from the aggregation of subnanometer-scale clusters, which would be formed from the aggregation of aqueous ions. The presence of intermingled areas of amorphous material and crystalline areas in our study suggests that schwertmannite may form through a similar pathway as that of the ferrihydrite in the Banfield et al. (Banfield et al., 2000) study. Though we did not observe oriented attachment in the early stages of schwertmannite formation and transformation, oriented attachment could be a mechanism by which the crystalline areas could transform from schwertmannite to goethite.

Acknowledgments

We thank the ICTAS Nanocharacterization and Fabrication Laboratory (NCFL) at Virginia Tech, the Materials Science and Engineering Nanoscale Materials Characterization Facility (MSE-NMCF) at the University of Virginia, and the Campus Electron Optics Facility (CEOF) at Ohio State University in collaboration with FEI Company for the use of their Titan microscopes. We thank Matthew Eick for helpful comments that greatly enhanced the quality of this paper. Grants from the US Department of Energy (DE-FG02-06ER15786) and the Institute for Critical Technology and Applied Sciences at Virginia Tech provided major financial support for this project. We are also appreciative of the support from the National Science Foundation (NSF) and the Environmental Protection Agency through the Center for Environmental Implications of NanoTechnology (CEINT) funded under NSF Cooperative Agreement EF-0830093.

Fellowship support for this research was provided by the National Science Foundation (NSF IGERT grant DGE-0504196). Any opinions, findings, and conclusions or recommendations expressed in this material are those of the authors and do not necessarily reflect the views of NSF, EPA, or DOE.

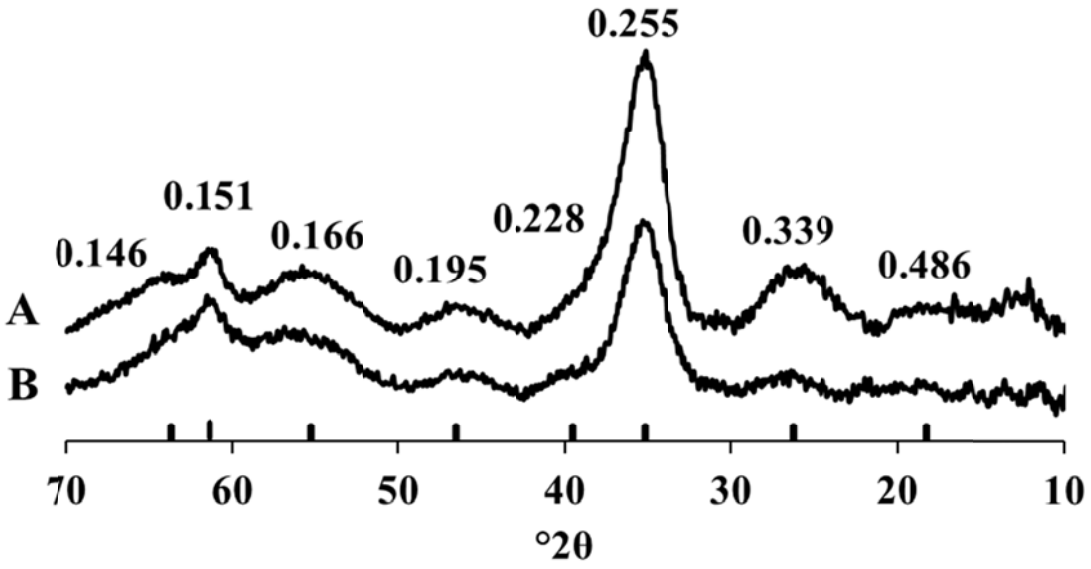

Figure 2.1. *XRD patterns of precipitates synthesized at room temperature for 24 hrs (A) and at 75°C for 1 hr (B). Peak locations (black lines) and d-spacings (nm) for schwertmannite (Bigham et al., 1994) shown for reference.*

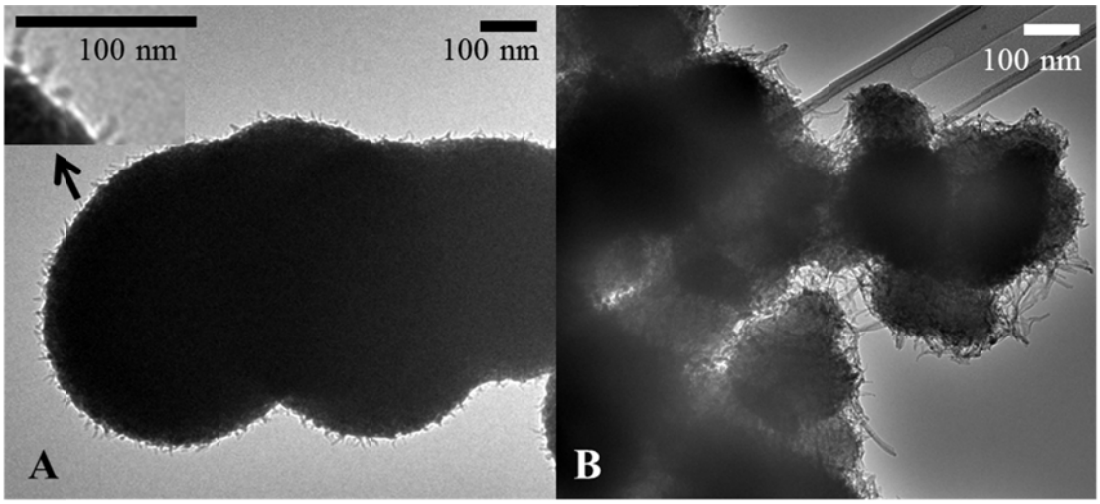

Figure 2.2. *(A) Schwertmannite aggregate produced in room temperature synthesis and (B) aggregate of schwertmannite produced at 75°C for 1hr reaction time. Scale bars = 100 nm.*

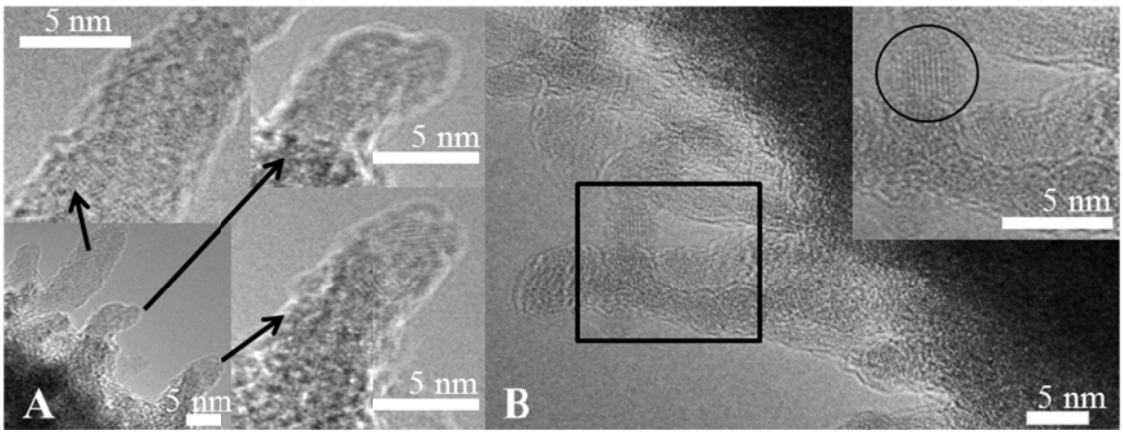

Figure 2.3. *Needles at the surface of the same schwertmannite sphere produced in the room temperature synthesis for 24 hrs.*

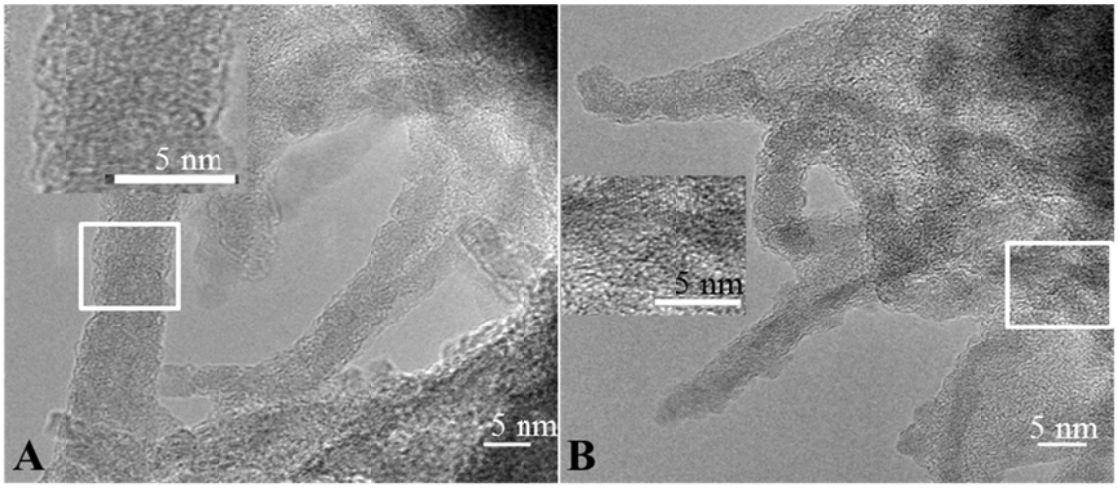

Figure 2.4. *Needles on the surface of schwertmannite particles produced at 75°C for 1 hr.*

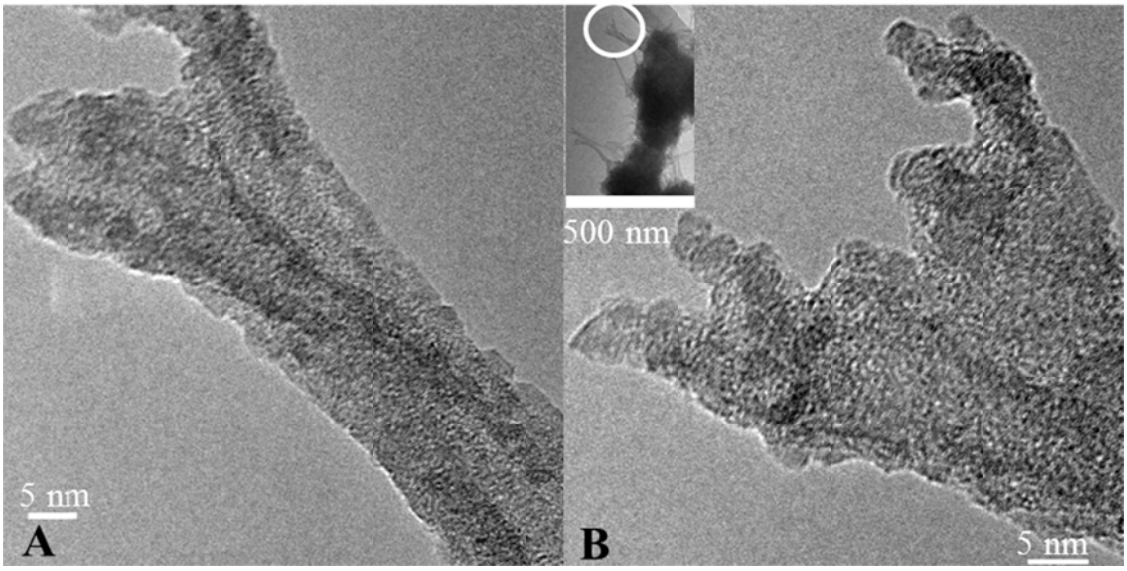

Figure 2.5. *Needles on the surface of schwertmannite particles formed at 75°C for 1 hr reaction time. (B) Tip of the needle seen in the inset.*

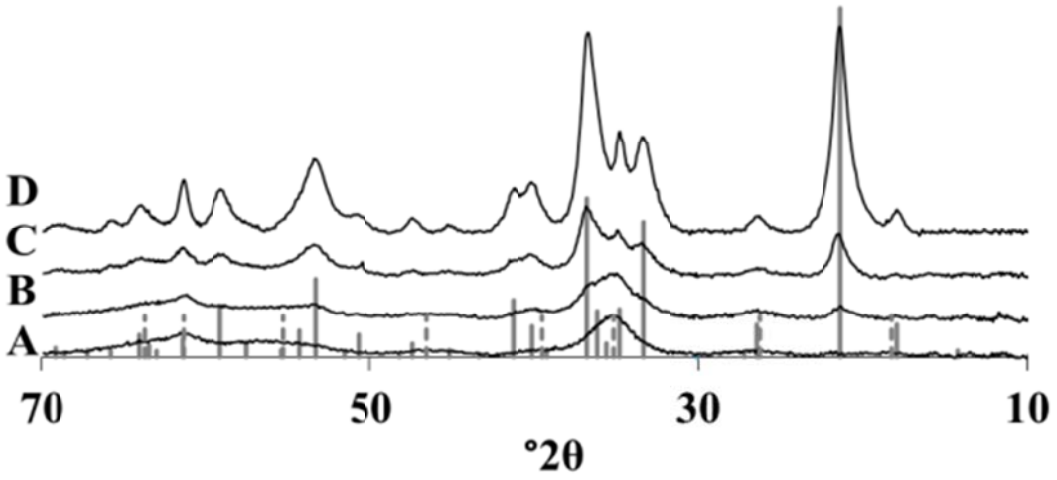

Figure 2.6. *XRD patterns showing the transformation from schwertmannite to goethite at 75°C. (A) 1 hr, (B) 3 hrs, (C) 6 hrs, and (D) 24 hrs. Schwertmannite (Bigham et al., 1994) (dotted grey lines) and goethite standard (solid grey lines) on the XRD patterns are shown for reference.*

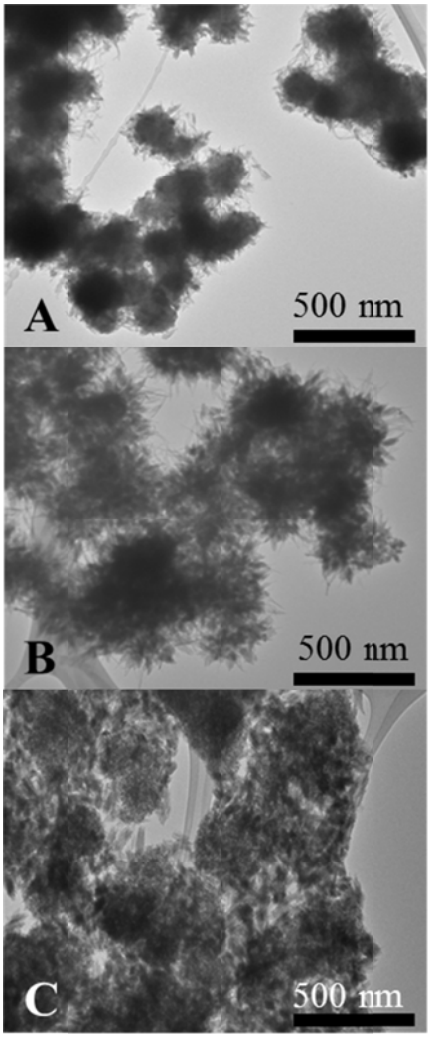

Figure 2.7. *TEM images of sample collected at (A) 3 hrs, (B) 6 hrs, (C) 24 hrs.*

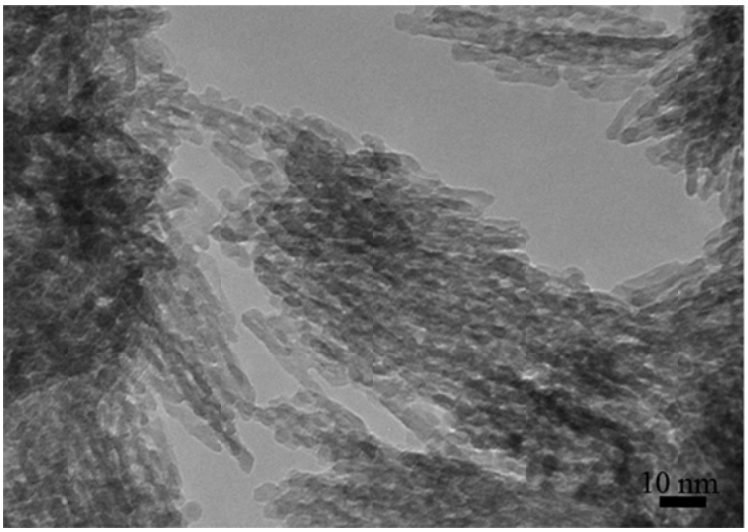

Figure 2.8. *Goethite from synthesis run for 24 hrs at 75°C.*

References

Abramoff, M.D., Magalhaes, P.J., and Ram, S.J. (2004) Image processing with ImageJ. Biophotonics International, 11(7), 36-42.

Acero, P., Ayora, C., Torrento, C., and Nieto, J.M. (2006) The behavior of trace elements during schwertmannite precipitation and subsequent transformation into goethite and jarosite. Geochimica Et Cosmochimica Acta, 70(16), 4130-4139.

Anschutz, A.J., and Penn, R.L. (2005) Reduction of crystalline iron(III) oxyhydroxides using hydroquinone: Influence of phase and particle size. Geochemical Transactions, 6(3), 60-66.

Banfield, J.F., Welch, S.A., Zhang, H.Z., Ebert, T.T., and Penn, R.L. (2000) Aggregation-based crystal growth and microstructure development in natural iron oxyhydroxide biomineralization products. Science, 289(5480), 751-754.

Barham, R.J. (1997) Schwertmannite: A unique mineral, contains a replaceable ligand, transforms to jarosites, hematites, and/or basic iron sulfate. Journal of Materials Research, 12(10), 2751-2758.

Bigham, J.M., Schwertmann, U., Carlson, L., and Murad, E. (1990) A poorly crystallized oxyhydroxysulfate of iron formed by bacterial oxidation of Fe(II) in acid-mine waters. Geochimica Et Cosmochimica Acta, 54(10), 2743-2758.

Bigham, J.M., Carlson, L., and Murad, E. (1994) Schwertmannite, a new iron oxyhydroxysulphate from Pyhasalmi, Finland, and other localities. Mineralogical Magazine, 58(393), 641-648.

Bigham, J.M., Schwertmann, U., and Pfab, G. (1996a) Influence of pH on mineral speciation in a bioreactor simulating acid mine drainage. Applied Geochemistry, 11(6), 845-849.

Bigham, J.M., Schwertmann, U., Traina, S.J., Winland, R.L., and Wolf, M. (1996b) Schwertmannite and the chemical modeling of iron in acid sulfate waters. Geochimica Et Cosmochimica Acta, 60(12), 2111-2121.

Bigham, J.M., and Nordstrom, D.K. (2000) Iron and aluminum hydroxysulfates from acid sulfate waters. In C.N. Alpers, J.L. Jambor, and D.K. Nordstrom, Eds. Sulfate Minerals-Crystallography, Geochemistry and Environmental Significance, 40, p. 351-403. Mineralogical Society of America, Washington, DC.

Burleson, D.J., and Penn, R.L. (2006) Two-step growth of goethite from ferrihydrite. Langmuir, 22(1), 402-409.

Burton, E.D., Bush, R.T., and Sullivan, L.A. (2006) Sedimentary iron geochemistry in acidic waterways associated with coastal lowland acid sulfate soils. Geochimica Et Cosmochimica Acta, 70(22), 5455-5468.

Burton, E.D., Bush, R.T., Sullivan, L.A., and Mitchell, D.R.G. (2007) Reductive transformation of iron and sulfur in schwertmannite-rich accumulations associated with acidified coastal lowlands. Geochimica Et Cosmochimica Acta, 71(18), 4456-4473.

Burton, E.D., Bush, R.T., Sullivan, L.A., and Mitchell, D.R.G. (2008) Schwertmannite transformation to goethite via the Fe(II) pathway: Reaction rates and implications for iron-sulfide formation. Geochimica Et Cosmochimica Acta, 72(18), 4551-4564.

Bush, R., Burton, E., and Sullivan, L. (2007) Catalytic action of aqueous Fe(II) and S(II) on the transformation of schwertmannite to goethite. Geochimica Et Cosmochimica Acta, 71(15), A137-A137.

Claassen, J.O., Meyer, E.H.O., Rennie, J., and Sandenbergh, R.F. (2002) Iron precipitation from zinc-rich solutions: defining the Zincor Process. Hydrometallurgy, 67(1-3), 87-108.

Cornell, R.M., and Schwertmann, U. (2003) The Iron Oxides. Wiley-VCH, Weinheim.

Davidson, L.E., Shaw, S., and Benning, L.G. (2008) The kinetics and mechanisms of schwertmannite transformation to goethite and hematite under alkaline conditions. American Mineralogist, 93(8-9), 1326-1337.

Espana, J.S., Pamo, E.L., Santofimia, E., Aduvire, O., Reyes, J., and Barettino, D. (2005) Acid mine drainage in the Iberian Pyrite Belt (Odiel river watershed, Huelva, SW Spain): Geochemistry, mineralogy and environmental implications. Applied Geochemistry, 20(7), 1320-1356.

Fernandez-Martinez, A., Timon, V., Roman-Ross, G., Cuello, G.J., Daniels, J.E., and Ayora, C. (2010) The structure of schwertmannite, a nanocrystalline iron oxyhydroxysulfate. American Mineralogist, 95, 1312-1322.

Hochella, M.F., and Banfield, J.F. (1995) Chemical weathering of silicates in nature: a microscopic perspective with theoretical considerations. In A.F. White, and S.L. Brantley, Eds. Chemical weathering rates of silicate minerals, 31, p. 353-406. The Mineralogical Society of America, Washington, DC.

Hochella, M.F., Lower, S.K., Maurice, P.A., Penn, R.L., Sahai, N., Sparks, D.L., and Twining, B.S. (2008) Nanominerals, mineral nanoparticles, and Earth systems. Science, 319(5870), 1631-1635.

Hockridge, J.G., Jones, F., Loan, M., and Richmond, W.R. (2009) An electron microscopy study of the crystal growth of schwertmannite needles through oriented aggregation of goethite nanocrystals. Journal of Crystal Growth, 311(15), 3876-3882.

Janney, D.E., Cowley, J.M., and Buseck, P.R. (2000) Structure of synthetic 2-line ferrihydrite by electron nanodiffraction. American Mineralogist, 85(9), 1180-1187.

Jonsson, J., Persson, P., Sjoberg, S., and Lovgren, L. (2005) Schwertmannite precipitated from acid mine drainage: phase transformation, sulphate release and surface properties. Applied Geochemistry, 20(1), 179-191.

Jonsson, J., and Lovgren, L. (2006) Precipitation of secondary Fe(III) minerals from acid mine drainage. Applied Geochemistry, 21(3), 437-445.

Knorr, K.H., and Blodau, C. (2007) Controls on schwertmannite transformation rates and products. Applied Geochemistry, 22(9), 2006-2015.

Loan, M., Cowley, J.M., Hart, R., and Parkinson, G.M. (2004) Evidence on the structure of synthetic schwertmannite. American Mineralogist, 89(11-12), 1735-1742.

Madden, A.S., and Hochella, M.F. (2005) A test of geochemical reactivity as a function of mineral size: Manganese oxidation promoted by hematite nanoparticles. Geochimica Et Cosmochimica Acta, 69(2), 389-398.

Madden, A.S., Hochella, M.F., and Luxton, T.P. (2006) Insights for size-dependent reactivity of hematite nanomineral surfaces through Cu2+ sorption. Geochimica Et Cosmochimica Acta, 70(16), 4095-4104.

Manceau, A. (2009) Evaluation of the structural model for ferrihydrite derived from real-space modelling of high-energy X-ray diffraction data. Clay Minerals, 44(1), 19-34.

Michel, F.M., Ehm, L., Antao, S.M., Lee, P.L., Chupas, P.J., Liu, G., Strongin, D.R., Schoonen, M.A.A., Phillips, B.L., and Parise, J.B. (2007) The structure of ferrihydrite, a nanocrystalline material. Science, 316(5832), 1726-1729.

Navrotsky, A. (2004) Energetic clues to pathways to biomineralization: Precursors, clusters, and nanoparticles. Proceedings of the National Academy of Sciences of the United States of America, 101(33), 12096-12101.

Penn, R.L., Erbs, J.J., and Gulliver, D.M. (2006) Controlled growth of alpha-FeOOH nanorods by exploiting-oriented aggregation. Journal of Crystal Growth, 293(1), 1-4.

Regenspurg, S., Brand, A., and Peiffer, S. (2004) Formation and stability of schwertmannite in acidic mining lakes. Geochimica Et Cosmochimica Acta, 68(6), 1185-1197.

Schroth, A.W., and Parnell, R.A. (2005) Trace metal retention through the schwertmannite to goethite transformation as observed in a field setting, Alta Mine, MT. Applied Geochemistry, 20(5), 907-917.

Schwertmann, U., and Cornell, R.M. (1991) Iron oxides in the laboratory: Preparation and characterization. Wiley-VCH, New York.

Schwertmann, U., and Carlson, L. (2005) The pH-dependent transformation of schwertmannite to goethite at 25 degrees C. Clay Minerals, 40(1), 63-66.

Waychunas, G.A. (2001) Structure, aggregation and characterization of nanoparticles. In J.F. Banfield, and A. Navrotsky, Eds. Nanoparticles and the environment, 44, p. 105-166. The Mineralogical Society of America, Washington, DC.

Wu, C.H., Murayama, M., and Reynolds Jr., W.T. (submitted) A software tool for automatic analysis of selected area diffraction patterns within Digital Micrograph™. Ultramicroscopy.

Zinck, J.M., and Dutrizac, J.E. (1998) Environment - The behaviour of zinc, cadmium, thallium, tin and selenium during ferrihydrite precipitation from sulphate media. Cim Bulletin, 91(1019), 94-101.

3) Identifying the polyphasic structure, morphology, and arsenic association of the metastable ferric oxyhydroxysulfate nanomineral schwertmannite using analytical high resolution transmission electron microscopy

Rebecca A. French[1,2*], Manuel A. Caraballo[3], Bojeong Kim [1,2], J.D. Rimstidt [2], Mitsuhiro Murayama[4,5], Michael F. Hochella Jr.[1,2]

[1]ICTAS Environmental Nanoscience and Technology Laboratory, Virginia Tech, Blacksburg, VA 24061, U.S.A.
[2]Department of Geosciences, Virginia Tech, Blacksburg, VA 24061, U.S.A.
[3]Geology Department, University of Huelva, Campus "El Carmen", E-21071 Huelva, Spain
[4]ICTAS Nanoscale Characterization and Fabrication Laboratory, Virginia Tech, Blacksburg, VA 24061, U.S.A.
[5]Department of Materials Science, Virginia Tech, Blacksburg, VA 24061, U.S.A.
*Corresponding author e-mail address: rafrench@vt.edu

To be submitted to American Mineralogist

Abstract

Two sets of precipitates collected from stream sediments in the abandoned mine sites Monte Romero (MR) and Tinto Santa Rosa (TSR), in the world's largest known pyrite deposit, the Iberian Pyrite Belt of Spain, were identified using x-ray diffraction (XRD) and bulk digestion as the iron oxyhydroxysulfate nanomineral schwertmannite, and were further studied in great detail using analytical high resolution transmission electron microscopy (HRTEM). HRTEM offers advantages over bulk techniques such as powder-XRD and pair distribution function (PDF) analysis of synchrotron data, in its ability to discern multiple phases within poorly crystalline nanominerals. The samples display schwertmannite's characteristic 'pin-cushion' morphology with needles ranging in length from 100-300 nm long and 5-20 nm in width. Ultramicrotomed thin sections of schwertmannite show that these needles may make up ~36-70% of a schwertmannite spherical particle. Based on extensive HRTEM observations, the authors suggest that schwertmannite should not be described as a single phase mineral with a repeating unit

cell, but as a polyphasic nanomineral with crystalline areas spanning less than a few nanometers within an amorphous matrix. D-spacings measured from lattice fringes within schwertmannite's needles agree with d-spacings of the known transformation products of schwertmannite (goethite and jarosite). This finding implies that the initial stages of schwertmannite transformation occur as a gradual structural reordering at the nanoscale. Energy dispersive x-ray analysis applied across individual needles with ~3 nm spot size resolution reveal a decreasing ratio of sulfur to iron and silica to iron from the surface of the needle to the core with the silica to iron ratio consistently higher than the sulfur to iron ratio. Amorphous silica-rich precipitates were identified on the surface of the TSR schwertmannite. Arsenic is the most abundant trace element in the samples (MR: 0.218(1) wt% and TSR: 0.53(2) wt%). Arsenic in the TSR schwertmannite is associated with crystalline areas within its needle matrix, implying that schwertmannite-derived goethite nanocrystals may be an important transporter of arsenic.

3.1 Introduction

The ferric oxyhydroxysulfate nanomineral schwertmannite ($Fe_8O_8(OH)_{8-x}(SO_4)_x$ ($1<x<1.75$)) was first officially recognized as a mineral in 1994 (Bigham et al., 1994). The proposed structure for schwertmannite was a modified akaganéite structure where sulfate occupies the tunnels formed by the iron polyhedra in a bi-dentate inner-sphere complex, in place of chloride anions as in akaganéite. Fernandez-Martinez et al. (2010) recently refined the positions of iron and oxygens in Bigham et al's (1994) proposed structure using pair distribution function (PDF) analysis of high-energy x-ray total scattering experiments. The authors concluded that schwertmannite consisted of a "highly defective entangled network of structure motifs" as shown in their models. The defects in

the iron polyhedra network would result in a strained structure. Modeling of the synchrotron powder x-ray diffraction (XRD) patterns revealed that the best model structure would contain two inner-sphere and two outer-sphere sulfate anions per unit cell. Although PDF analysis offers advancement in refining the structure of poorly-crystalline nanominerals over XRD, it has limitations. Papers by Manceau (2009, 2010, 2011) have systematically criticized Michel et al.'s (2007; 2010) PDF-derived proposed structure for the nanomineral ferrihydrite saying that the proposed structure violates Pauling's 2nd and 3rd principals. Moreover, Manceau (2011) warns that PDF does not provide sufficient information to obtain unique crystallographic structures of defective minerals and in particular for nanocrystalline materials.

As suggested by the model structure in Fernandez-Martinez et al. (2010), analysis of the schwertmannite structure must also take into account the existence of multiple phases and defective structures. The bulk properties of schwertmannite also imply a non-uniform structure with its range of calculated solubility constants (Bigham et al., 1996b; Kawano and Tomita, 2001; Yu et al., 1999) that result in a pH stability window of pH 2-3 to pH 2-8, depending on the solubility product used (Majzlan et al., 2004). The predictive ability of geochemical models for schwertmannite's stability is further hindered by the fact that schwertmannite forms under the same conditions as ferrihydrite and jarosite, both of which also have a range of calculated solubilities (Bigham et al., 1996b). Furthermore, schwertmannite is a metastable mineral with respect to goethite and jarosite (Acero et al., 2006; Asta et al., 2010a), but the rate of transformation may vary anywhere from hours (Burton et al., 2008) to years (Bigham et al., 1996b; Jonsson et al., 2005; Regenspurg et al., 2004) depending on geochemical conditions. Despite its

unpredictability, researchers continue to incorporate schwertmannite into geochemical models because schwertmannite has been widely found as a precipitate in acid mine drainage (AMD) systems (Bigham et al., 1994; Bigham et al., 1996b; Espana et al., 2005), mine pit lakes (Blodau, 2006; Peine et al., 2000; Regenspurg et al., 2004), and acid-sulfate soils (Burton et al., 2006; Burton et al., 2007). It has also been found in acid oxic microenvironments in glacial and iceberg sediments (Raiswell et al., 2009). Schwertmannite preserved in icebergs may then become a source of bioavailable iron in oceans (Raiswell, 2011). Finally, the same processes that produce schwertmannite in AMD systems may also have occurred on the surface of Mars (Caraballo et al., 2011; Fernandez-Remolar et al., 2004), making schwertmannite a mineral of interplanetary importance.

High resolution transmission electron microscopy (HRTEM), unlike other techniques, allows researchers to discern polyphasic crystal morphology and structure at the nanoscale. Using this technique, researchers showed the existence of non-classical crystal growth mechanisms, such as oriented-attachment of crystalline nanoparticles, in material that would have appeared poorly crystalline or amorphous using XRD analysis (Banfield et al., 2000; Moreau et al., 2004). HRTEM has also been used to evaluate changes to surface structure as a result of mineral nanoparticle size (Chernyshova et al., 2007) and crystal face dependent dissolution of mineral nanoparticles (Liu et al., 2008; Liu et al., 2009). Researchers used analytical-HRTEM to identify mineral nanoparticles carrying toxic trace metals in a river system over long distances that would have otherwise not been predicted (Plathe et al., 2010). It has also proved to be a useful tool in the discovery of new nanophases of minerals (Hochella et al., 1999) and in the fate and

transformation of engineered nanomaterials in waste streams (Kim et al., 2010). Despite the promise that HRTEM shows for giving new insights into schwertmannite's structure and morphology, no studies have applied TEM to natural samples of schwertmannite at the resolution needed to investigate it at the nano- and atomic scale.

In this study we present the first HRTEM images of natural schwertmannite collected from abandoned mine sites in the Iberian Pyrite Belt (IPB) of southwest Spain. The IPB is a world-class site in which to study schwertmannite. The IPB is the largest known sulfide deposit in the world, spanning across the Huelva Province of Spain and continuing into Portugal with an estimated 1700 Mt of sulfide ore, the main mineral of which is pyrite (Saez et al., 1999). Thousands of years of mining these deposits for valuable trace metals left hundreds of abandoned mines and significant pollution as a result of largely unchecked acid mine drainage (Sarmiento et al., 2007). The pollutants drain to the Odiel river basin and the Tinto river and subsequently to the Gulf of Cadíz and the Atlantic ocean. Olías et al. (2006) estimated that the Odiel and Tinto rivers transport 7922 tons/year of Fe and 183,802 tons/year of SO_4, which represents 0.32 % and 0.15 % of the total global riverine flux of these metals. Furthermore, they estimated that these rivers transport 0.15%, 3.13%, and 15.1% of the global riverine flux of As, Cu, and Zn, respectively. A survey of 64 AMD discharges from 25 different mines in the IPB (Espana et al., 2005) determined that schwertmannite was the "most important mineral phase, both in controlling the Fe solubility at pH 2-4, and as a sorbent of the trace elements (As, Cu, Zn)," effectively assigning schwertmannite a significant part of the global metal cycling of these elements, remarkably, from this single region.

The insights provided in this study using HRTEM show that schwertmannite may not be characterized as a single phase mineral with a repeating unit cell, but should be described as a polyphasic nanomineral with crystalline areas spanning less than a few nanometers within an amorphous matrix. The crystalline areas agree with d-spacings of goethite and jarosite, which are known transformation products of schwertmannite, suggesting that the initial stages of transformation occur as a gradual structural reordering at the nanoscale. Finally, we investigate the chemistry of individual needles of schwertmannite using analytical-HRTEM, revealing the distribution of sulfur and arsenic across the needles as well as the presence of amorphous silica precipitates on the surface of schwertmannite.

3.2 Materials and Methods

3.21 Field-site and sampling description

Schwertmannite and water samples were collected from two abandoned mines in the Iberian Pyrite Belt (IPB) of southwest Spain. The Monte Romero (MR) mine contains a massive pyrite deposit rich in Zn, Pb, and Cu sulfides. The enclosing rocks are siliciclastic schists without carbonate beds (Pinedo-Vara, 1963). The main ore of the Tinto Santa Rosa (TSR) mine mainly consists of pyrite, chalcopyrite, and arsenopyrite. After the closure of the mine and recovery of groundwater levels, water began to flow from one of the mine adits and formed the TSR stream. In both mine sites fresh precipitates were collected from the stream bed sediment. In the MR site the iron precipitates appear as fine and loose orange sediment. Iron precipitates in the TSR site have formed iron terraces of iron-rich stromatolites (Perez-Lopez et al., 2011) in the stream bed and samples were collected from the surface of these terraces. To avoid the

presence of aged Fe mineral phases in the deeper sediments, only the top 1-2 cm of the fresh precipitates were collected. The samples were air dried at room temperature in the laboratory to avoid any mineral phase transformation and were ground to a powder using an agate mill.

Water samples were collected near the solid samples. Methods were based on previous field studies on acid mine drainage sites within the IPB (Caraballo et al., 2009; Caraballo et al., 2011). After filtering the water through a 0.1 μm Millipore filter on Millipore syringe filter holders, the samples were acidified in the field to pH 1 with HNO_3 and stored at 4°C in polyethylene bottles until analysis. Temperature and electrical conductivity were measured in the field using a portable CM35 meter (Crison®) with 3 point calibration (147 and 1413 μS cm^{-1} and 12.88 mS cm^{-1}). The pH and redox potential (Eh) were measured using a PH25 meter (Crison®) with Crison electrodes. Eh and pH were controlled and calibrated using 2 points (240–470 mV) and 3 points (pH 4.01–7.00–9.21), respectively, with Crison standard solutions. An auto-calibrating Hanna® portable meter was used to measure dissolved O_2.

3.22 Total extractable metal analysis

Concentrations of dissolved Al, As, Ca, Cd, Co, Cr, Cu, Fe, K, Mg, Mn, Ni, Pb, S, Si, Ti, V, and Zn in the water samples were determined by Inductively Coupled Plasma Atomic Emission Spectrometry (ICP-AES Jobin-Ybon Ultima2) using a protocol especially designed for AMD samples (Tyler et al., 2004). Analysis was performed at the Central Research Services at the University of Huelva (CRSUH). Multi-element standard solutions (SCP SCIENCE) were run at the beginning and end of each analytical series for calibration. Certified Reference Material SRM-1640 NIST freshwater- type and inter-

laboratory standard IRMM-N3 wastewater test materials (European Commission Institute for Reference Materials and Measurements) were also analyzed. No significant differences were found between the certified values and the experimental concentrations measured. Detection limits were calculated by average and standard deviations from 10 blanks. Detection limits were: 0.200 mgL^{-1} for Al, Fe, Mn, Mg, Si and S; 0.5 $mgL^{-1}$for Ca; 0.05 $mgL^{-1}$for Zn; 0.005 mgL^{-1} for Cu; 0.002 mgL^{-1} for As and 0.001 mgL^{-1} for the other trace elements.

The iron precipitates were first digested using concentrated HNO_3. About 0.05 grams of iron precipitates were mixed with 3 mL of HNO_3 (ACS grade) and were left sitting closed at room temperature in digest vessels (CEM MARSXpress^{TM} acid digest vessel) for 3 or more days until colored solids were no longer visible. The samples were then diluted with NANOpure® water (Barnstead, 18.2MΩ-cm water with 1-5 ppb TOC) to a total volume of 25 mL. The samples were analyzed using ICP-AES (Spectro ARCOS ICP Model FHS16, Virginia Tech Soil Testing Laboratory) for the concentrations of Al, As, Ca, Cd, Co, Cr, Cu, Fe, K, Mg, Mn, Ni, Pb, S, Si, Ti, V, and Zn. Calibration standards were prepared for each single element within the matrix solution of 12% HNO_3. A blank with 12% HNO_3 was run as well and all analyzed metals were below detection limits. Quality Control (QC) standards with a "Certificate of Analysis" were prepared from multielement standards that are used for verification of instrument accuracy and precision throughout the analysis. A QC check of 90-110% of the true value is considered acceptable. White solids, most likely silicates that would not be dissolved by a nitric acid digestion, were visible in the MR samples. These solids were filtered out of solution using a 0.1μm syringe filter (Acrodisc®, Supor® membrane) before ICP-AES

analysis. Three replicates were analyzed for each sample and the concentration was reported as the average and twice the standard deviation or the 95% confidence interval. Detection limits were Al 0.006 mgL^{-1}, As 0.017 mgL^{-1}, Ca 0.051 mgL^{-1}, Cd 0.004 mgL^{-1}, Co 0.007 mgL^{-1}, Cr mgL^{-1}, Cu 0.007 mgL^{-1}, Fe 0.007 mgL^{-1}, K 0.041 mgL^{-1}, Mg 0.036 mgL^{-1}, Mn 0.003 mgL^{-1}, Na 0.016 mgL^{-1}, Ni 0.006 mgL^{-1}, Pb 0.016 mgL^{-1}, S 0.051 mgL^{-1}, Si 0.065 mgL^{-1}, Ti 0.011 mgL^{-1}, and Zn 0.006 mgL^{-1}. This digestion method will not completely dissolve silicate minerals and therefore the total metal analysis in this study would not reflect the total amount of the elements in these minerals (e.g. Si, Al, Fe, K, Mg, Ca, etc.).

3.23 Geochemical modeling

The equilibrium geochemical speciation/mass transfer model PHREEQC (Parkhurst, 1995) with the database of the speciation model MINTEQ (Ball and Nordstrom, 1991) was used to calculate the saturation indices (SI) of possible iron oxide phases in the field sites and the aqueous speciation of metals in the water samples. Zero, negative, or positive SI values predict whether the field sites were in equilibrium, undersaturated, or supersaturated, respectively, with goethite, ferrihydrite, jarosite, and schwertmannite.

3.24 Powder x-ray diffraction

The purity of the schwertmannite samples was determined using powder x-ray diffraction on a PANalytical X-pert PRO diffractometer with a Cu K-alpha (45kV-40mA) radiation. Analysis was performed from 10.004° 2θ to 79.976° 2θ with step size 0.017°.

3.25 Transmission Electron Microscopy (TEM) sample preparation and mounting

TEM ultramicrotomed thin sections of schwertmannite were prepared as follows. Subsamples of the selected schwertmannite were mixed with NANOpure® water in a 2-mL centrifuge tube, and were then dehydrated by applying a series of ethanol solutions from graded 15% to 100% ethanol:water. After completing dehydration, the precipitates were placed in 100% propylene oxide for 15 minutes, followed by infiltration with a suspension of propylene oxide and Poly/Bed 812 (50:50 (v:v)) and left overnight. On the following day, the samples were again subjected to infiltrate with 100% of Poly/Bed 812 and left to sit overnight. The following day, the samples were embedded in a flat mold using freshly prepared 100% Poly/Bed 812. The mold was then cured in an oven set at 60°C for at least 48 hours. Ultra-thin sections were obtained by ultramicrotome using a diamond knife and approximately 60-90 nm thick sections were collected on a Cu or Au TEM grid with a lacey carbon support film.

Whole schwertmannite aggregate TEM samples were prepared in two ways: 1) Iron precipitates were suspended in NANOpure® water and placed in a sonicating bath for 5 minutes to disperse aggregates, 2) Iron precipitates were suspended in ethanol and placed in a sonicating bath for 2 minutes to disperse aggregates. In both sample preparations a droplet of sample was placed on a Cu or Au TEM grid with a lacey carbon support film and wicked dry with a Kimwipe®. TEM grids were then placed in a desiccator under vacuum until analysis. There were no differences observed in TEM images collected on schwertmannite prepared using these two sample preparation methods.

3.26 Microscopy and chemical analysis

Whole schwertmannite aggregates on TEM grids, as prepared above, were scanned for arsenic using an environmental scanning electron microscope (ESEM) (FEI Quanta 600 FEG) with energy dispersive x-ray spectroscopy (EDX) (Bruker QUANTAX 400) operating at 20 kV. This technique allowed us to locate samples with a sufficiently high arsenic concentration that would be detectable on the EDX on TEM. Seventy four aggregates of schwertmannite from the TSR mine site, displaying the characteristic 'pin-cushion' morphology and strong Fe and S signals, were scanned. Approximately 70% of those aggregates showed an L peak for arsenic indicating that arsenic was present at detectable levels in those aggregates. Silica was not detectable above background levels using ESEM/EDX. Images of the grid location of each schwertmannite aggregate were collected to locate the same aggregate during TEM analysis.

TEM imaging and EDX analysis was performed on an FEI Titan 300 operating at 200 kV (ICTAS NCFL, Virginia Tech), FEI Titan 300 TEM operating at 300 kV (Dept. Materials Science & Engineering, Univ. of Virginia), and an FEI Titan3 operating at 300 kV with (FEI demo lab, CEOF Ohio State Univ.). EDX data was analyzed with FEI TEM Imaging and Analysis software. Analysis of EDX peaks was performed with a background correction that uses a multi-polynomial fit of background bremsstrahlung radiation, which is caused by deceleration of incident electrons. The characteristic peaks were fitted with a Gaussian curve and peak intensity was recorded. The default setting on the software recognizes peaks as significant only if they are 6 times higher than the background intensity. Ratios of Si:Fe, S:Fe, and As:Fe were calculated based on the integrated intensity of x-rays in the EDX spectra characteristic of K-shell electrons. Silica

and sulfur have adjacent peaks in the EDX spectra and have k-factors that are very close to one. The ratios of S:Fe and Si:Fe may therefore be directly compared as relative concentrations of the elements. Absolute concentrations of elements were not measureable due to unknown sample thickness.

Individual needles on the surface of schwertmannite particles were analyzed by focusing the beam to a ~3 nm spot and collecting EDX data at that point. The beam was then manually moved to an adjacent area and data was again collected. The structure of the schwertmannite sample was significantly damaged during analysis (Figure B.S1), but the small amounts of material in the needles at this resolution necessitated this approach in order to obtain sufficient signal for analysis. TEM images were collected on the undamaged schwertmannite areas before EDX data collection in order to correlate needle morphology with chemical information.

3.3 Results and Discussion

3.31 Field site and bulk schwertmannite mineralogy and chemical analysis

The water chemistry and metal content of the stream water in MR and TSR sites (Table 3.1 and 3.2) create conditions that favor schwertmannite formation in the IPB, with a low pH between 2 and 4, oxic conditions, and high dissolved sulfate and iron (Espana et al., 2005). Saturation indices calculated using PHREEQC for the mines sites (Table 3.2) shows that using the Bigham et al. (1996b) solubility constant, the sites are undersaturated with respect to schwertmannite, whereas using the solubility constants derived by Yu et al. (1999) and Kawano and Tomita (2001) predicts that the sites are near saturation or supersaturated with respect to schwertmannite. Calculations also predict that both sites are supersaturated with respect to goethite and that the MR site is

supersaturated with respect to K-jarosite and H_3O-jarosite. Previous studies on the MR site and TSR site also found that the smaller solubility constants more accurately reflected the mineralogy of the field site and H_3O-jarosite was the identified jarosite phase (Acero et al., 2006; Asta et al., 2010b).

Schwertmannite collected at the TSR and MR sites exhibits the characteristic x-ray diffraction pattern for schwertmannite with broad peaks, although the peak at 0.486 nm was too weak to distinguish in our XRD analysis (Figure 3.1). However, Perez-Lopez et al. (unpublished) identified all 8 peaks of these same schwertmannite samples using synchrotron micro-XRD. The two XRD patterns in Figure 3.1 are nearly identical with the center of the peaks aligning, but the MR spectra exhibits lower peak intensity, most visible in the peak at 0.255 nm.

Bulk digestion of the schwertmannite samples showed that the most abundant elements were iron and sulfur with approximately the same average weight percent of each element for both samples (Table 3.3). If we use the model structure for schwertmannite (Bigham et al., 1994; Yu et al., 1999) and hold the number of atoms of Fe and O as a constant of 16 atoms, then we can calculate the formula for schwertmannite for the MR as $Fe_{16}O_{16}(OH)_{8.68}(SO_4)_{3.66}$ and for the TSR schwertmannite as $Fe_{16}O_{16}(OH)_{8.72}(SO_4)_{3.64}$. The number of sulfates in this formula is in good agreement with the model proposed by Fernandez-Martinez et al. (2010) with two outer-sphere and two inner-sphere complexes of sulfate per unit cell.

After iron and sulfur, arsenic was the most abundant element in both samples and is an order of magnitude higher in concentration than any other element in the precipitates with the exception of aluminum in the MR schwertmannite and calcium in

the TSR schwertmannite. Comparing the concentration of arsenic in the water samples to the concentration in the schwertmannite, we see that the MR and TSR schwertmannite contain, respectively, greater than 25,500 and 6000 to 7000 times the arsenic concentration of the stream water. Previous field studies on the MR and TSR sites also showed that schwertmannite was the major sink for arsenic (Acero et al., 2006; Asta et al., 2010b).

3.32 Characterization of schwertmannite morphology and needle structure

Needles on the surface of the MR schwertmannite measure approximately 150-250 nm in length and 5-20 nm in width (Figure 3.2A), which falls within the range of reported needle length from previous studies (Bigham and Nordstrom, 2000). It is difficult though to define where a particular needle begins as the needles become more closely packed as you move from the surface to the core of a schwertmannite particle. In the core the bundles of needles are too electron dense to differentiate between them. Many needles appear to consist of two or more separate needles at the base, but then grow together to form a single tip. The needles are also tapered and become thinner from the center of the schwertmannite particle to the surface. They do not exhibit any faceting and appear rounded at the tips.

The TSR schwertmannite has shorter and wider needles than the MR schwertmannite (Figure 3.2B). The needle length, measured from the intersection of two needles to the tip (see arrow Figure 3.2B for example) is <50 nm. However, if the length is measured from a more electron dense area to the edge of the darkest part of the TEM image, then the needles measure approximately 100-150 nm in length (see dotted line

Figure 3.2B for example). The width of the needles, 5-20 nm is approximately the same for both the MR and TSR schwertmannite samples.

In cross section view, the longer needles on the MR schwertmannite particle are 250-300 nm long (Figure 3.2C), whereas needles on the TSR schwertmannite particle are 30-50 nm long (Figure 3.2D). Other TSR schwertmannite images (supplemental Figure B.S2) also showed schwertmannite with longer needles on the same length scale as the MR schwertmannite, indicating heterogeneous needle length across schwertmannite particles.

To date no one has been able to determine whether or not schwertmannite has a solid core or is made up of densely packed needles (Loan et al., 2004). In the MR schwertmannite (Figure 3.2C), features that resemble densely packed needles (e.g. porous areas shown by a darker contrast) extend ~200 nm from the base of the needles into the core. Assuming a spherical particle and that this schwertmannite particle was cut at the center of the sphere, the needles would make up greater than 70% of the volume of the schwertmannite particle. In the TSR schwertmannite, the needles extend ~50 nm into the core, yielding a needle volume of 36% of the entire schwertmannite particle. This estimate does not intend to imply that needles do not make up the entire core of the schwertmannite particle, but to demonstrate that a high proportion of the volume of schwertmannite aggregates are made up of needles. Investigating the structure of the entire core of schwertmannite remains a continuing challenge as obtaining a sufficiently thin sample and artifacts from beam interaction with the resin prevented us from examining structural motifs (e.g. lattice fringes, etc.) on these samples using HRTEM.

The uniform contrast seen in the needles of the MR schwertmannite at lower magnifications (Figure 3.2A) is reflected at higher magnifications where we may observe the morphology of schwertmannite with atomic resolution. A single needle from the area shown in Figure 3.2A is pictured in Figure 3.3. The edges and tip of the needle do not display any distinct facets and have an atomically rough surface. There are no lattice fringes that extend throughout the needle, but rather the lattice fringes extend out for distances of only 2-3 nm. This suggests an assemblage of small nanocrystals, but no edges of individual particles are visible within the needle. One area in the needle displays measureable lattice fringes that do not correlate with any schwertmannite peak in the XRD pattern , but the d-spacing does match the spacing for the (101) plane of goethite (supplemental info. Figure B.S3).

A thicker schwertmannite needle (Figure 3.4 left) from another schwertmannite particle from the MR site (supplemental Figure B.S8) displays the highly disordered nature of the schwertmannite. No individual spots are discernable within the FT pattern, only a broad ring (Figure 3.4 left inset). The width of the ring gives a range of d-spacings that overlap with the most intense peak of the schwertmannite XRD pattern. FT analysis on another needle from the same MR schwertmannite particle (Figure 3.4 right) displays a single pair of bright spots within the otherwise noisy pattern that also falls within the intense 0.255 nm peak for schwertmannite. Water chemistry data (Table 3.2) indicates that this site is supersaturated with respect to goethite and jarosite, both of which have planes with d-spacings that could match the d-spacing of the FT spots as well (Table 3.4). Noisy areas in the FT pattern could be due to a poorly ordered structure, crystals that are

not oriented correctly with respect to the incident electron beam to diffract, and/or overlapping crystals (Janney et al., 2000).

The TSR schwertmannite displays differences in crystallinity between a needle (seen by the darker contrast) and the space between the two needles (no visible fringes and lighter contrast) (Figure 3.5 and 3.2B). FT analysis of crystalline areas reveals that most of the lattice fringes fall within the 0.255 nm and 0.228 nm XRD peaks for schwertmannite and goethite reflections in those areas (Table 3.5 and 3.6). One lattice fringe that falls within the XRD peak at 0.339 nm had no matching goethite plane, but H_3O-jarosite does have its second and third most intensely diffracting planes that could match this d-spacing (Table 3.5). Geochemical modeling (Table 3.2) did not predict that these sites were supersaturated with respect to H_3O-jarosite −hence this phase is not shown in Tables 3.5 and 3.6−, but H_3O-jarosite has been observed in other field studies on the TSR site (Asta et al., 2010b). One set of lattice fringes visible near the base of the needle (Figure 3.5 inset, left image; Table 3.5) has a d-spacing that closely aligns with the 0.486 nm peak of schwertmannite. Goethite's (200) plane has a reflection in the range of this d-spacing. Few areas in any of the needles that we imaged exhibit distinct outlines of individual nanoparticles, but inset area X in Figure 3.7 shows lattice fringes that form the edges of a 5 nm particle within the needle.

At the scale of the bulk sample the schwertmannite from the MR and TSR mine sites appear very similar. Their XRD patterns are nearly identical with matching peak positions and the digestion of the bulk material shows that the iron and sulfur content differs at most by approximately 1 wt %. However, the HRTEM reveals differences between these samples that are not possible to see using bulk anlaysis. The images in this

study show that the TSR schwertmannite samples contain schwertmannite particles with needles that are crystalline with easily visible lattice fringes and with FT analyses displaying multiple bright spots. Though outlines of individual crystals within the needles are not discernable, the blotchy contrast displayed in multiple TSR schwertmannite aggregates in this study (Figure 3.2B, Figure 3.5, supplemental Figure B.S7. Figure B.S8) indicates rounded particles aggregated together. This stands in contrast to the more uniform contrast of the MR schwertmannite needles (Figure 3.3, 3.4 and supplemental Figure B.S8) where lattice fringes are rarely visible and FT patterns exhibit few or no bright spots at all. Unfortunately, due to the practical limits of TEM it is not possible to determine if all schwertmannite particles in both samples would exhibit this same trend, but all images displayed in this study represent the 3 aggregates of schwertmannite, including multiple needles from each of those aggregates, observed from each site. But what gives rise to these differences in morphology and crystallinity? In other words how does schwertmannite form?

If the schwertmannite formed via an ion by ion or molecule by molecule attachment to a growing crystal face, as in the classical model of crystal growth, then there would be crystal faces and coherent lattice fringes across an entire schwertmannite needle. We do not observe this. On the other hand, if the schwertmannite formed entirely from oriented attachment of individual highly crystalline nanoparticles - as has been observed in the formation and transformation of ferrihydrite and goethite (Banfield et al., 2000; Burleson and Penn, 2006; Penn et al., 2007) - then there would be visible individual particles with coherent lattice fringes across individual particles. This is also not observed. Crystallographically oriented particles could exist in these needles, but

their visibility may be obscured due to many overlapping particles (Janney et al., 2000). We observed some schwertmannite needles in the TSR sample with areas with coherent lattice fringes extending for 5-10 nm (Figure 3.5 and 3.6), but lattice fringes in the MR sample were on the order of 1-2 nm in length. If the primary building block were randomly attached 1-2 nm particles for the MR schwertmannite needles, then it is easily conceivable that there would be many overlapping particles, within a needle.

Another possibility is the attachment of surface reacting species (atom, ion, molecule, cluster, or nanoparticle) to form an amorphous material and subsequent aging of these particles to form randomly oriented crystalline particles (Navrotsky, 2004). Which one of these processes predominates in the growth of schwertmannite or whether all of them contribute is not possible to determine from the results of this study. However, an amorphous precursor is more consistent than the previous two models with what we see in the schwertmannite needles. In the TSR schwertmannite crystalline areas are surrounded by incorporated amorphous particles. In the MR schwertmannite we do not see ordering across individual crystal interfaces, but rather in very small areas that appear randomly oriented. We also observe atomically rough surfaces and hill and valley shapes, which is consistent with the morphology of crystals grown by aggregation of nanoparticles (Banfield et al., 2000; Burleson and Penn, 2006). Majzlan and Myneni (2005) found that Fe^{III} oligomers that are hydrogen-bonded to sulfate are present in acid sulfate waters typical of AMD and that these oligomers of varying size are structurally more similar to the proposed structure for schwertmannite than that of goethite, jarosite, or ferrihydrite, explaining why schwertmannite may often be the first mineral to form in AMD systems. Aging of amorphous precursors is a common crystal growth pathway in

biominerals, often observed in the calcium carbonate system (Navrotsky, 2004), but also in iron oxides. For example, in a paper by Chan et al. (2004), they saw bacterial filaments surrounded by amorphous iron oxides. Older filaments contained a 2-3 nm layer of lepidocrocite surrounded by ferrihydrite, leading the authors to believe that these crystals formed from the amorphous iron oxide upon aging.

Once schwertmannite has formed, however, it will eventually transform to goethite and jarosite. Previous field studies on both the MR and TSR sites reported an evolution of schwertmannite to goethite and jarosite in samples taken from the surface precipitates down to the deeper and older sediments (Acero et al., 2006; Asta et al., 2010a). Acero et al. (2006) also observed this transformation from natural schwertmannite to goethite and jarosite in the laboratory, but other studies reported the transformation of synthetic schwertmannite solely to goethite (Bigham et al., 1996b; Burton et al., 2008; Jonsson et al., 2005; Knorr and Blodau, 2007; Regenspurg et al., 2004; Schwertmann and Carlson, 2005). The accepted transformation mechanism is the dissolution of schwertmannite accompanied by simultaneous precipitation of goethite, as evidenced by the release of sulfate and the uptake of hydroxyls from solution (Bigham et al., 1996b).

In this study, the agreement between the d-spacings measured from individual lattice fringes and the d-spacings for goethite and H_3O-jarosite planes suggests that transformation from schwertmannite to goethite may occur as gradual ordering of Fe with aging within the schwertmannite needles. Similar *in situ* transformation processes have occurred in the growth of goethite from oriented attachment of ferrihydrite nanoparticles under low temperature field conditions (Banfield et al., 2000). The kinetics of the

schwertmannite to goethite transformation are not well understood and the transformation times can range from hours (Burton et al., 2008) to months (Knorr and Blodau, 2007; Regenspurg et al., 2004; Schwertmann and Carlson, 2005) to years (Bigham et al., 1996b; Jonsson et al., 2005; Regenspurg et al., 2004). It is also important to note again that the differences we observe in crystallinity using HRTEM are not visible in the XRD pattern and therefore previous kinetics studies that relied solely on XRD would not observe the initial aging steps that we may be seeing in this study. Similar aging phenomena have been observed in the conversion of ferrihydrite to goethite (Banfield et al., 2000) and in the weathering of silicate minerals (Hochella and Banfield, 1995), where structural inheritance during phase transformation occurred. In their proposed model structure for schwertmannite, Fernandez-Martinez et al. (2010) noted the close relationship between the iron octahedral framework of schwertmannite and goethite, pointing out that the release of just one pair of iron octahedra would allow the transformation from a schwertmannite to a goethite framework. A strong relationship between goethite and schwertmannite is also apparent in the schwertmannite XRD pattern as the most intense peak of schwertmannite at 0.255 nm –where we also observed the majority of our lattice fringes– is framed by the second (111) and third (301) most intense reflections in the goethite XRD pattern (Cornell and Schwertmann, 2003). Based on this it is conceivable that the small amount of observable order in the schwertmannite XRD pattern could be due to goethite nanoparticles within the schwertmannite matrix. A previous study on synthetic schwertmannite produced at 85°C showed that schwertmannite nanoneedles were entirely composed of faceted goethite nanocrystals (Hockridge et al., 2009). Although we do not see evidence of distinctive goethite nanocrystals in the natural

schwertmannite nanoneedles, the Hockrdige et al. (2009) study demonstrates that goethite can be a part of the schwertmannite structure, despite the fact that one cannot identify individual goethite peaks in the XRD pattern.

If it is true that schwertmannite contains goethite as an important part of its structure, then why are not more lattice fringes observed that align well with the most intense (101) reflection in goethite's XRD pattern? Aging studies on a natural schwertmannite (Acero et al., 2006) show that the (101) goethite reflection appears at the same time that the reflections for the (301), (210), (400), and (111) planes of goethite begin to show individual peaks within the single broad peak at 0.255 nm in the schwertmannite XRD pattern. This implies that at the earliest stages of phase transformation, the (101) plane of goethite appears. But if we begin with the assumption that the intensity of all of the peaks in the schwertmannite XRD pattern are due to d-spacings that are closely aligned with goethite d-spacings, then it follows that the atomic arrangement that gives rise to the (101) plane of goethite may be particularly inhibited from forming. The most likely candidate for this inhibition is the presence of sulfate, which has been proposed as part of the schwertmannite structure (Bigham et al., 1994; Fernandez-Martinez et al., 2010) and which is known as a competing ion for complexation with ferric iron (Majzlan and Myneni, 2005).

3.33 The presence of sulfur and silica in schwertmannite nanoneedles

We performed an EDX analysis on individual needles from whole aggregates of schwertmannite that were *not* embedded in a resin; therefore, all chemical information comes from the schwertmannite and not from any sample preparation artifacts. Assuming that the schwertmannite needles may have a cone-like shape, the EDX data implies a

heterogeneous distribution of sulfur in the schwertmannite needles. The ratio of sulfur to iron is higher on the surface of the schwertmannite needles than in the center of the needle (Figure 3.7). Surprisingly, considering silica's concentration of 0.008 wt% in the bulk sample of schwertmannite as opposed to sulfur's 5.5 wt% concentration (Table 3.3), silica has a higher concentration than sulfur in these needles. The silica to iron ratio is also higher on the surface than in the center of the needles.

EDX analysis of the TSR schwertmannite shows that the concentration of sulfur is two orders of magnitude lower than silica in the needles (Figure 3.8). Again, this is a surprising result considering the bulk chemical information (Table 3.3) where sulfur is two orders of magnitude higher in concentration than silica. In the needles, sulfur has its highest concentrations in close proximity to the darker contrast areas with easily observable lattice fringes rather than concentrating only in the areas between the needles like silica (see sampling points 5-7, Figure 3.8A and 3.8B). In other needles on the same schwertmannite particle, sulfur concentrates in areas with visible lattice fringes, further showing evidence of sulfur's close association with the more crystalline and lower silica to iron ratio areas (Figure B.S10). This is reasonable as sulfate fits in the proposed iron octahedral tunnel structure of schwertmannite and may also complex with the surface of the schwertmannite (Bigham et al., 1994; Fernandez-Martinez et al., 2010). Sulfate is not a part of the structure of goethite however, but may sorb to the surface of iron oxides (McBride, 1994). It is possible to explain the higher ratio of sulfur to iron on the surface compared to the core of the needles as sulfate being pushed out and released to solution as the needles transform to goethite. Previous studies explained higher concentrations of sulfate in bulk digestions of samples than would be predicted by the proposed chemical

formula for schwertmannite as sulfate that is adsorbed to the surface of schwertmannite (Bigham et al., 1996a). This is also consistent with our EDX data.

Silica, unlike sulfate, is unlikely to chemically substitute into the iron octahedral structure because of the large difference in ionic radii between Si^{4+} and Fe^{3+} (0.26Å for $^{IV}Si^{4+}$ and 0.49Å for $^{IV}Fe^{3+}$) (Shannon, 1976). Under the geochemical conditions of the MR and TSR field sites the majority of silica should be in the monosilicic acid form (H_4SiO_4). As the water samples were undersaturated with respect to amorphous silica and we are at a pH of 3, which is much less than the pK_1 of silicic acid (McBride, 1994), it is most likely that the silica here was adsorbed to the surface of the schwertmannite. Although surface adsorbed silica has not been observed for schwertmannite in any previous studies, silicic acid may form complexes and polymers at the surface of Fe (oxyhydr)oxide surfaces (Doelsch et al., 2001; Doelsch et al., 2003; Eick et al., 2009; Waltham and Eick, 2002). Surface adsorption may also be increased within the nano- and mesopores created by the closely packed needles of schwertmannite because they create highly confined spaces where water activity will be reduced as compared to bulk water. This reduces the hydration of species and therefore promotes inner-sphere complexation (Wang et al., 2003).

We observed silica in multiple needles from this same TSR schwertmannite aggregate as well as in another aggregate of TSR schwertmannite that were randomly selected (supplemental Figure B.S11 and B.S12). The pattern of high silica to iron ratios in amorphous areas was also observed repeatedly (supplemental Figure B.S11). Although we could not collect chemical information on the amount of silica present in the interior of schwertmannite in these studies, the ratio of silica to iron from the bulk digestion and

from EDX data on entire aggregates of schwertmannite indicates that this high ratio of silica to iron is a surface phenomenon. It is also possible that we only observed those particles that had higher than average concentrations of silica on the surface. Determining what effect silica could have on the structure of schwertmannite is beyond the scope of the current study. Recently though a study on natural ferrihydrite that contained 2-9 wt% silica proposed that silica reduced particle size and increased structural disorder in the ferrihydrite particles (Cismasu et al., 2011). Other studies also found that silica inhibits iron polymerization and complexes with the surface of iron oxides (Pokrovski et al., 2003). Regardless of the exact role of silica in schwertmannite its presence in our samples adds to the already complex nature of understanding the surface reactivity of naturally occurring nanominerals, which would be affected by natural coatings.

3.34 The distribution of arsenic within schwertmannite needles

According to the bulk digestion of our two schwertmannite samples, the TSR sample contains approximately twice the concentration of arsenic as the MR sample. While arsenic was detectable in needles in the TSR sample (Figure 3.8C), we were not able to detect arsenic in the MR sample. The EDX results indicate that arsenic in the TSR sample was strongly associated with the darker contrast and highly crystalline areas of the schwertmannite surface (Figure 3.8C, sampling points 2-5 and 8-10, supplemental Figure B.S11) with the exception of point 13 with its lighter contrast. However, the point 13 area also contains lattice fringes and has relatively low silica to iron ratio indicating that the difference in contrast is likely due to differences in thickness and not crystallinity. The absence of arsenic in areas high in silica is also consistent with previous

work where silicate reduced the rate of adsorption, blocked adsorption sites, and displaced arsenite on goethite surfaces (Luxton et al., 2008; Waltham and Eick, 2002).

Field studies (Acero et al., 2006; Asta et al., 2010b) explained the sequestration of arsenic by schwertmannite through the exchange of the sulfate anion by the arsenate anion in the tunnels of the akaganéite-like proposed structure for schwertmannite or through surface adsorption (Fukushi et al., 2004; Regenspurg and Peiffer, 2005; Waychunas et al., 1994). Geochemical modeling predicts that the dominant arsenic species will be the arsenate anion ($H_2AsO_4^-$) in the field sites where our samples were collected (Acero et al., 2006; Asta et al., 2010b; Dove and Rimstidt, 1985). Schwertmannite has a point of zero charge of 7.2 (Jonsson et al., 2005) favoring sorption of negatively-charged ions at a low pH where the surface of schwertmannite would be positive (Acero et al., 2006). While arsenic may be sequestered by schwertmannite, it can also inhibit its formation and transformation to goethite (Regenspurg and Peiffer, 2005; Waychunas et al., 1994). Both sulfate and arsenate inhibit the formation of the Fe(III)-OH^- complex and therefore iron oxide formation (Majzlan and Myneni, 2005; Regenspurg and Peiffer, 2005). But arsenate acts as a more 'aggressive' competitor anion than sulfate with a higher surface complexation constant (Fe(III)-$H_2AsO_4^-$ is log K 29.3 and Fe(III)-SO_4^{2-} is log K 7.78 (Dzombak and Morel, 1990)) (Carlson et al., 2002; Regenspurg and Peiffer, 2005). In contrast to this observed inhibitory effect, we found the higher concentration of arsenic in the TSR sample, which appeared to be more crystalline than the MR sample with d-spacings that closely matched goethite planes. However, our natural schwertmannite contained 10 times less arsenic than Regenspurg et

al.'s (2005) arsenic-doped synthetic schwertmannite and therefore it is likely that arsenic does not have a highly inhibitory effect on goethite formation at these trace levels.

The presence of arsenic associated with goethite nanocrystals possibly forming within the highly disordered schwertmannite needle matrix has interesting implications for the fate of this trace element once the transformation to goethite has occurred. In laboratory studies the solid phase retained arsenic throughout the transformation from schwertmannite to goethite, but no specific mechanisms were proposed for this retention (Acero et al., 2006; Courtin-Nomade et al., 2005). Although the ionic radius for arsenate would, theoretically, allow it to be incorporated into the goethite structure (Cornell and Schwertmann, 2003) this has not been demonstrated prior to the study by Pedersen et al. (2006). This study found that arsenate could be very strongly bound to goethite and incorporated into the structure, preventing it from desorbing. Previous studies have also demonstrated the high affinity of goethite nanocrystals for arsenic in river systems (Plathe et al., 2010), allowing goethite nanocrystals to act as a transporter for trace elements over long distances or 'nanovectors' (Hassellov and von der Kammer, 2008). The combined effect of a strong affinity for goethite and the inhibition of crystal growth by arsenic increases the likelihood that schwertmannite derived goethite would be a source of these nanovectors for arsenic transport. Furthermore, regardless of the presence of arsenic, goethite formed from the transformation of schwertmannite forms nanocrystals (Bigham et al., 1996b; French et al., submitted). A survey on the Iberian Pyrite Belt (IPB) concluded that the majority of goethite in that system should be considered as a transformation product of schwertmannite, as goethite was most often associated with older precipitates and schwertmannite with the overlying fresh

precipitates (Espana et al., 2005). Olías et al. (2006) found that over 36 tons per year of arsenic are released to the Huelva estuary and then to the Atlantic ocean, making the IPB and therefore schwertmannite one of the major geochemical controls on the global fate and transport of arsenic.

Acknowledgements

We thank the ICTAS Nanocharacterization and Fabrication Laboratory (NCFL) at Virginia Tech, the Materials Science and Engineering Nanoscale Materials Characterization Facility (MSE-NMCF) at the University of Virginia, and the Campus Electron Optics Facility (CEOF) at Ohio State University in collaboration with FEI Company for the use of their Titan microscopes. We thank Matthew Eick for helpful comments that greatly enhanced the quality of this paper. Grants from the US Department of Energy (DE-FG02-06ER15786) and the Institute for Critical Technology and Applied Sciences at Virginia Tech provided major financial support for this project. We are also appreciative of the support from the National Science Foundation (NSF) and the Environmental Protection Agency through the Center for Environmental Implications of NanoTechnology (CEINT) funded under NSF Cooperative Agreement EF-0830093. Fellowship support for this research was provided by the National Science Foundation (NSF IGERT grant DGE-0504196). Any opinions, findings, and conclusions or recommendations expressed in this material are those of the authors and do not necessarily reflect the views of NSF, EPA, or DOE.

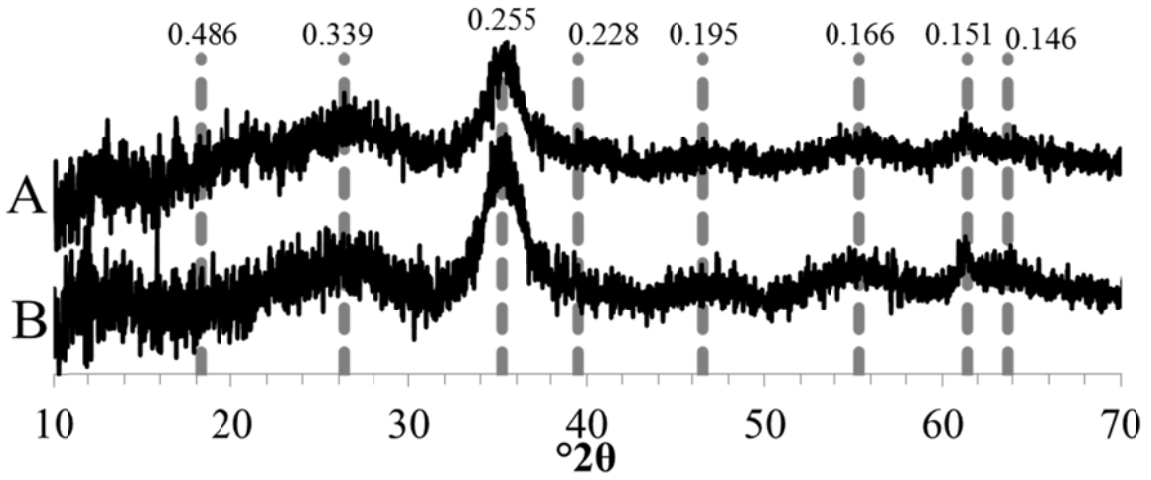

Figure 3.1. *XRD pattern for precipitates from two sites. (A) Monte Romero mine and (B) Tinto Santa Rosa mine. The grey dotted lines are the literature values for the d-spacings for schwertmannite (Cornell and Schwertmann, 2003).*

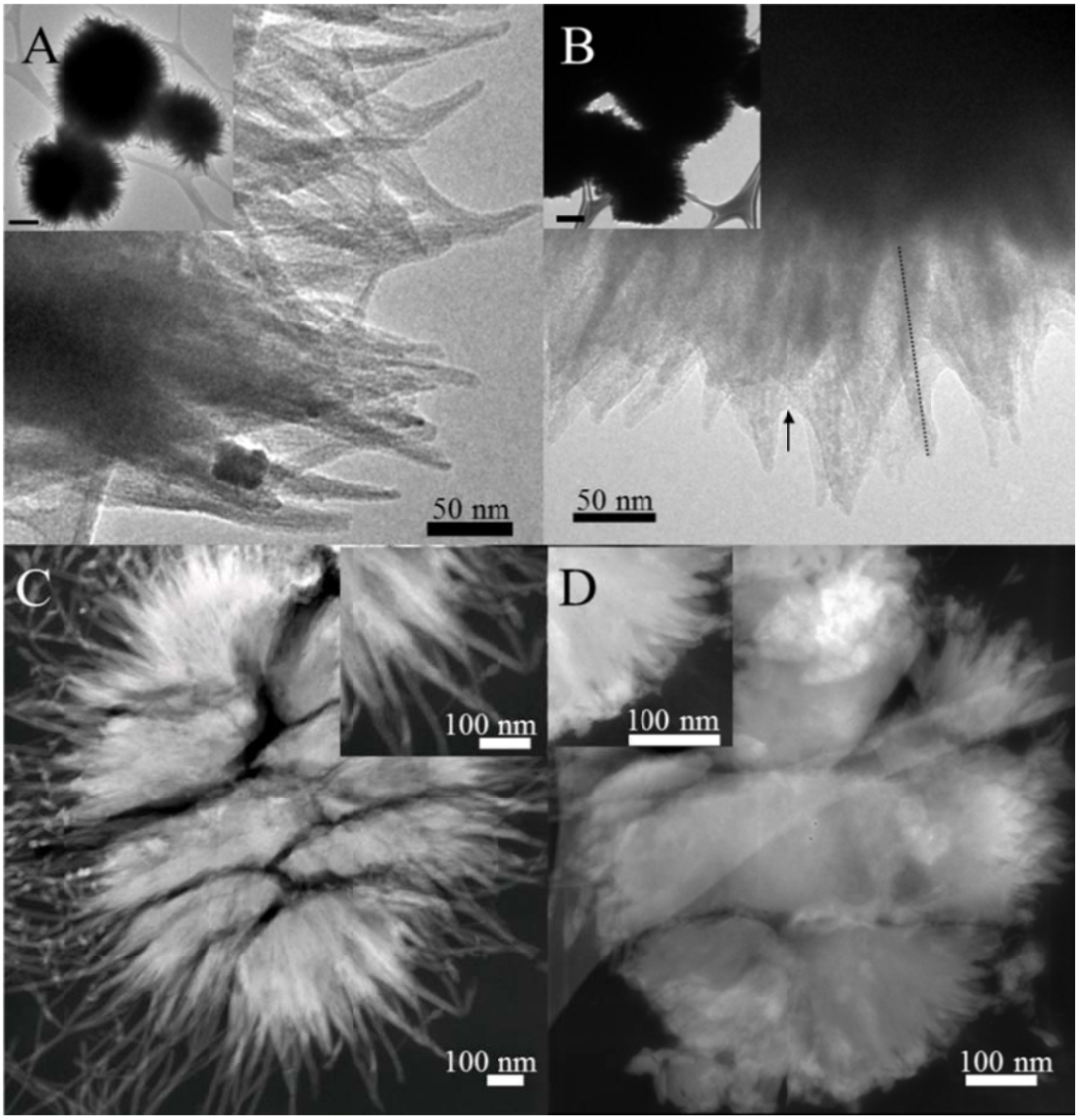

Figure 3.2. *Schwertmannite needles from a schwertmannite 'pin cushion' shown in inset. (inset scale bar = 500 nm) from the MR (A) and TSR (B) mine sites and a cross section of a schwertmannite particle embedded in resin from the MR mine (C) and TSR mine (D) taken in HAADF-STEM mode. Insets show magnifications of needles on the surface of the schwertmannite particle.*

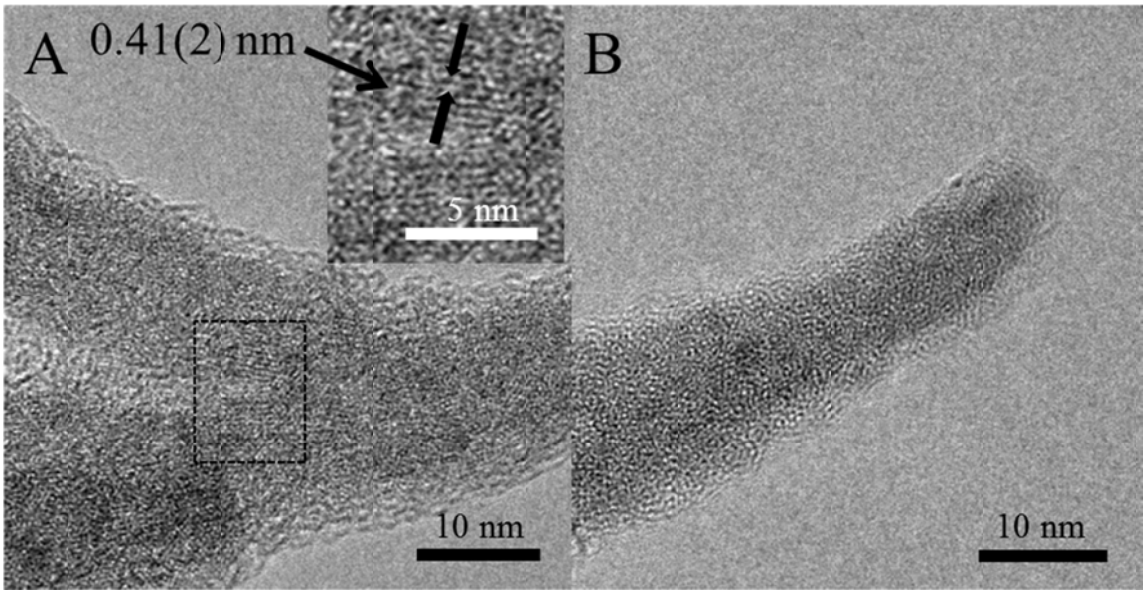

Figure 3.3. *TEM images of an individual schwertmannite needle from the MR mine on the surface of one of the schwertmannite particles in Figure 3.2A. (A) is the base of the needle and (B) shows the tip of the same needle. Inset in A shows lattice fringes enclosed by the black box.*

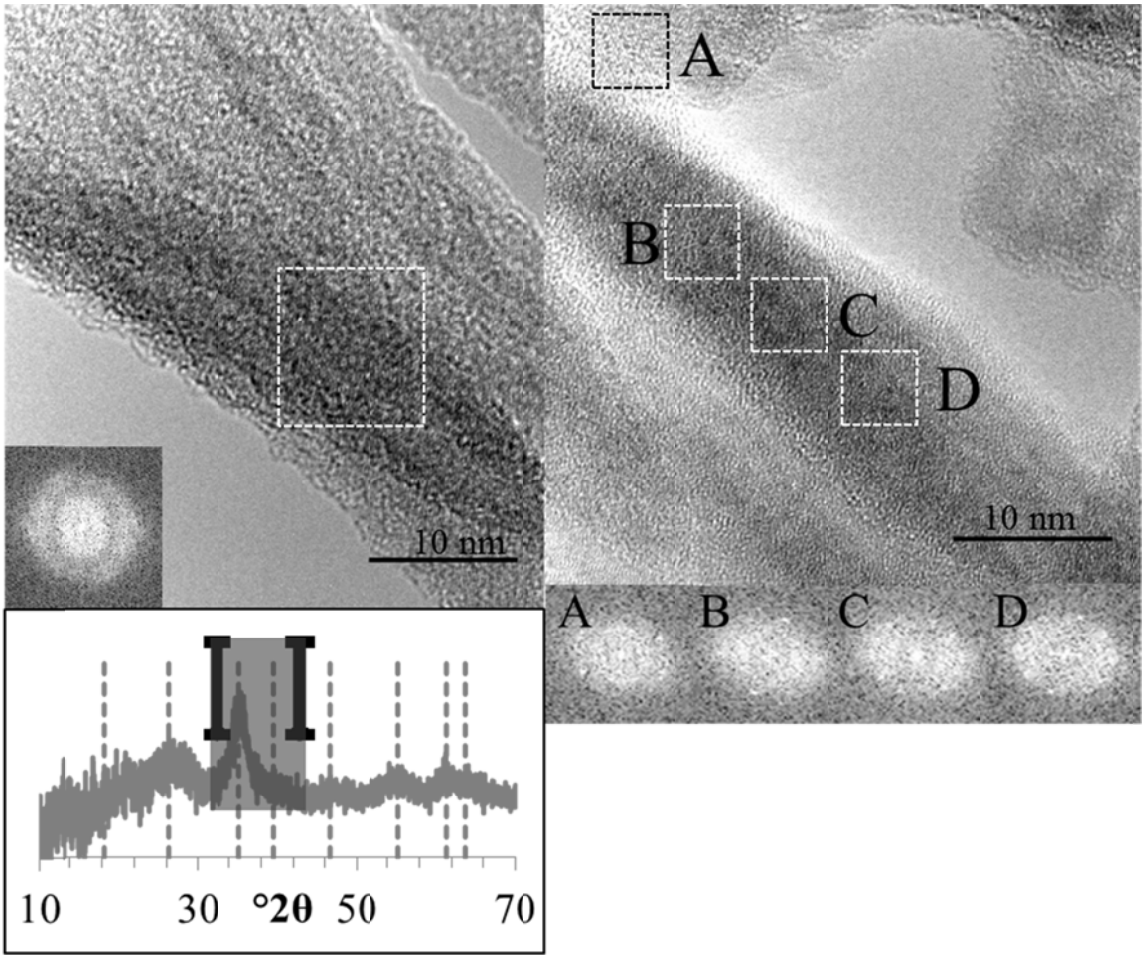

Figure 3.4. *TEM images needles on the surface of a schwertmannite particle from the MR mine. Insets show the FT of the areas enclosed white boxes. The XRD pattern of the bulk schwertmannite sample with black lines showing the d-spacings measured from the inside and edge of the outer ring on the FT pattern for the TEM image on the left. (See supplemental info. Figure B.S4 for explanation of how error bars are calculated). The dotted grey lines are the literature values for schwertmannite's d-spacings (Cornell and Schwertmann, 2003).*

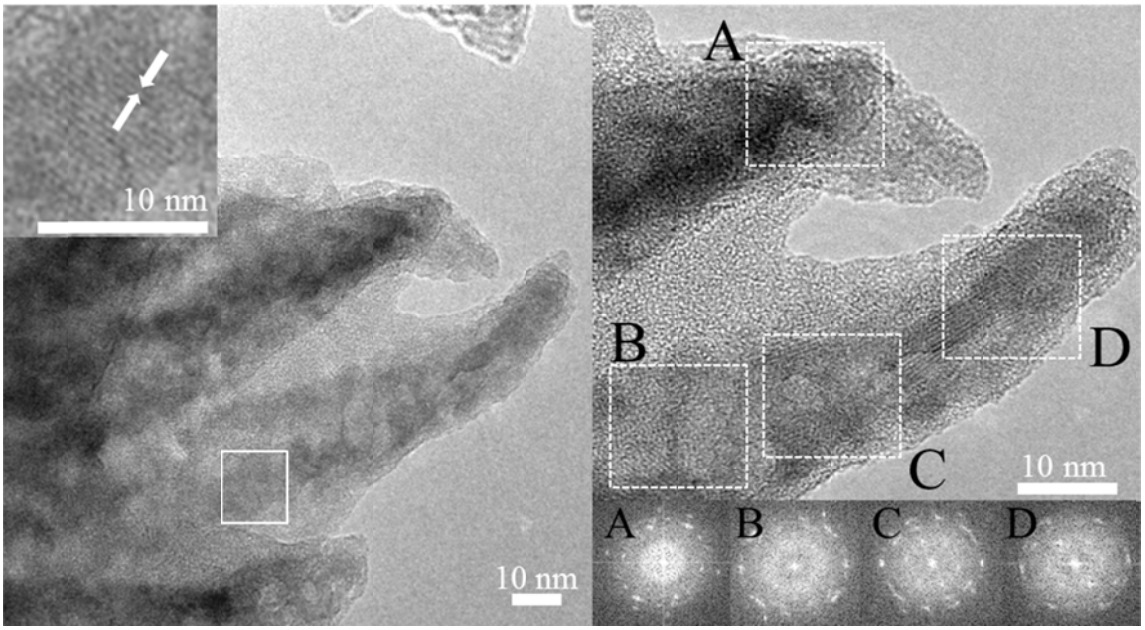

Figure 3.5. *Needles on the surface of a schwertmannite particle in Figure 3.3B from the TSR mine. Left image shows lattice fringes. Right image shows the tips of the needles on the left image. Insets show the FT of the areas enclosed by the white boxes.*

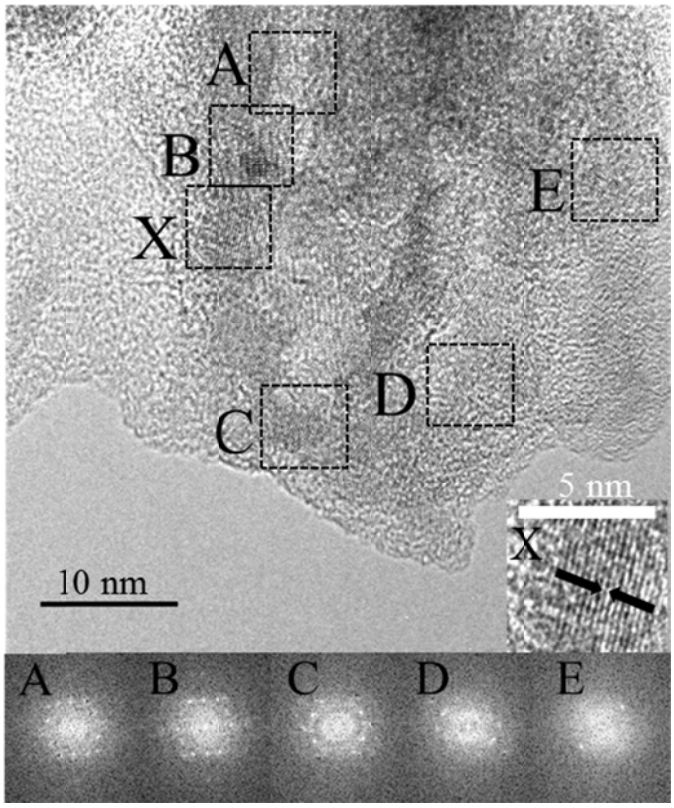

Figure 3.6. *Surface of a schwertmannite particle from the TSR mine. Insets A-E show the FT of areas enclosed by black boxes. The inset 'X' shows lattice fringes from area 'X' enclosed by the black box.*

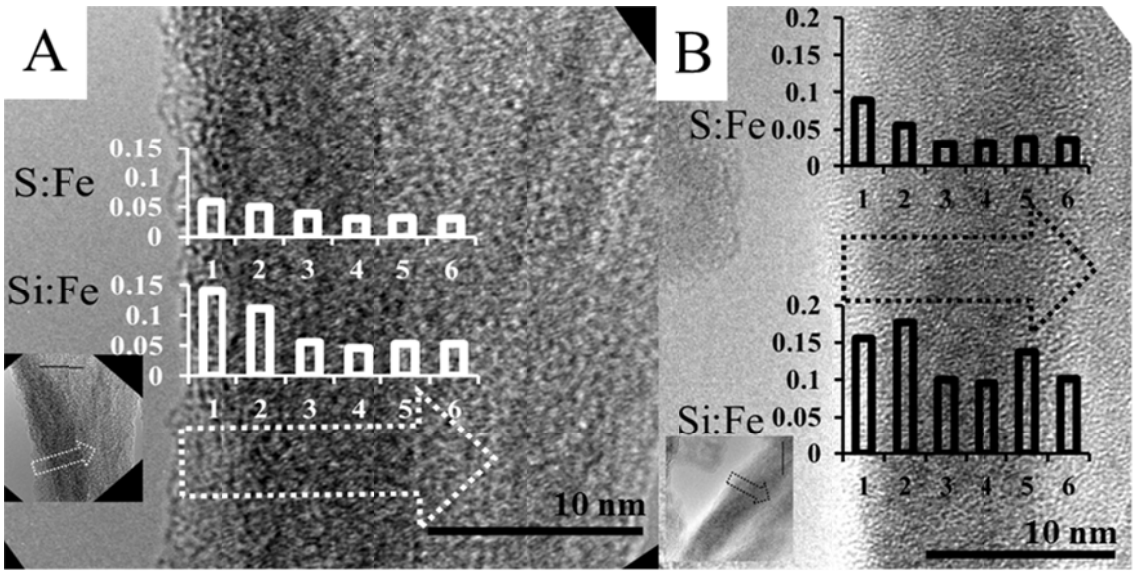

Figure 3.7. *Magnified images of MR schwertmannite needles. Insets show entire area (see also Figure 3.4). Bar graphs show the ratio of integrated K peak intensities for S:Fe and Si:Fe as you move along the arrow from the outside of the needle towards the center of the needle.*

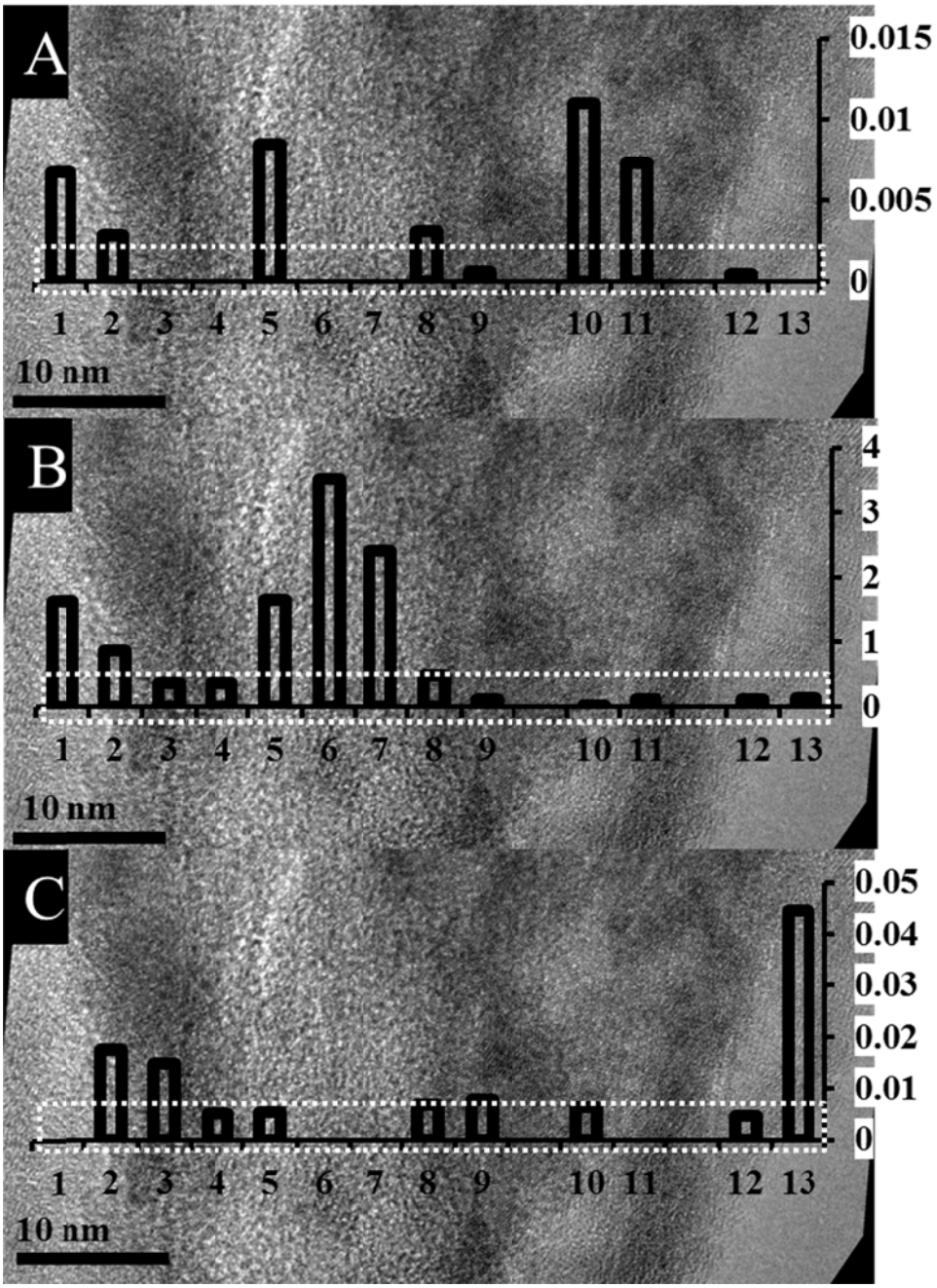

Figure 3.8. *Schwertmannite nanoneedles from the TSR sample. (For larger area see supplemental Figure B.S1). Numbers on the horizontal axis denote approximate points where EDX data was collected within the area of the white rectangle. Bar graphs show the ratio of integrated K peak intensities for S:Fe (A), Si:Fe (B), and As:Fe (C). The ratios of S:Fe and Si:Fe may be directly compared to each other, but the As:Fe ratios should not be compared to the ratios of the other elements.*

Table 3.1. *Water chemistry of AMD streams. (Metal concentration = mgL^{-1}).*

Site	pH	CE ($mS\ cm^{-1}$)	T (°C)	Eh (mV)	pE
MR	2.66	2.76	30	672.2	11.4
TSR	2.53	2.53	18.4	660	11.2

Site	Al	As	Ca	Cd	Co	Cr	Cu	Fe	K	Mg
MR	105	0.085	260	0.701	0.775	0.0043	5.9	201	3.1	264
TSR	66	0.791	162	0.079	0.954	0.011	15	568	n.d.*	124

Site	Mn	Ni	Pb	S	SO_4	Si	Ti	V	Zn
MR	18	0.826	0.139	1136	3408	38	0.007	n.d.	457
TSR	33	0.731	0.076	902	2706	33	n.d.	0.00973	62

*n.d. = no data

Table 3.2. *PHREEQC saturation index calculations with respect to goethite, ferihydrite, jarosite, and schwertmannite.*

Site	Goethite	$Fe(OH)_3$	Jarosite -K	Jarosite -H_3O	Schwertmannite (log*K* = 18(2.5))[a]	Schwertmannite (log*K* = 10.5(2.0))[b]	Schwertmannite (log*K* = 7.06(0.09))[c]
MR	4.3	-1.8	2.4	0.39	-5.2	0.84	10.0
TSR	3.7	-2.0	n.d.	-1.2	-6.1	-0.027	8.90

[a] (Bigham et al., 1996a); [b] (Yu et al., 1999); [c] (Kawano and Tomita, 2001)

Table 3.3. *Schwertmannite precipitates metal content (weight %).*

Site	Al	As	Ca	Cd	Co	Cr	Cu	Fe	K	Mg
MR	0.125(4)*	0.218(1)	0.072(8)	b.d.l.[†]	b.d.l.	b.d.l.	0.0148(4)	41.9(5)	0.007(4)	0.07(2)
TSR	0.023(5)	0.53(2)	0.010(1)	b.d.l.	b.d.l.	b.d.l.	0.0053(3)	42.0(7)	b.d.l.	b.d.l.

Site	Mn	Ni	Pb	S	Si	Ti	V	Zn
MR	0.0015(9)	b.d.l	b.d.l.	5.5(3)	0.008(3)	0.0040(7)	0.0215(3)	0.011(3)
TSR	0.0009(9)	b.d.l	b.d.l.	5.5(4)	0.05(1)	b.d.l.	0.010(3)	0.0026(8)

* (#) = e.s.d. or twice the standard deviation (95% confidence)
[†] b.d.l.= below detection limit

Table 3.4. *D-spacings measured from FT analysis of lattice fringes (Figure 3.5, right image) and their respective peak in the schwertmannite XRD pattern and matching reflections of goethite and H_3O-jarosite planes.**

Image area	Schwertmannite XRD peak (nm)	Goethite plane	H_3O-jarosite[a]
A,B	0.255/0.228	A,B: (211) (002) (111); A: (011)	A,B: (107) (205); A: (024)
C,D	0.255	C,D: (111) (400) (011) (210)	C,D: (205) (024)

*See supplemental Figure B.S4 for exact location of d-spacings measured from the lattice fringe.
[a] (Majzlan et al., 2004b)

Table 3.5. *D-spacings measured from FT analysis of lattice fringes (Figure 3.6) and their respective peak in the schwertmannite XRD pattern and matching reflections of goethite planes.**

Image area	Schwertmannite XRD peak (nm)	Goethite plane
Inset left image 0.503 nm ± 0.010	0.486	(200)
A,B,C,D	0.255	A-D: (301), (210); B-D: (011); D: (400)
A,C,D	0.339	No known plane (H_3O-Jarosite[a]: (113) (015) (202))
A,B,C	0.228	(401)

*See supplemental Figure B.S5 for exact location of d-spacings.
[a] (Majzlan et al., 2004b)

Table 3.6. *D-spacings measured from FT analysis of lattice fringes (Figure3. 7) and their respective peak in the schwertmannite XRD pattern and matching reflections of goethite and H_3O-jarosite planes.**

Image area	Schwertmannite XRD peak (nm)	Goethite plane
A,B	0.255	A: (301) (210); A,B: (111) (400) (011)
A,B,C,D,E	0.228	A-E: (401) (202); A-C: (211); C: (002)
A	0.195	(202) (311)
X: 0.238 nm ±0.006	0.255/0.228	(111)

* See supplemental Figure B.S6 for exact location of d-spacings.

References

Acero, P., Ayora, C., Torrento, C., and Nieto, J.M. (2006) The behavior of trace elements during schwertmannite precipitation and subsequent transformation into goethite and jarosite. Geochimica Et Cosmochimica Acta, 70(16), 4130-4139.

Asta, M.P., Ayora, C., Acero, P., and Cama, J. (2010a) Field rates for natural attenuation of arsenic in Tinto Santa Rosa acid mine drainage (SW Spain). Journal of Hazardous Materials, 177(1-3), 1102-1111.

Asta, M.P., Ayora, C., Roman-Ross, G., Cama, J., Acero, P., Gault, A.G., Charnock, J.M., and Bardelli, F. (2010b) Natural attenuation of arsenic in the Tinto Santa Rosa acid stream (Iberian Pyritic Belt, SW Spain): The role of iron precipitates. Chemical Geology, 271(1-2), 1-12.

Ball, J.W., and Nordstrom, D.K. (1991) User's manual for WATEQ4F with revised thermodynamic database and test cases for calculating speciation of major, trace, and redox elements in natural waters. U.S. Geological Survey. Water-Resources.

Banfield, J.F., Welch, S.A., Zhang, H.Z., Ebert, T.T., and Penn, R.L. (2000) Aggregation-based crystal growth and microstructure development in natural iron oxyhydroxide biomineralization products. Science, 289(5480), 751-754.

Bigham, J.M., Carlson, L., and Murad, E. (1994) Schwertmannite, a new iron oxyhydroxysulphate from Pyhasalmi, Finland, and other localities. Mineralogical Magazine, 58(393), 641-648.

Bigham, J.M., Schwertmann, U., and Pfab, G. (1996a) Influence of pH on mineral speciation in a bioreactor simulating acid mine drainage. Applied Geochemistry, 11(6), 845-849.

Bigham, J.M., Schwertmann, U., Traina, S.J., Winland, R.L., and Wolf, M. (1996b) Schwertmannite and the chemical modeling of iron in acid sulfate waters. Geochimica Et Cosmochimica Acta, 60(12), 2111-2121.

Bigham, J.M., and Nordstrom, D.K. (2000) Iron and aluminum hydroxysulfates from acid sulfate waters. Sulfate Minerals - Crystallography, Geochemistry and Environmental Significance, 40, p. 351-403.

Blodau, C. (2006) A review of acidity generation and consumption in acidic coal mine lakes and their watersheds. Science of the Total Environment, 369(1-3), 307-332.

Burleson, D.J., and Penn, R.L. (2006) Two-step growth of goethite from ferrihydrite. Langmuir, 22(1), 402-409.

Burton, E.D., Bush, R.T., and Sullivan, L.A. (2006) Sedimentary iron geochemistry in acidic waterways associated with coastal lowland acid sulfate soils. Geochimica Et Cosmochimica Acta, 70(22), 5455-5468.

Burton, E.D., Bush, R.T., Sullivan, L.A., and Mitchell, D.R.G. (2007) Reductive transformation of iron and sulfur in schwertmannite-rich accumulations associated with acidified coastal lowlands. Geochimica Et Cosmochimica Acta, 71(18), 4456-4473.

Burton, E.D., Bush, R.T., Sullivan, L.A., and Mitchell, D.R.G. (2008) Schwertmannite transformation to goethite via the Fe(II) pathway: Reaction rates and implications for iron-sulfide formation. Geochimica Et Cosmochimica Acta, 72(18), 4551-4564.

Caraballo, M.A., Rotting, T.S., Nieto, J.M., and Ayora, C. (2009) Sequential extraction and DXRD applicability to poorly crystalline Fe- and Al-phase characterization from an acid mine water passive remediation system. American Mineralogist, 94(7), 1029-1038.

Caraballo, M.A., Sarmiento, A.M., Sanchez-Rodas, D., Nieto, J.M., and Parviainen, A. (2011) Seasonal variations in the formation of Al and Si rich Fe-stromatolites, in the highly polluted acid mine drainage of Agua Agria Creek (Tharsis, SW Spain). Chemical Geology, 284, 97-104.

Carlson, L., Bigham, J.M., Schwertmann, U., Kyek, A., and Wagner, F. (2002) Scavenging of as from acid mine drainage by schwertmannite and ferrihydrite: A comparison with synthetic analogues. Environmental Science & Technology, 36(8), 1712-1719.

Chan, C.S., De Stasio, G., Welch, S.A., Girasole, M., Frazer, B.H., Nesterova, M.V., Fakra, S., and Banfield, J.F. (2004) Microbial polysaccharides template assembly of nanocrystal fibers. Science, 303(5664), 1656-1658.

Chernyshova, I.V., Hochella, M.F., and Madden, A.S. (2007) Size-dependent structural transformations of hematite nanoparticles. 1. Phase transition. Physical Chemistry Chemical Physics, 9(14), 1736-1750.

Cismasu, A.C., Michel, F.M., Tcaciuc, A.P., Tyliszczak, T., and Brown, G.E. (2011) Composition and structural aspects of naturally occurring ferrihydrite. Comptes Rendus Geoscience, 343(2-3), 210-218.

Cornell, R.M., and Schwertmann, U. (2003) The Iron Oxides. Wiley-VCH, Weinheim.

Courtin-Nomade, A., Grosbois, C., Bril, H., and Roussel, C. (2005) Spatial variability of arsenic in some iron-rich deposits generated by acid mine drainage. Applied Geochemistry, 20(2), 383-396.

Doelsch, E., Stone, W.E.E., Petit, S., Masion, A., Rose, J., Bottero, J.Y., and Nahon, D. (2001) Speciation and crystal chemistry of Fe(III) chloride hydrolyzed in the presence of SiO4 ligands. 2. Characterization of Si-Fe aggregates by FTIR and Si-29 solid-state NMR. Langmuir, 17(5), 1399-1405.

Doelsch, E., Masion, A., Rose, J., Stone, W.E.E., Bottero, J.Y., and Bertsch, P.M. (2003) Chemistry and structure of colloids obtained by hydrolysis of Fe(III) in the presence of SiO4 ligands. Colloids and Surfaces a-Physicochemical and Engineering Aspects, 217(1-3), 121-128.

Dove, P.M., and Rimstidt, J.D. (1985) The solubility and stability of scorodite, $FeAsO_4.2H_2O$. American Mineralogist, 70(7-8), 838-844.

Dzombak, D.A., and Morel, F.M.M. (1990) Surface Complexation Modeling - Hydrous Ferric Oxide. Wiley-Interscience, New York.

Eick, M.J., Luxton, T.P., and Welsh, H.A. (2009) EFFECT OF SILICA POLYMERIZATION ON THE OXALATE-PROMOTED DISSOLUTION OF GOETHITE. Clays and Clay Minerals, 57(5), 578-585.

Espana, J.S., Pamo, E.L., Santofimia, E., Aduvire, O., Reyes, J., and Barettino, D. (2005) Acid mine drainage in the Iberian Pyrite Belt (Odiel river watershed, Huelva, SW Spain): Geochemistry, mineralogy and environmental implications. Applied Geochemistry, 20(7), 1320-1356.

Fernandez-Martinez, A., Timon, V., Roman-Ross, G., Cuello, G.J., Daniels, J.E., and Ayora, C. (2010) The structure of schwertmannite, a nanocrystalline iron oxyhydroxysulfate. American Mineralogist, 95, 1312-1322.

Fernandez-Remolar, D., Gomez-Elvira, J., Gomez, F., Sebastian, E., Martiin, J., Manfredi, J.A., Torres, J., Kesler, C.G., and Amils, R. (2004) The Tinto River, an extreme acidic environment under control of iron, as an analog of the Terra Meridiani hematite site of Mars. Planetary and Space Science, 52(1-3), 239-248.

French, R.A., Monsegue, N., Murayama, M., and Hochella, M.F. (submitted) Temperature controlled crystal growth of the Fe(III)-oxyhydroxysulfate nanomineral schwertmannite and subsequent transformation to goethite nanorods. Journal of Crystal Growth.

Fukushi, K., Sato, T., Yanase, N., Minato, J., and Yamada, H. (2004) Arsenate sorption on schwertmannite. American Mineralogist, 89(11-12), 1728-1734.

Hassellov, M., and von der Kammer, F. (2008) Iron Oxides as Geochemical Nanovectors for Metal Transport in Soil-River Systems. Elements, 4(6), 401-406.

Hochella, M.F., and Banfield, J.F. (1995) Chemical weathering of silicates in nature: a microscopic perspective with theoretical considerations. In A.F. White, and S.L. Brantley, Eds. Chemical weathering rates of silicate minerals, 31, p. 353-406. The Mineralogical Society of America, Washington, DC.

Hochella, M.F., Moore, J.N., Golla, U., and Putnis, A. (1999) A TEM study of samples from acid mine drainage systems: Metal-mineral association with implications for transport. Geochimica Et Cosmochimica Acta, 63(19-20), 3395-3406.

Hockridge, J.G., Jones, F., Loan, M., and Richmond, W.R. (2009) An electron microscopy study of the crystal growth of schwertmannite needles through oriented aggregation of goethite nanocrystals. Journal of Crystal Growth, 311(15), 3876-3882.

Janney, D.E., Cowley, J.M., and Buseck, P.R. (2000) Structure of synthetic 2-line ferrihydrite by electron nanodiffraction. American Mineralogist, 85(9), 1180-1187.

Jonsson, J., Persson, P., Sjoberg, S., and Lovgren, L. (2005) Schwertmannite precipitated from acid mine drainage: phase transformation, sulphate release and surface properties. Applied Geochemistry, 20(1), 179-191.

Kawano, M., and Tomita, K. (2001) Geochemical modeling of bacterially induced mineralization of schwertmannite and jarosite in sulfuric acid spring water. American Mineralogist, 86(10), 1156-1165.

Kim, B., Park, C.S., Murayama, M., and Hochella, M.F. (2010) Discovery and Characterization of Silver Sulfide Nanoparticles in Final Sewage Sludge Products. Environmental Science & Technology, 44(19), 7509-7514.

Knorr, K.H., and Blodau, C. (2007) Controls on schwertmannite transformation rates and products. Applied Geochemistry, 22(9), 2006-2015.

Liu, J., Aruguete, D.A., Jinschek, J.R., Rimstidt, J.D., and Hochella, M.F. (2008) The non-oxidative dissolution of galena nanocrystals: Insights into mineral dissolution rates as a function of grain size, shape, and aggregation state. Geochimica Et Cosmochimica Acta, 72(24), 5984-5996.

Liu, J., Aruguete, D.M., Murayama, M., and Hochella, M.F. (2009) Influence of Size and Aggregation on the Reactivity of an Environmentally and Industrially Relevant Manomaterial (PbS). Environmental Science & Technology, 43(21), 8178-8183.

Loan, M., Cowley, J.M., Hart, R., and Parkinson, G.M. (2004) Evidence on the structure of synthetic schwertmannite. American Mineralogist, 89(11-12), 1735-1742.

Luxton, T.P., Eick, M.J., and Rimstidt, D.J. (2008) The role of silicate in the adsorption/desorption of arsenite on goethite. Chemical Geology, 252(3-4), 125-135.

Majzlan, J., Navrotsky, A., and Schwertmann, U. (2004) Thermodynamics of iron oxides: Part III. Enthalpies of formation and stability of ferrihydrite (similar to Fe(OH)(3)), schwertmannite (similar to FeO(OH)(3/4)(SO4)(1/8)), and epsilon-Fe2O3. Geochimica Et Cosmochimica Acta, 68(5), 1049-1059.

Majzlan, J., and Myneni, S.C.B. (2005) Speciation of iron and sulfate in acid waters: Aqueous clusters to mineral precipitates. Environmental Science & Technology, 39(1), 188-194.

Manceau, A. (2009) Evaluation of the structural model for ferrihydrite derived from real-space modelling of high-energy X-ray diffraction data. Clay Minerals, 44(1), 19-34.

Manceau, A. (2010) PDF analysis of ferrihydrite and the violation of Pauling's Principia. Clay Minerals, 45(2), 225-228.

Manceau, A. (2011) Critical evaluation of the revised akdalaite model for ferrihydrite. American Mineralogist, 96(4), 521-533.

McBride, M.B. (1994) Environmental Chemistry of Soils. Oxford University Press, New York.

Michel, F.M., Ehm, L., Antao, S.M., Lee, P.L., Chupas, P.J., Liu, G., Strongin, D.R., Schoonen, M.A.A., Phillips, B.L., and Parise, J.B. (2007) The structure of ferrihydrite, a nanocrystalline material. Science, 316(5832), 1726-1729.

Michel, F.M., Barron, V., Torrent, J., Morales, M.P., Serna, C.J., Boily, J.F., Liu, Q.S., Ambrosini, A., Cismasu, A.C., and Brown, G.E. (2010) Ordered ferrimagnetic form of ferrihydrite reveals links among structure, composition, and magnetism. Proceedings of the National Academy of Sciences of the United States of America, 107(7), 2787-2792.

Moreau, J.W., Webb, R.I., and Banfield, J.F. (2004) Ultrastructure, aggregation-state, and crystal growth of biogenic nanocrystalline sphalerite and wurtzite. American Mineralogist, 89(7), 950-960.

Navrotsky, A. (2004) Energetic clues to pathways to biomineralization: Precursors, clusters, and nanoparticles. Proceedings of the National Academy of Sciences of the United States of America, 101(33), 12096-12101.

Olias, M., Canovas, C.R., Nieto, J.M., and Sarmiento, A.M. (2006) Evaluation of the dissolved contaminant load transported by the Tinto and Odiel rivers (South West Spain). Applied Geochemistry, 21(10), 1733-1749.

Parkhurst, D.L. (1995) User's guide to PHREEQC: a computer program for speciation, reaction path, advective-transport, and inverse geochemical calculations. US Geological Survey. Water Resources.

Pedersen, H.D., Postma, D., and Jakobsen, R. (2006) Release of arsenic associated with the reduction and transformation of iron oxides. Geochimica Et Cosmochimica Acta, 70(16), 4116-4129.

Peine, A., Tritschler, A., Kusel, K., and Peiffer, S. (2000) Electron flow in an iron-rich acidic sediment - evidence for an acidity-driven iron cycle. Limnology and Oceanography, 45(5), 1077-1087.

Penn, R.L., Tanaka, K., and Erbs, J. (2007) Size dependent kinetics of oriented aggregation. Journal of Crystal Growth, 309(1), 97-102.

Perez-Lopez, R., Asta, M.P., Roman-Ross, G., Nieto, J.M., Ayora, C., and Tucoulou, R. (2011) Synchrotron-based X-ray study of iron oxide transformations in terraces from the Tinto-Odiel river system: Influence on arsenic mobility. Chemical Geology, 280(3-4), 336-343.

Perez-Lopez, R., and Caraballo, M.A. (unpublished) Deriving a solubility constant for schwertmannite from samples collected in the Iberian Pyrite Belt, SW Spain.

Pinedo-Vara, I. (1963) Piritas de Huelva. Su historia, minería y aprovechamineto. Summa, Madrid, Spain.

Plathe, K.L., von der Kammer, F., Hassellov, M., Moore, J., Murayama, M., Hofmann, T., and Hochella, M.F. (2010) Using FlFFF and aTEM to determine trace metal-nanoparticle associations in riverbed sediment. Environmental Chemistry, 7(1), 82-93.

Pokrovski, G.S., Schott, J., Garges, F., and Hazemann, J.L. (2003) Iron (III)-silica interactions in aqueous solution: Insights from X-ray absorption fine structure spectroscopy. Geochimica Et Cosmochimica Acta, 67(19), 3559-3573.

Raiswell, R., Benning, L.G., Davidson, L., Tranter, M., and Tulaczyk, S. (2009) Schwertmannite in wet, acid, and oxic microenvironments beneath polar and polythermal glaciers. Geology, 37(5), 431-434.

Raiswell, R. (2011) Iron transport from the open continents to the open ocean: The aging-rejuvenation cycle. Elements, 7, p. 101-106. Mineralogical Society of America, USA.

Regenspurg, S., Brand, A., and Peiffer, S. (2004) Formation and stability of schwertmannite in acidic mining lakes. Geochimica Et Cosmochimica Acta, 68(6), 1185-1197.

Regenspurg, S., and Peiffer, S. (2005) Arsenate and chromate incorporation in schwertmannite. Applied Geochemistry, 20(6), 1226-1239.

Saez, R., Pascual, E., Toscano, M., and Almodovar, G.R. (1999) The Iberian type of volcano-sedimentary massive sulphide deposits. Mineralium Deposita, 34(5-6), 549-570.

Sarmiento, A.M., Oliveira, V., Gomez-Ariza, J.L., Nieto, J.M., and Sanchez-Rodas, D. (2007) Diel cycles of arsenic speciation due to photooxidation in acid mine drainage from the Iberian Pyrite Belt (Sw Spain). Chemosphere, 66(4), 677-683.

Schwertmann, U., and Carlson, L. (2005) The pH-dependent transformation of schwertmannite to goethite at 25 degrees C. Clay Minerals, 40(1), 63-66.

Shannon, R.D. (1976) Revised effective ionic-radii and systematic studies of interatomic distances in halides and chalcogenides. Acta Crystallographica Section A, 32(SEP1), 751-767.

Tyler, G., Carrasco, R., Nieto, J.M., Perez, R., Ruiz, M.J., and Sarmineto, A.M. (2004) Optimization of major and trace element determination on acid mine drainage samples by ultrasonic nebulizer-ICP-OES (USN-ICP-OES). Pittcon Conference, p. 9000/1000, Chicago, USA.

Waltham, C.A., and Eick, M.J. (2002) Kinetics of arsenic adsorption on goethite in the presence of sorbed silicic acid. Soil Science Society of America Journal, 66(3), 818-825.

Wang, Y., Bryan, C., Xu, H., and Gao, H. (2003) Nanogeochemistry: Geochemical reactions and mass transfers in nanopores. Geology, 31, 387-390.

Waychunas, G.A., Xu, N., Fuller, C.C., Davis, J.A., and Bigham, J.M. (1994) XAS STUDY OF ASO43- AND SEO42- SUBSTITUTED SCHWERTMANNITES. 8th International Conference on X-Ray Absorption Fine Structure (XAFS VIII), p. 481-483, Berlin, Germany.

Yu, J.Y., Heo, B., Choi, I.K., Cho, J.P., and Chang, H.W. (1999) Apparent solubilities of schwertmannite and ferrihydrite in natural stream waters polluted by mine drainage. Geochimica Et Cosmochimica Acta, 63(19-20), 3407-3416.

Appendix A: Supplemental information for Chapter 2

Temperature controlled crystal growth of the Fe(III)-oxyhydroxysulfate nanomineral schwertmannite and subsequent transformation to goethite nanorods

Rebecca A. French[1,2]*, Niven Monsegue[3,4], Mitsuhiro Murayama[3,4], Michael F. Hochella Jr.[1,2]

[1]ICTAS Environmental Nanoscience and Technology Laboratory, Virginia Tech, Blacksburg, VA 24061, U.S.A.
[2]Department of Geosciences, Virginia Tech, Blacksburg, VA 24061, U.S.A.
[3]ICTAS Nanoscale Characterization and Fabrication Laboratory, Virginia Tech, Blacksburg, VA 24061, U.S.A.
[4]Department of Materials Science, Virginia Tech, Blacksburg, VA 24061, U.S.A.
*Corresponding author e-mail address: rafrench@vt.edu

To be submitted to Journal of Crystal Growth

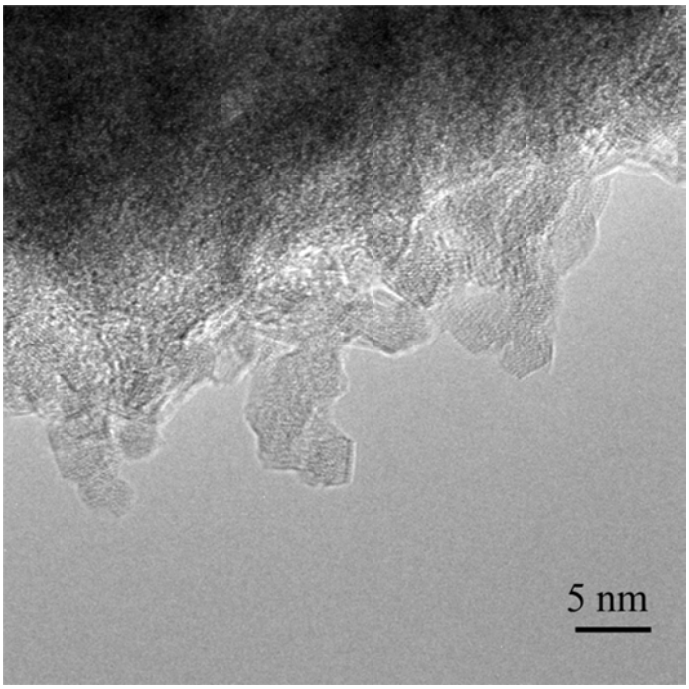

Figure A.S1. *Needles, on the surface of a schwertmannite sphere produced at room temperature with 24 hrs of reaction time, after ~7 minutes of exposure to the electron beam on an FEI Titan operating at 300 kV while focusing and alignment were occurring. The distinct faceting and increase in crystallinity, as seen from the lattice fringes, was not observed on these needles before the prolonged exposure to the beam and nowhere else where images were taken for this study. We did not observe changes to needles that were used for analysis over the course of the time that we collected images, making us confident that changes to the schwertmannite morphology and crystallinity only occur after prolonged exposure to the beam and not under the time (<1 minute) that we needed to collect our images used for analysis.*

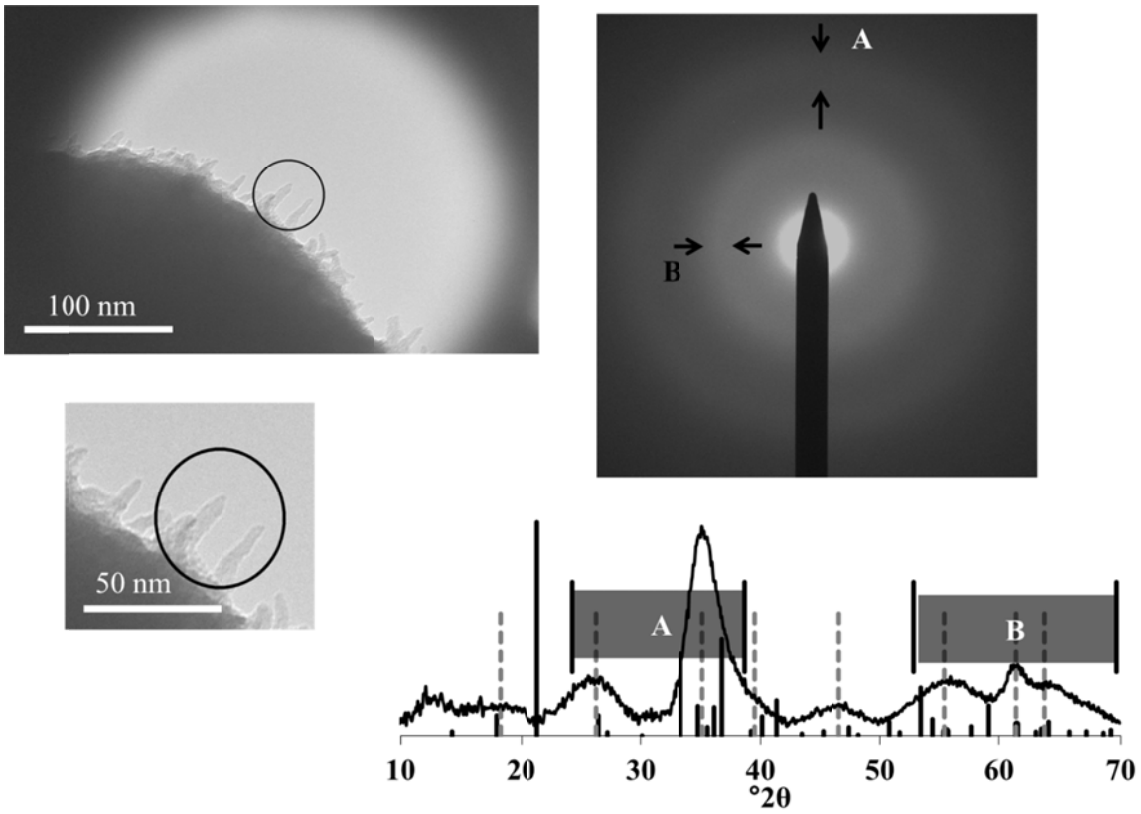

Figure A.S2. *Schwertmannite produced at room temperature with 24 hrs of reaction time (upper and lower left images). Selected area electron diffraction patterns (top right) of the circled needles shows two diffuse rings covering d-spacings over the range of 53° to 70° (2θ) and 24° to 39° (2θ) as pictured by the grey boxes overlying the XRD pattern for the schwertmannite sample. Black lines on the XRD pattern are from a goethite standard and grey dotted lines are the schwertmannite literature values (Cornell and Schwertmann, 2003).*

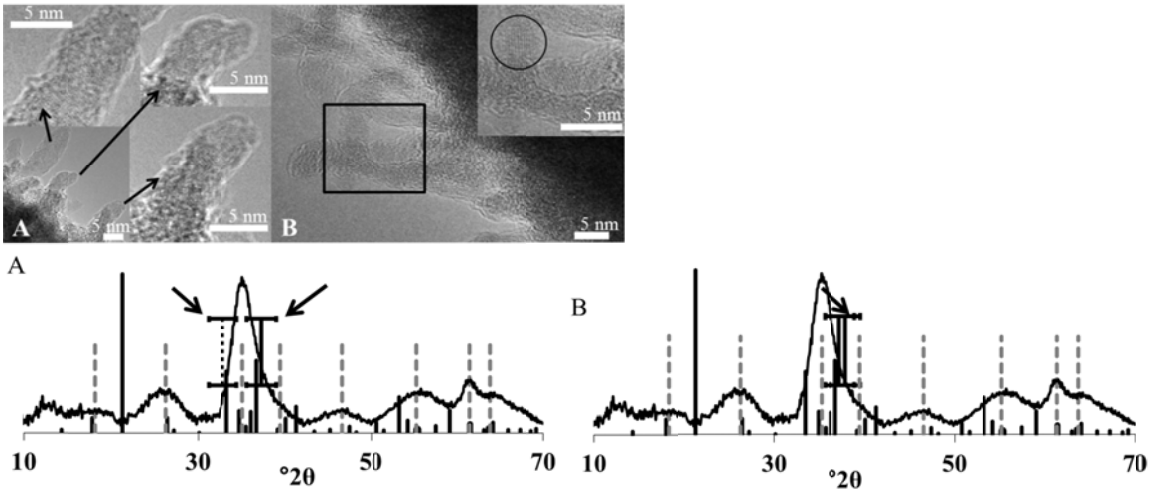

Figure A.S3. *Schwertmannite produced at room temperature. The d-spacing measured from lattice fringes in image (A) corresponds to the solid and dotted black lines (see arrows) on the x-ray diffraction pattern (A). The black solid line corresponds to d-spacings measured from the lattice fringes in image (A) upper right and the dotted line corresponds to the lattice fringes from image (A) lower right. In image (B) the lattice fringes seen in the inset have a d-spacing located at the solid line (see arrow) on the XRD pattern (B). The black lines on the horizontal axis are the goethite standard d-spacings and the grey dotted lines are the schwertmannite literature values (Cornell and Schwertmann, 2003).*

The error bars on the d-spcaings on the XRD patterns are calculated based on the pixel size of the Fourier Transform (FT) of the HRTEM images. We measure d-spacings by converting the number of pixels from an FT image to the equivalent distance in nanometers, therefore, the error in our measurements is the °2θ equivalent of plus or minus 1 pixel length of the measured d-spacing. For example, if we measured the distance between the center of an FT image and a spot to be 35 pixels and 1 pixel = 0.18 nm^{-1}, then the d-spacing (d) would be

$$d = \frac{1}{35 \times 0.18} \qquad (1)$$

and d-spacing measured if the actual length was plus one pixel would be

$$d = \frac{1}{36 \times 0.18} \qquad (2)$$

and similarly for minus one pixel the d-spacing would be

$$d = \frac{1}{34 \times 0.18} \qquad (3)$$

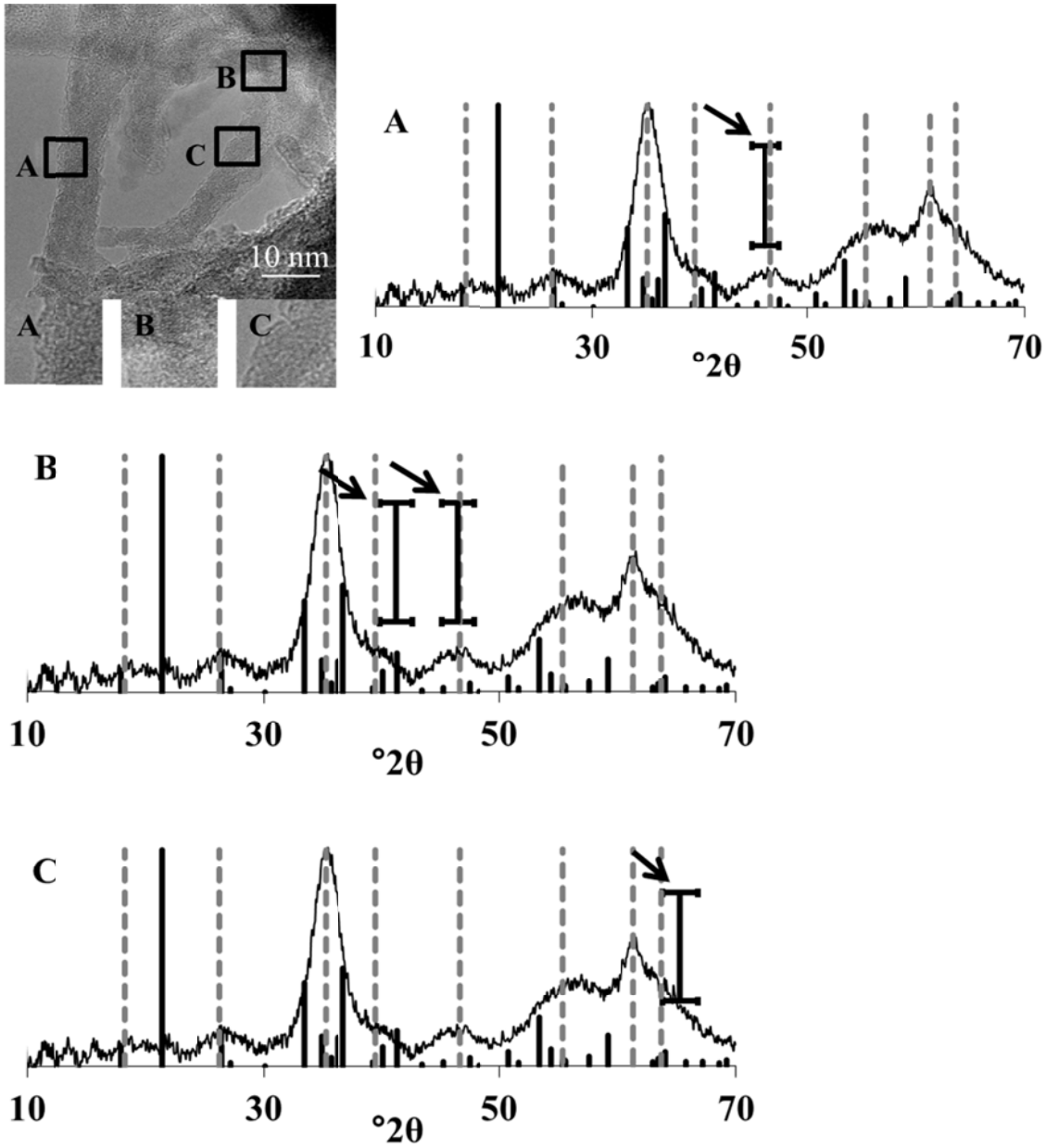

Figure A.S4. *Fourier Transform (FT) analysis of areas A, B, C in image (upper left) of schwertmannite needles formed in schwertmannite synthesis run at 75°C for 1 hr gave d-spacings shown by solid lines with error bars (see arrows). The black lines on the horizontal axis are the goethite standard d-spacings and the grey dotted lines are the schwertmannite literature values (Cornell and Schwertmann, 2003). (See Figure A. S3 for explanation of error bars).*

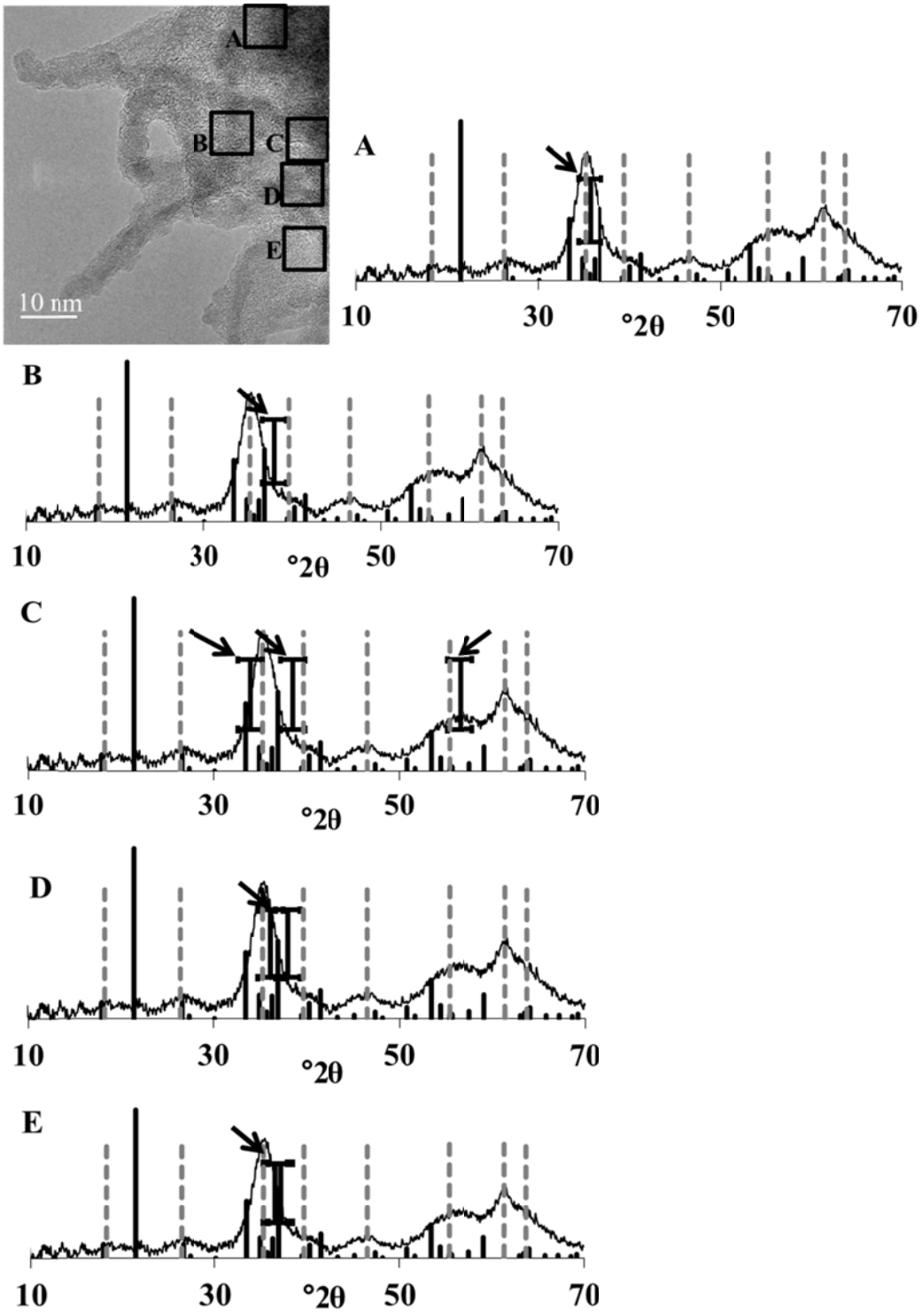

Figure A.S5. *Fourier Transform (FT) analysis of areas A, B, C, D, and E in image of schwertmannite needles formed in schwertmannite synthesis run at 75°C for 1 hr gave d-spacings shown by solid lines with error bars (see arrows). The black lines on the horizontal axis are the goethite standard d-spacings and the grey dotted lines are the schwertmannite literature values (Cornell and Schwertmann, 2003). (See Figure A.S3 for explanation of error bars).*

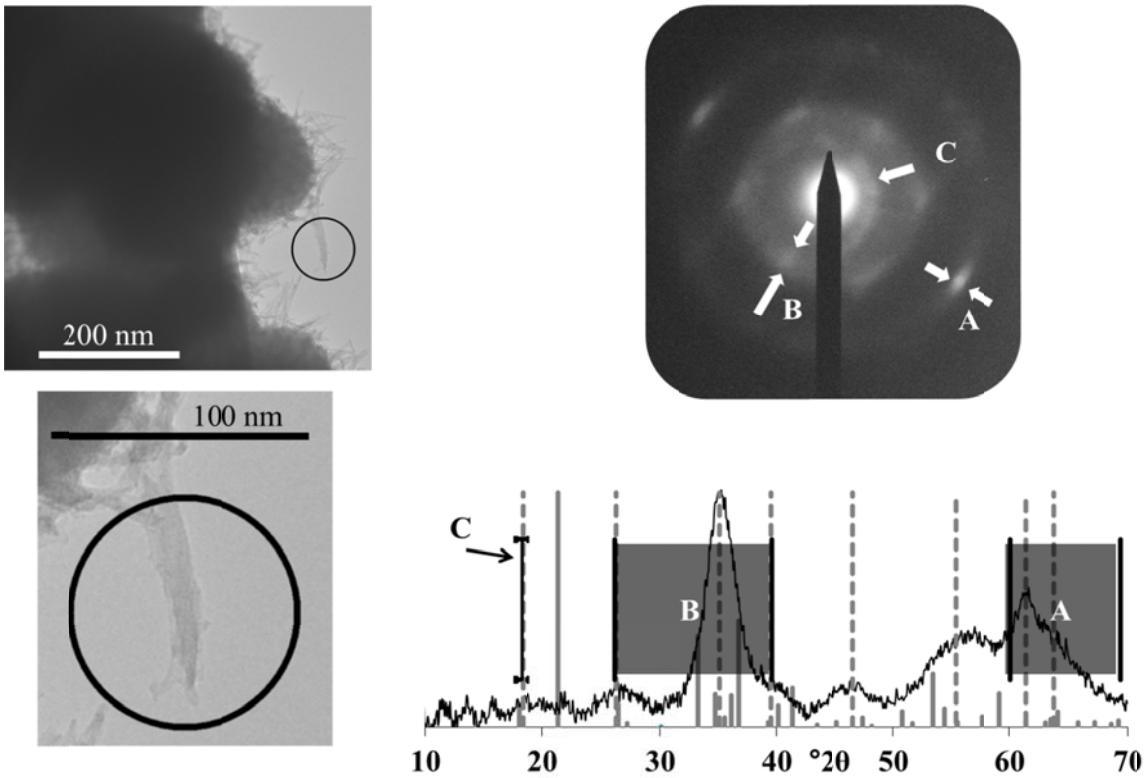

Figure A.S6. *Schwertmannite produced at 75°C after 1 hr of reaction time (upper and lower left images). Selected area electron diffraction patterns (top right) of the circled needle shows three diffuse rings with spots covering d-spacings over the range of 60° to 70° (2θ) and 26° to 40° (2θ) as pictured by the grey boxes overlying the XRD pattern for the schwertmannite sample. The outer edge of the partial ring (C) had a d-spacing at ~18° 2θ. Black lines on the XRD pattern are from a goethite standard and grey dotted lines are the schwertmannite literature values (Cornell and Schwertmann, 2003).*

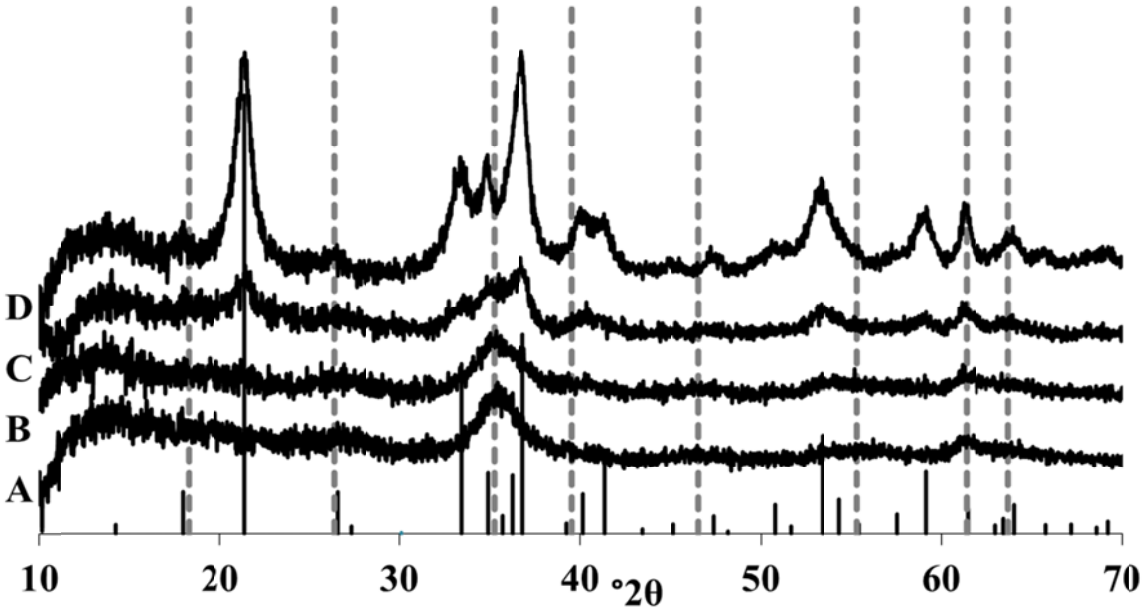

Figure A.S7. *Replicate synthesis of the transformation from schertmannite to goethite at 75°C for 24 hrs. XRD patterns were collected on precipitate extracted from the synthesis at 1 hr (A), 3 hrs (B), 6 hrs (C), and 24 hrs (D). Black lines on the XRD pattern are from a goethite standard and grey dotted lines are the schwertmannite literature values (Cornell and Schwertmann, 2003). XRD analysis was performed on a PANalytical X-pert PRO diffractometer with a Cu K-alpha (45kV-40mA) radiation. Analysis was performed from 10.004° 2θ to 79.976° 2θ with step size 0.017°.*

References

Cornell, R.M., and Schwertmann, U. (2003) The Iron Oxides. Wiley-VCH, Weinheim.

Appendix B: Supplemental information for Chapter 3

Identifying the polyphasic structure and morphology of the nanomineral schwertmannite using analytical high resolution transmission electron microscopy

Rebecca A. French[1,2*], Manuel A. Caraballo[3], Bojeong Kim [1,2], J.D. Rimstidt[2], Mitsuhiro Murayama[4,5], Michael F. Hochella Jr.[1,2]

[1]ICTAS Environmental Nanoscience and Technology Laboratory, Virginia Tech, Blacksburg, VA 24061, U.S.A.
[2]Department of Geosciences, Virginia Tech, Blacksburg, VA 24061, U.S.A.
[3]Geology Department, University of Huelva, Campus "El Carmen", E-21071 Huelva, Spain
[4]ICTAS Nanoscale Characterization and Fabrication Laboratory, Virginia Tech, Blacksburg, VA 24061, U.S.A.
[5]Department of Materials Science, Virginia Tech, Blacksburg, VA 24061, U.S.A.
*Corresponding author. E-mail address: rafrench@vt.edu

To be submitted to American Mineralogist

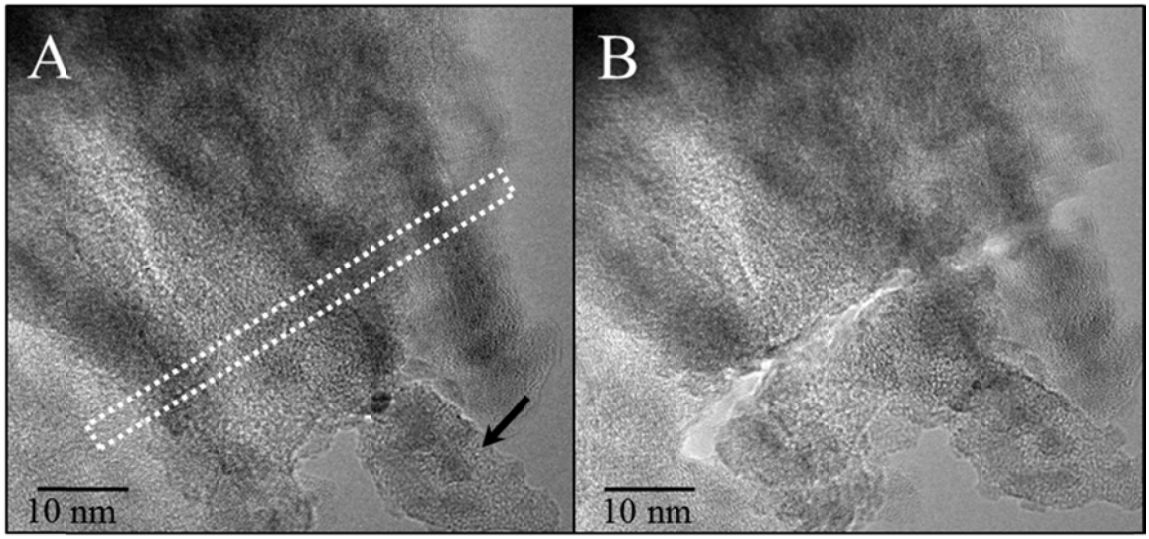

Figure B.S1. *(A) TEM image of needles on the surface of a schwertmannite particle from the TSR site. The white dotted rectangle refers to the approximate area over which EDX analysis was performed across those needles. The bumpy areas at the ends of the needle (see arrow) appear after EDX analysis and are due to beam damage. This damage was caused by EDX analysis that was performed prior to the EDX analysis along the white arrow. (B) Shows a post-EDX analysis TEM image where you can see the beam damage after analysis. Destroying the sample was necessary to obtain sufficient signal to observe trace metal content of the schwertmannite needles.*

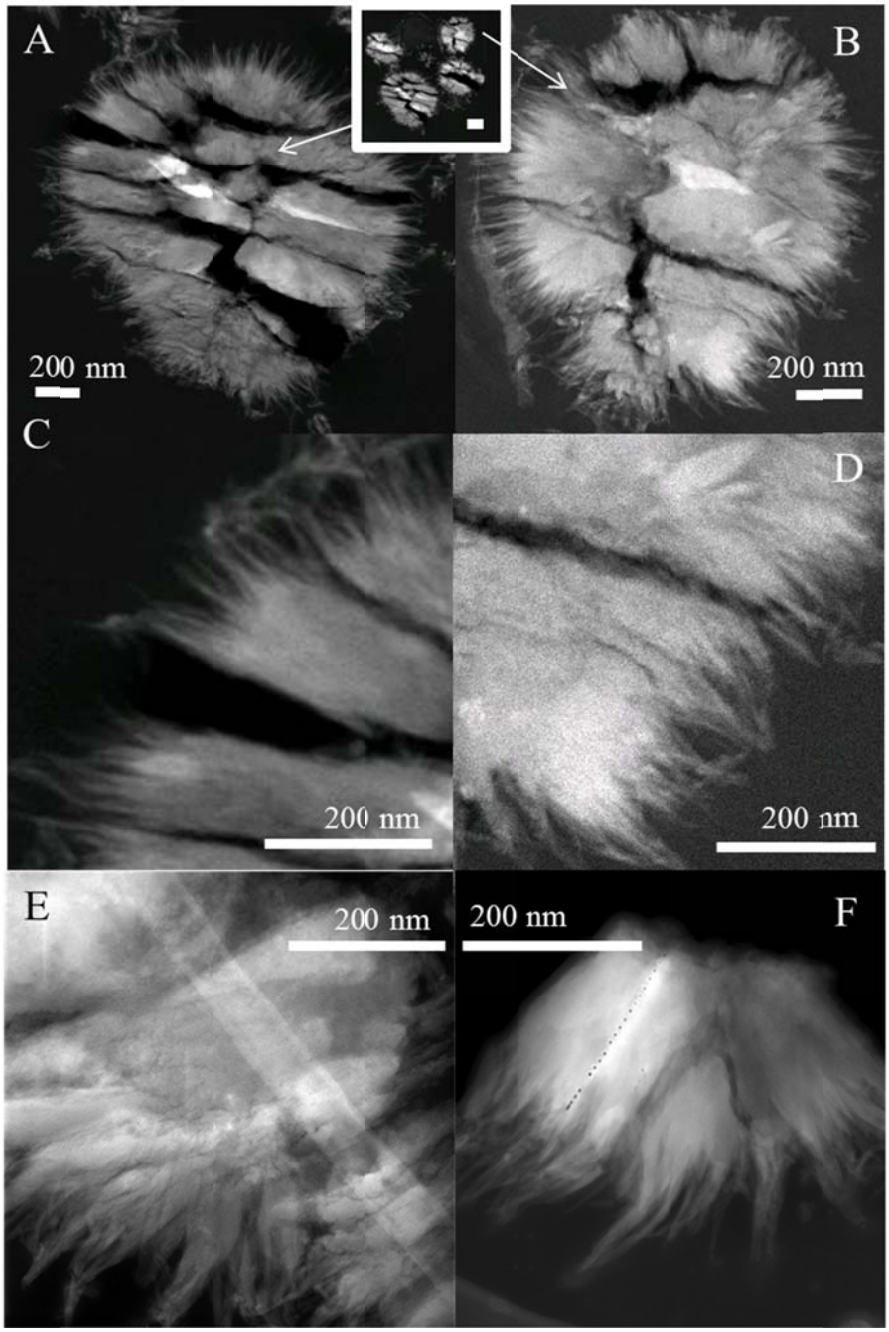

Figure B.S2. *(A) and (B) TEM images taken in DF mode of ultramicrotomed thin sections of schwertmannite from the MR site ((A), (B), and magnified areas of those particles: (C), and (D)) and the TSR site ((E) and (F)). The cracks across (A) and (B) were incurred during the cutting process and were characteristic of all schwertmannite particles that were thin sections. No evidence for these types of cracks was ever seen when imaging the schwertmannite particles as whole aggregates. (D) Shows only a portion of a schwertmannite particle that was broken during the cutting process. The line of dots that are visible on the left side of the section are holes created when collecting EDX data of the sample. The scale bar for the inset between (A) and (B) is 500 nm.*

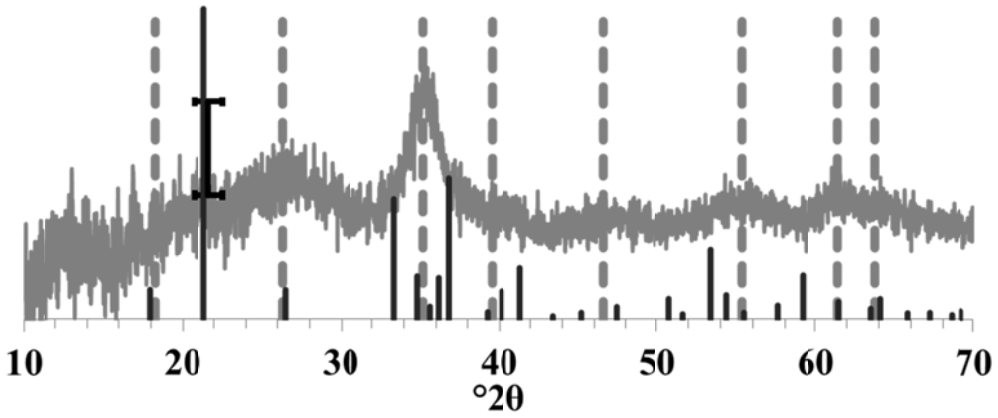

Figure B.S3. *Needle from the TSR schwertmannite (Figure 3.4 main text). XRD pattern shows the location of the d-spacing measured from the lattice fringe in image (Figure 3.4A). The d-spacing measured from lattice fringes in image (A) corresponds to the solid black lines on the x-ray diffraction pattern. The error bars were calculated as the mean and standard deviation of measurements of the lattice fringes. The black lines on the horizontal axis are the goethite standard d-spacings and the grey dotted lines are the schwertmannite literature values (Cornell and Schwertmann, 2003).*

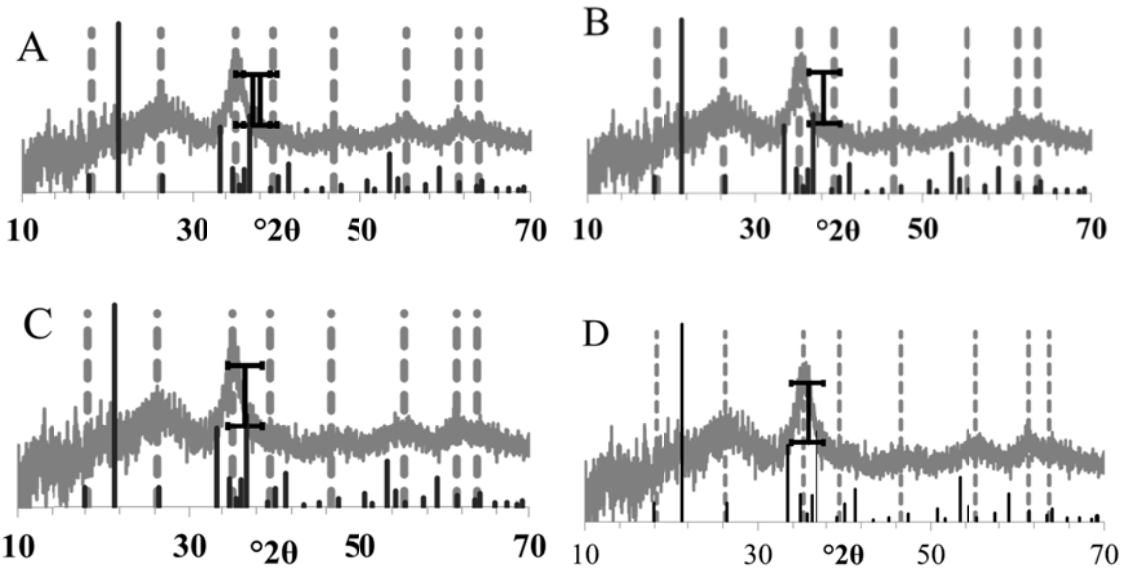

Figure B.S4. *Location of d-spacings measured using Fourier Transform (FT) analysis of HRTEM image shown in Figure 3.5, right image (main text). The FT d-spacings correspond to the solid black lines on the x-ray diffraction pattern with error bars. The error bars were calculated based on the method described below. The black lines on the horizontal axis are the goethite standard d-spacings and the grey dotted lines are the schwertmannite literature values (Cornell and Schwertmann, 2003).*

The error bars on the d-spacings on the XRD patterns are calculated based on the pixel size of the FT spectra of the HRTEM images. We measure d-spacings by converting the number of pixels from an FT image to the equivalent distance in nanometers, therefore, the error in our measurements is the °2θ equivalent of plus or minus 1 pixel length of the measured d-spacing. For example, if we measured the distance between the center of an FT image and a spot to be 35 pixels and 1 pixel = 0.18 nm^{-1}, then the d-spacing (d) would be

$$d = \frac{1}{35 \times 0.18} \quad (1)$$

and d-spacing measured if the actual length was plus one pixel would be

$$d = \frac{1}{36 \times 0.18} \quad (2)$$

and similarly for minus one pixel the d-spacing would be

$$d = \frac{1}{34 \times 0.18} \quad (3)$$

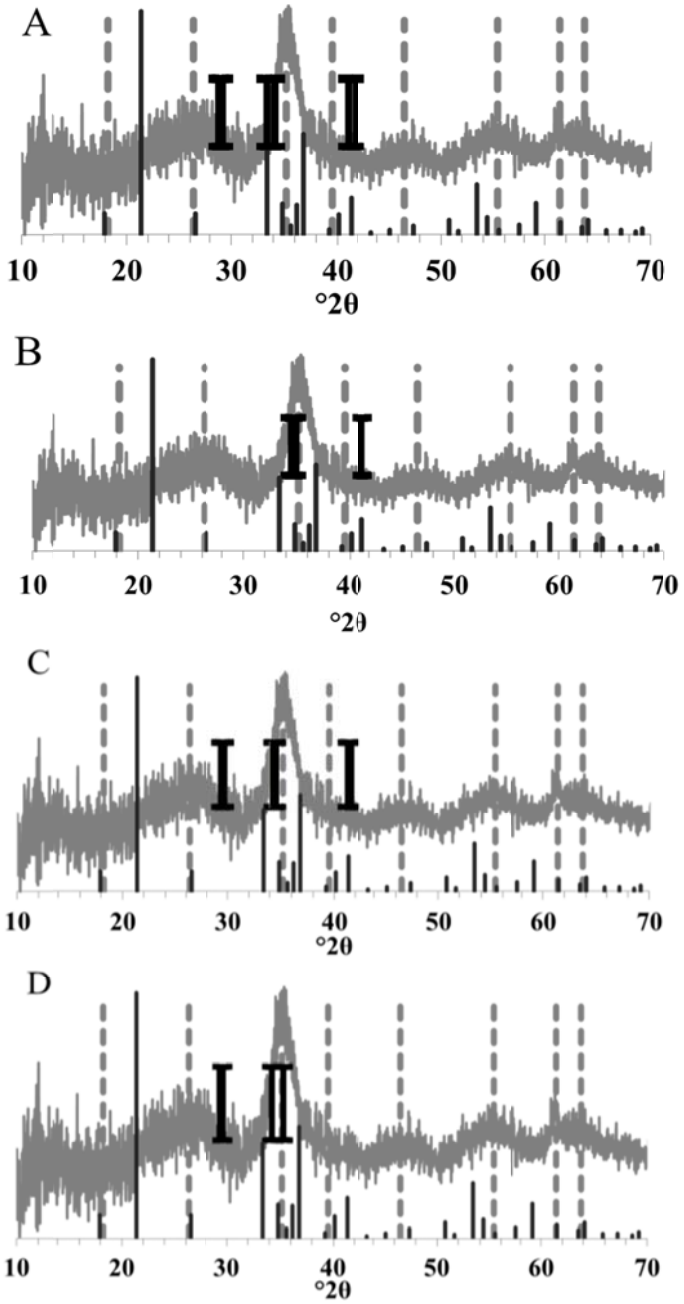

Figure B.S5. *Location of d-spacings measured using Fourier Transform (FT) analysis of HRTEM image shown in Figure 3.6, right image (main text). The FT d-spacings correspond to the solid black lines on the x-ray diffraction pattern with error bars. The error bars were calculated based on the method described below. The black lines on the horizontal axis are the goethite standard d-spacings and the grey dotted lines are the schwertmannite literature values (Cornell and Schwertmann, 2003).*

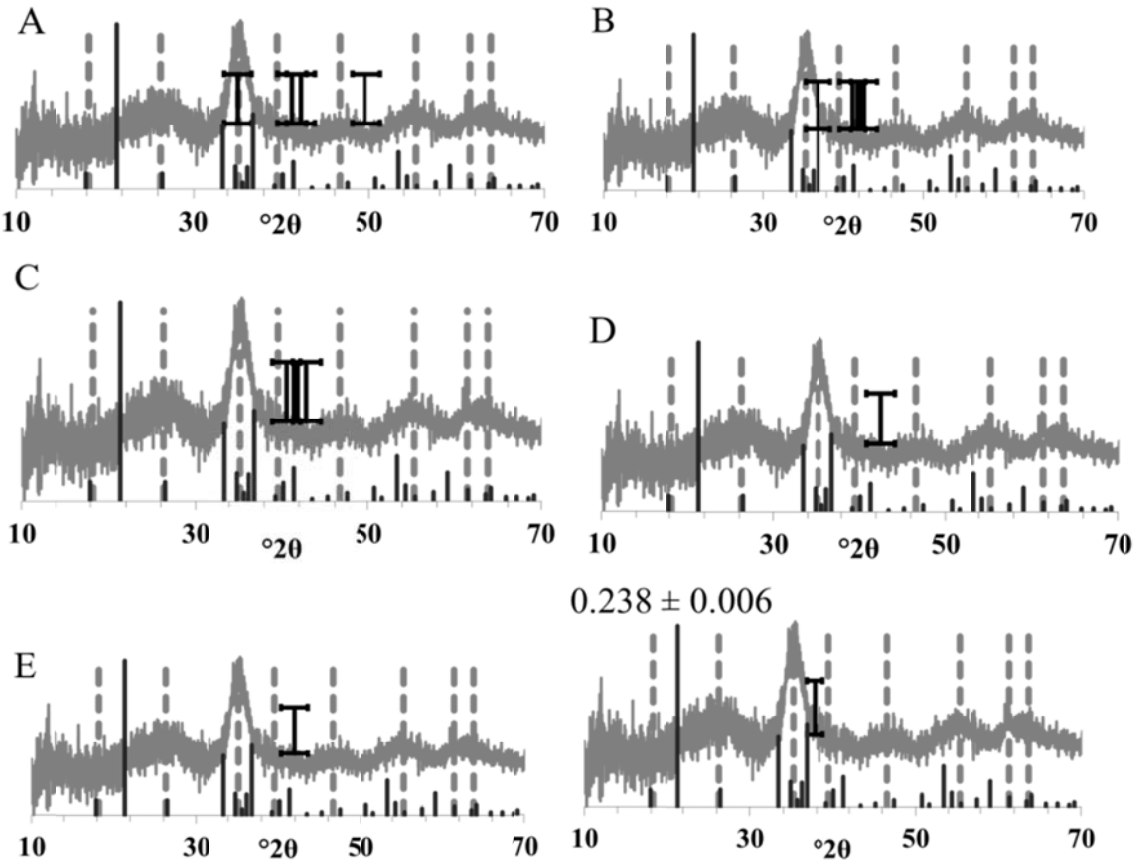

Figure B.S6. *Location of d-spacings measured using Fourier Transform (FT) analysis of HRTEM image shown in Figure 3.7. The FT d-spacings correspond to the solid black lines on the x-ray diffraction pattern with error bars. The error bars were calculated based on the method described in Figure B.S4. The black lines on the horizontal axis are the goethite standard d-spacings and the grey dotted lines are the schwertmannite literature values (Cornell and Schwertmann, 2003).*

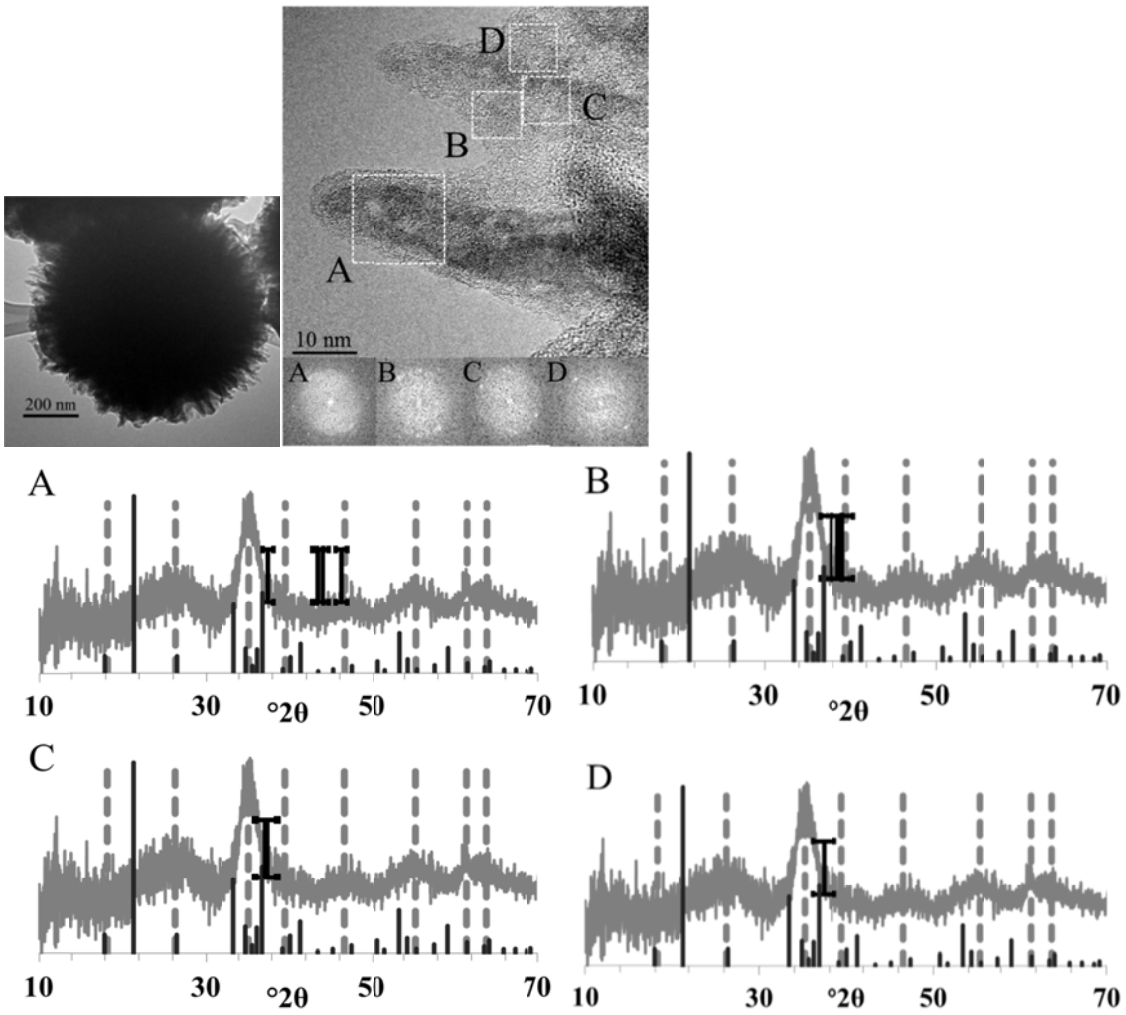

Figure B.S7. *Left TEM image is a schwertmannite particle from the Tinto Santa Rosa mine and the right TEM image shows needles from the surface of that particle. Insets in the right image show the FT of areas enclosed by white boxes. XRD patterns show the location of d-spacings measured from the FT analysis and the table gives the location of the planes. The FT d-spacings correspond to the solid black lines on the x-ray diffraction pattern with error bars. The error bars were calculated based on the method described in Figure B.S4. The black lines on the horizontal axis are the goethite standard d-spacings and the grey dotted lines are the schwertmannite literature values (Cornell and Schwertmann, 2003).*

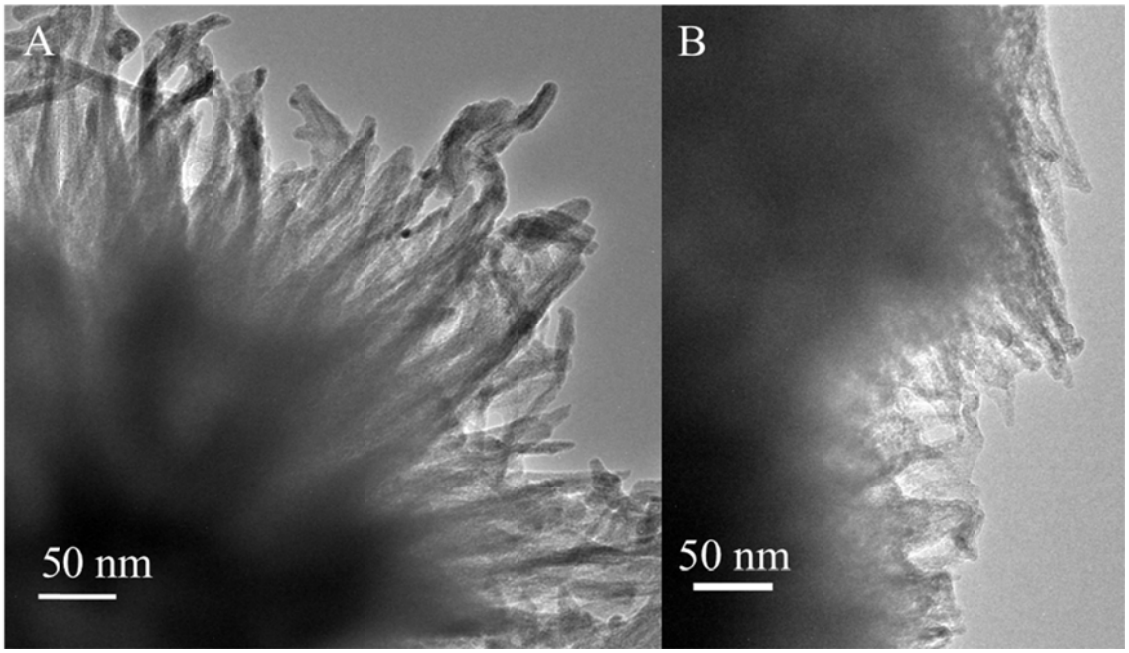

Figure B.S8. *(A) MR schwertmannite from which images for Figure 3.5 and 3.8 and supplemental Figure B.S9 were taken. (B) TSR schwertmannite from which images for Figure 3.9 and supplemental Figures B.S10 and B.S13 were taken.*

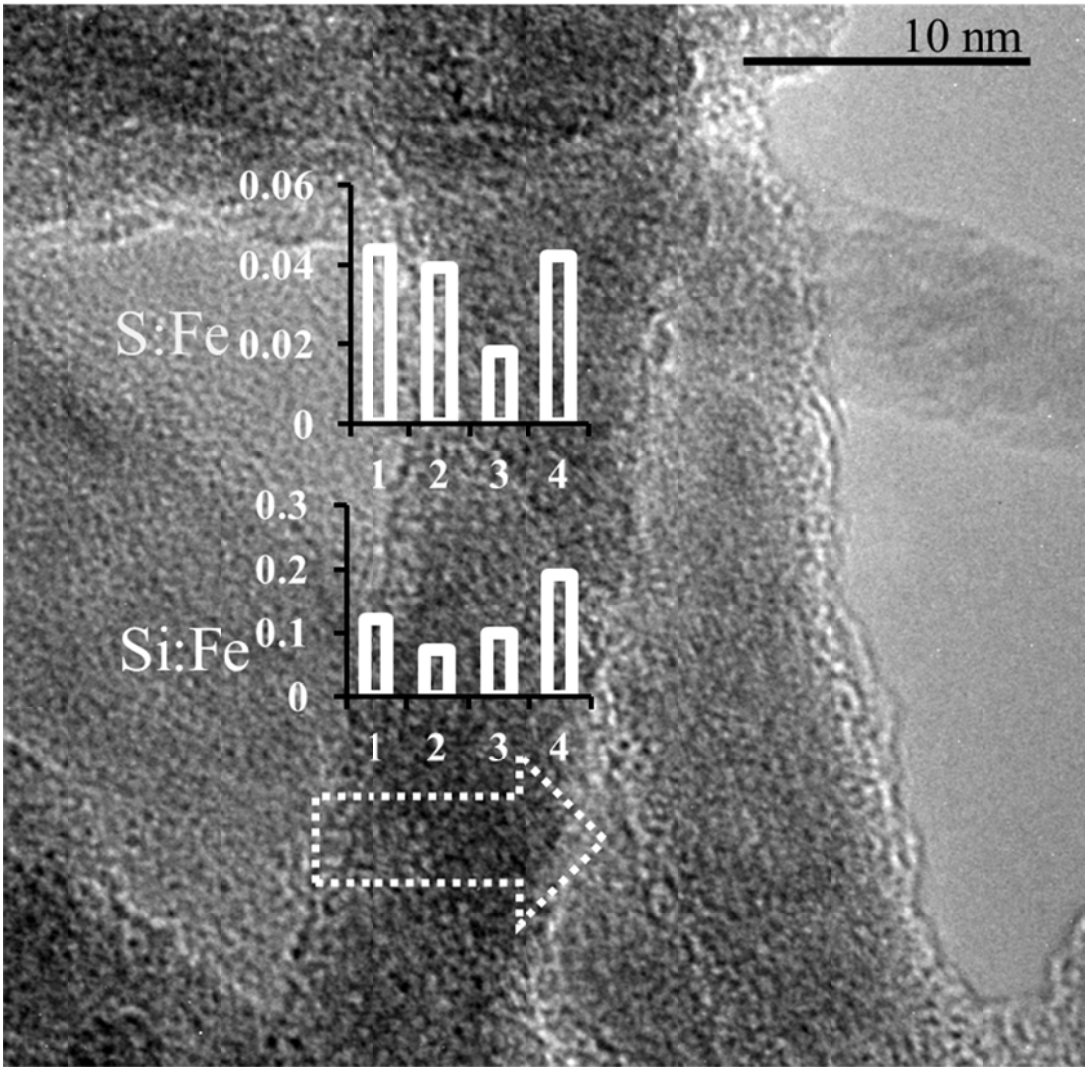

Figure B.S9. *S:Fe and Si:Fe ratios calculated from integrated peak intensity of EDX data collected at 4 points along the arrow from schwertmannite from the MR site.*

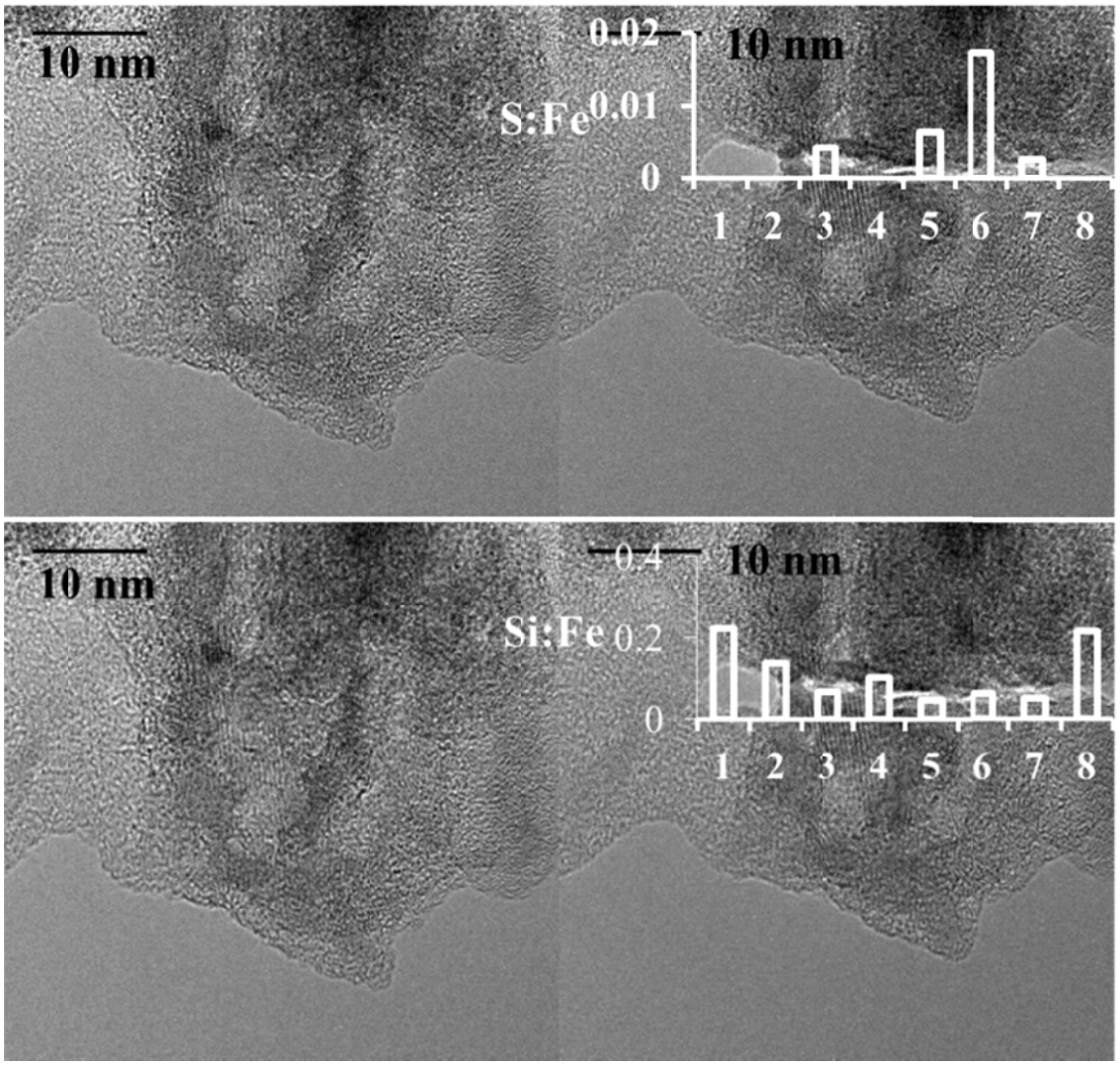

Figure B.S10. *S:Fe and Si:Fe ratios calculated from integrated peak intensity of EDX data collected at 8 points along the arrow across schwertmannite needles from the TSR site.*

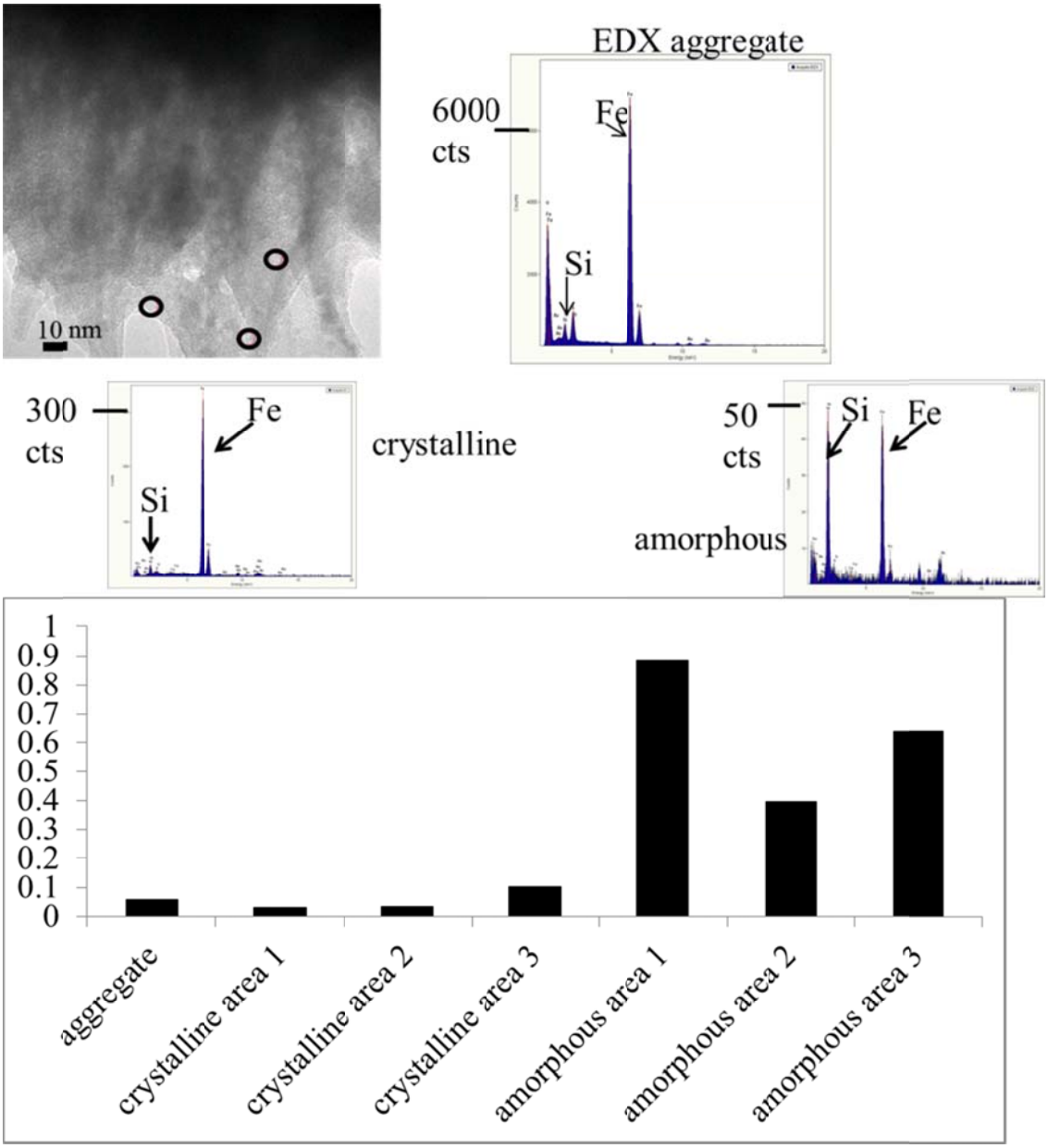

Figure B.S11. *Graph of semi-quantitative comparison of the silica to iron ratio in schwertmannite from the TSR site. 'Aggregate' refers to EDX data of the entire schwertmannite aggregate (inset Figure 3.3B) from which the TEM image shown above was taken. The black circles on the TEM image indicate the 'amorphous' areas where EDX data was collected. An example spectra is shown above and the Si:Fe ratios for the 3 'amorphous' areas are shown in the bar graph. EDX data on 3 'crystalline' areas was also collected and their Si:Fe ratios are shown in the bar graph with an example spectra above. Si:Fe ratios are calculated from the intensity ratio of the K peak for Si relative to the K peak for Fe. These ratios should not be taken as absolute concentrations and should only be compared relative to each other.*

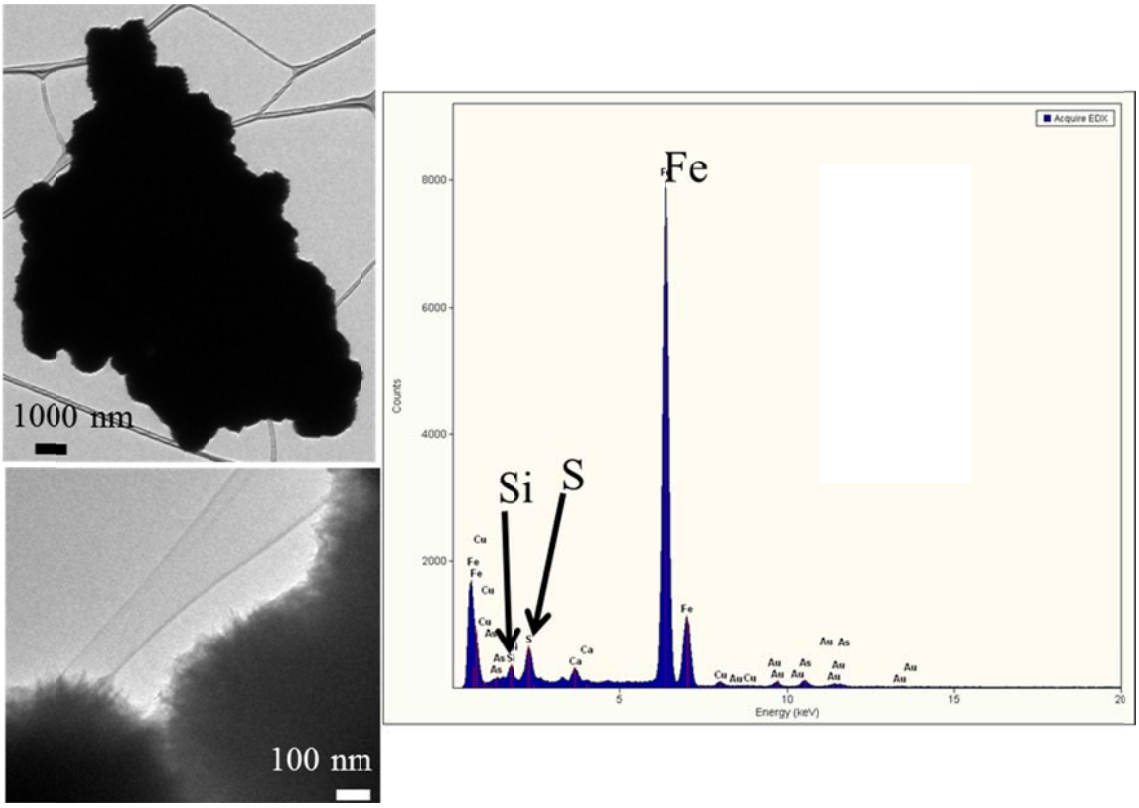

Figure B.S12. *Another schwertmannite aggregate on, which contained needles with the blotchy contrast seen in other schwertmannite aggregates observed. The EDX data of the entire aggregate showed that there was silica present on this aggregate with a similar ratio to that seen in Figure B.S11.*

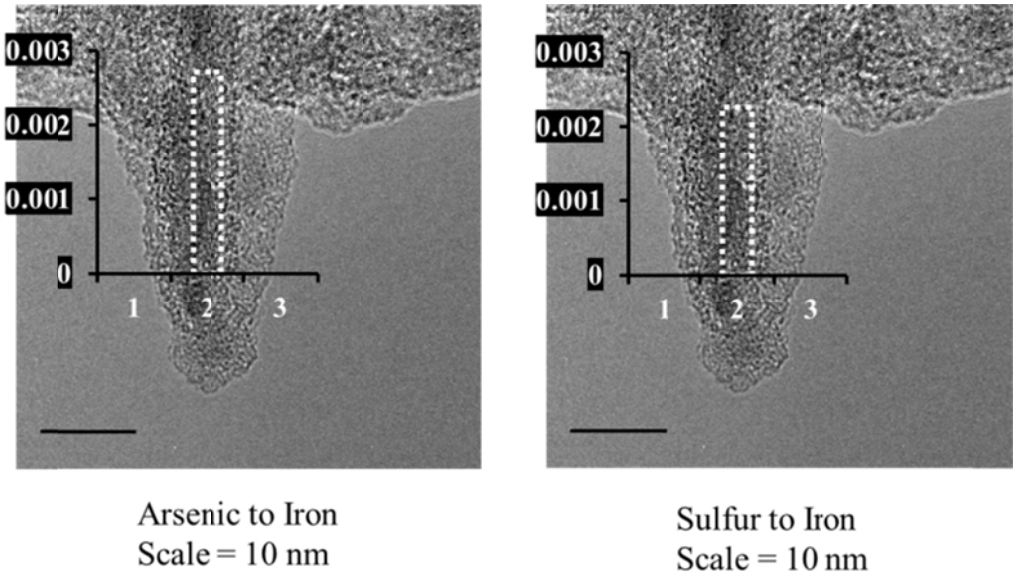

Figure B.S13. *The distribution of arsenic and sulfur across a needle of schwertmannite from the TSR site. Ratios of As:Fe and S:Fe should not be directly compared to each other. Ratios are calculated from the integrated intensity of EDX K peaks for these elements.*

References

Cornell, R.M., and Schwertmann, U. (2003) The Iron Oxides. 664 p. Wiley-VCH, Weinheim.